Electronic properties of organic-inorganic halide perovskites and their interfaces

Dissertation

zur Erlangung des akademischen Grades

d o c t o r r e r u m n a t u r a l i u m

(Dr. rer. nat.)

im Fach Physik

eingereicht an der

Mathematisch-Naturwissenschaftlichen Fakultät

der Humboldt-Universität zu Berlin

von

Herrn Fengshuo Zu, M.Sc.

Präsidentin der Humboldt-Universität zu Berlin

Prof. Dr.-Ing. Sabine Kunst

Dekan der Mathematisch-Naturwissenschaftlichen Fakultät

Prof. Dr. Elmar Kulke

Gutachter/in: 1. Prof. Dr. Norbert Koch

2. Prof. Dr. Christoph T. Koch

3. Prof. Dr. Derck Schlettwein

Datum der mündlichen Prüfung: 07.08.2019

Abstract

Optoelectronic devices based on halide perovskites (HaPs) and possessing remarkably high performance have been reported. To push the development of such devices even further, a comprehensive and reliable understanding of their electronic structure, including the energy level alignment (ELA) at HaPs interfaces, is essential but presently not available. In an attempt to get a deep insight into the electronic properties of HaPs and the related interfaces, the work presented in this thesis investigates i) the fundamental band structure of perovskite single crystals, in order to establish solid foundations for a better understanding the electronic properties of polycrystalline thin films and ii) the effects of surface states on the surface electronic structure and their role in controlling the ELA at HaPs interfaces. The characterization is mostly performed using photoelectron spectroscopy, together with complementary techniques including low-energy electron diffraction, UV-vis absorption spectroscopy, atomic force microscopy and Kelvin probe measurements.

Firstly, the band structure of two prototypical perovskite single crystals is unraveled, featuring widely dispersing top valence bands (VB) with the global valence band maximum at *R* point of the Brillouin zone. The hole effective masses there are determined to be ~0.25 m_0 for $CH_3NH_3PbBr_3$ and ~0.50 m_0 for $CH_3NH_3PbI_3$. Based on these results, the energy distribution curves of polycrystalline thin films are constructed, revealing the fact that using a logarithmic intensity scale to determine the VB onset is preferable due to the low density of states at the VB maximum. Secondly, investigations on the surface electronic structure of pristine perovskite surfaces conclude that the n-type behavior is a result of surface band bending due to the presence of donor-type surface states. Furthermore, due to surface photovoltage effect, photoemission measurements on different perovskite compositions exhibit excitation-intensity dependent energy levels with a shift of up to 0.7 eV. Eventually, control over the ELA

by manipulating the density of surface states is demonstrated, from which very different ELA situations (variation over 0.5 eV) at interfaces with organic electron acceptor molecules are rationalized. Our findings further help to explain the rather dissimilar reported energy levels at perovskite surfaces and interfaces, refining our understanding of the operational principles in perovskite related devices.

Keywords:

hybrid perovskites, energy level alignment, surfaces and interfaces, electronic band structure, density of surface states, surface photovoltage, photoelectron spectroscopy

Zusammenfassung

Über die besonders hohe Effizienz von Halid-Perowskit (HaP)-basierten optoelektronischen Bauteilen wurde bereits in der Literatur berichtet. Um die Entwicklung dieser Bauteile voranzutreiben, ist ein umfassendes und verlässliches Verständnis derer elektronischen Struktur, sowie der Energielevelanordnung (ELA) an HaP Grenzflächen von größter Bedeutung. Demzufolge beschäftigt sich die vorliegende Arbeit mit der Untersuchung i) der Bandstruktur von Perowskit-Einkristallen, um ein solides Fundament für die Darlegung der elektronischen Eigenschaften von polykristallinen Dünnschichten zu erarbeiten, und mit ii) den Einflüssen von Oberflächenzuständen auf die elektronische Struktur der Oberfläche, sowie deren Rolle bei der Kontrolle von ELA an HaP Grenzflächen. Die Charakterisierung erfolgt überwiegend mithilfe von Photoelektronenspektroskopie (PES) und ergänzenden Messmethoden wie Beugung niederenergetischer Elektronen an Oberflächen, UV-VIS-Spektroskopie, Rasterkraftmikroskopie und Kelvin-Sonde.

Erstens weist die Banddispersion von zwei prototypischen Perowskit-Einkristallen eine starke Dispersion des jeweiligen oberen Valenzbandes (VB) auf, dessen globales Maximum in beiden Fällen am R-Punkt in der Brillouin-Zone liegt. Dabei wird eine effektive Lochmasse von 0.25 m_0 für $CH_3NH_3PbBr_3$, bzw. von ~0.50 m_0 für $CH_3NH_3PbI_3$ bestimmt. Basierend auf diesen Ergebnissen werden die elektronischen Spektren von polykristallinen Dünnschichten konstruiert und es wird dadurch aufgezeigt, dass eine Bestimmung der Valenzbandkantenposition ausgehend von einer logarithmischen Intensitätsskala aufgrund von geringer Zustandsdichte am VB Maximum vorzuziehen ist.

Zweitens stellt sich bei der Untersuchung der elektronischen Struktur von frisch präparierten Perowskit-Oberflächen heraus, dass die n-Typ Eigenschaft eine Folge der Bandverbiegung ist, welche durch donatorartige Oberflächenzustände hervorgerufen

wird. Des Weiteren weisen die PES-Messungen an Perowskiten mit unterschiedlichen Zusammensetzungen aufgrund von Oberflächenphotospannung eine Anregungslichtintensitätsabhängigkeit der Energieniveaus von bis zu 0.7 eV auf. Darüber hinaus wird die Kontrolle von ELA durch gezielte Variation der Oberflächenzustandsdichte gezeigt, wodurch sich unterschiedliche ELA-Lagen (mit Abweichungen von über 0.5 eV) an den Grenzflächen mit organischen Akzeptormolekülen erklären lassen. Die vorliegenden Ergebnisse verhelfen dazu, die starke Abweichung der in der Literatur berichteten Energieniveaus zu erklären und somit ein verfeinertes Verständnis des Funktionsprinzips von perowskit-basierten Bauteilen zu erlangen.

Schlagwörter:

Energielevelanordnung, Oberfläche und Grenzfläche, elektronische Bandstruktur, Oberflächenzustandsdichte, Oberflächenphotospannung, Photoelektronen-spektroskopie

Abbreviations

AFM	Atomic force microscope
ARPES	Angle-resolved photoelectron spectroscopy
BE	Binding energy
CBM	Conduction band minimum
DFT	Density functional theory
DOS	Density of states
DoSS	Density of surface states
E_0	Electrostatic potential at 0, equivalent to E_{vac}
EA	Electron affinity
EDCs	Energy distribution curves
E_F	Fermi level
E_i	Intrinsic Fermi level
ELA	Energy level alignment
E_{vac}	Vacuum level
FWHM	Full-width at half maximum
HaPs	Hybrid perovskites or halide perovskites
HOMO	Highest occupied molecular orbitals
ID	Interface dipole
IE/IP	Ionization energy/potential
IMFP	Inelastic mean free path

KP	Kelvin probe
LEED	Low-energy electron diffraction
LUMO	Lowest unoccupied molecular orbitals
m^*	Effective mass
m_0	Free electron mass
PES	Photoemission/photoelectron spectroscopy
RT	Room temperature
SECO	Secondary electron cut-off
SPV	Surface photovoltage
UHV	Ultra-high vacuum
UPS/XPS	Ultraviolet/X-ray photoelectron spectroscopy
VBM	Valence band maximum
$\Delta\Phi_{BB}$	Change of Band bending
$\Delta\Phi_{ID}$	Change of interface dipole
Φ	Work function

Contents

Abstract ..... **i**

Zusammenfassung ..... **iii**

Abbreviations ..... **v**

Contents ..... **vii**

1 Introduction **1**

2 Fundamentals **5**

2.1 Theory of electronic structure of solids *5*

2.1.1 Free and nearly-free electron approximation 5

2.1.2 Tight-binding approximation 8

2.1.3 Density of states 10

2.1.4 Effective mass 11

2.1.5 Fermi level 12

2.2 Models and mechanisms of energy level alignment *14*

2.2.1 Surface states and surface band bending 14

2.2.2 Surface space-charge in thermal equilibrium 16

2.2.3 Surface photovoltage (SPV) 20

2.2.4 Vacuum level alignment 23

2.2.5 Fermi level pinning 24

3 Fundamentals of halide perovskites **26**

3.1 Crystal structure *26*

3.2 Electronic structure of halide perovskites *28*

3.3 Optoelectronic properties *30*

3.4 Film formation and engineering *32*

3.5 Applications in solar cells *33*

4 Fundamentals of experimental techniques **35**

4.1 Low-energy electron diffraction (LEED) *35*

4.2 Macroscopic Kelvin probe (KP) 37

4.3 Photoelectron spectroscopy (PES) 38

4.3.1 Three-step considerations 38

4.3.2 Valence-states and core-level photoemission 40

4.3.3 Angle-resolved photoelectron spectroscopy (ARPES) 44

5 Materials and experimental setups 46

5.1 Materials and sample preparation 46

5.2 Experimental setups 49

5.3 Data analysis 53

6 Results and discussion 56

6.1 Characterization of halide perovskites 56

6.2 Band structure of halide perovskite single crystals 58

6.2.1 LEED studies of halide perovskite single crystals 59

6.2.2 ARPES studies of halide perovskite single crystals 62

6.2.3 Summary 67

6.3 Determining the valence band onset of halide perovskites 68

6.3.1 Linear vs logarithmic plot for valence band onset 69

6.3.2 Valence band onset determination for halide perovskite systems 70

6.3.3 Summary 75

6.4 Surface electronic properties of halide perovskite thin films 75

6.4.1 Origin of surface n-type character 76

6.4.2 Impact of illumination on electronic and chemical structures 82

6.4.3 Effect of SPV in characterizing halide perovskites 89

6.4.4 Summary 92

6.5 Energy levels alignment at halide perovskite/electron acceptors interfaces 93

6.5.1 Low-DoSS perovskite/acceptor interfaces 94

6.5.2 High-DoSS perovskite/acceptor interfaces 98

6.5.3 Discussion and summary 102

7 Summary and outlook 107

8 Appendix 110

8.1 Excitation source parameters 110

8.2 Additional experimental data 110
8.2.1 Density functional theory 110
8.2.2 Determining the valence band onset of halide perovskites 111
8.2.3 Surface electronic properties of halide perovskite thin films 112
8.2.4 Energy levels alignment at halide perovskite/electron acceptors interfaces 115

Bibliography 119

Publications 129

Acknowledgements 131

Selbstständigkeitserklärung 132

1 Introduction

Hybrid organic-inorganic perovskites (HOIPs) or lately halide perovskites (HaPs) based optoelectronic devices have recently attracted tremendous attention and are being intensively investigated and explored in the fields of photovoltaics (PVs),[6, 78, 166] light-emitting diodes,[142, 168] photodetector[27] and laser devices.[180] In particular, HaPs-based PVs have made such a spectacular progress in power conversion efficiency (PCE) that the PV field has never witnessed before.[59] Perovskite materials exhibit excellent light absorption properties, similar to that of organic materials, with absorption coefficients exceeding 10^4 cm^{-1}.[22] Notably, the materials possess sharp absorption edges with low Urbach energy (as small as 15 meV),[22] high charge-carrier mobilities (typically more than 10 $cm^2 V^{-1} s^{-1}$)[13] and long diffusion lengths (up to 1 μm and even beyond).[138] All of these underlying optoelectronic properties of the perovskite materials have led to the outstanding performance of HaPs-based PVs.

These properties can be (partially) rationalized from perovskites electronic band structure. Therefore, assessing the electronic structure of HaPs materials, and with this the charge transport properties, is crucial for establishing a comprehensive understanding of HaPs-based optoelectronic devices. Tremendous investigations have been devoted to characterize the intrinsic electronic properties of the HaPs materials both theoretically and experimentally.[14, 34, 36, 79, 110, 127, 162, 184, 186] However, open questions regarding the electronic behavior still remain. In particular, the interfacial energy level alignments (ELAs) at HaPs interfaces, as the key to achieve high device performance, are subject to examination. A typical example for the electronic structure at interfaces in a *p-i-n*

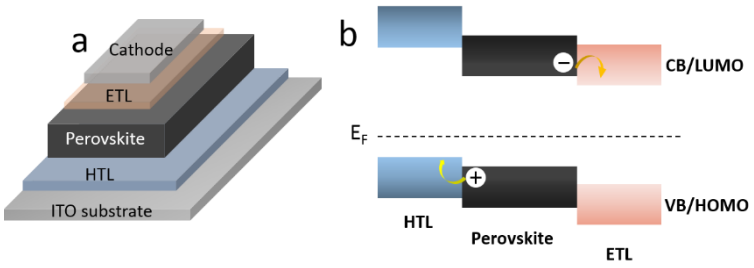

Figure 1.1 *(a) Schematics of a typical p-i-n architecture for perovskite solar cells. (b) Schematic electronic structure presenting p-i-n interfacial energetics. HTL and ETL stand for hole and electron transport layers, respectively.*

perovskite solar cell is schematically shown in **Figure 1.1**. As one can see, a perovskite solar cell typically comprises multiple functional interfaces, from hole (or electron) transport to hole (or electron) blocking layers which are inserted in order to enhance charge dissociation efficiency and reduce non-radiative recombination losses.[135-136, 159] With a favorable energy level alignment, the photo-generated electrons and holes can be efficiently transported, and eventually collected at the electrodes. For this purpose, it is necessary to gain a deep insight into the electronic processes occurring at perovskite-related interfaces in order to further optimize the energy level alignment.

In an attempt to contribute to a better understanding of the intrinsic band structure and the resulting ELA at perovskite-related interfaces, in this thesis, studies on the surface electronic structure of perovskite thin films and single crystals are carried out. In addition, the impact of the surface states on the ELA at perovskites/electron acceptor interfaces are investigated.

This thesis is structured in the following way: chapter 2 starts with an introduction on the basic elements of solid-state physics with a focus laid on electronic band structure. Specifically, this chapter contains, firstly, the theoretical models for approaching the electronic band structure of different solids, followed by some basic concepts in solid-state theory that are relevant to the investigations herein. Subsequently, section 2.2 is centered on the models and mechanisms of the energy level alignments at semiconductors' surface and interface. Detailed discussion on the effect of surface states on the energy level

alignments under thermal equilibrium and illumination is explicitly laid out. In chapter 3, the fundamental aspects of the HaPs materials are discussed. On one hand, the crystal structure, as the starting point to introduce the HaPs materials, is described. On the other hand, the application and development of HaPs in the PV field are briefly summarized. Additionally, focus is put on the electronic structure of HaPs material, which is one of the main keynotes in this thesis. Chapter 4 will introduce the experimental techniques that were employed, with a detailed guide on photoelectron spectroscopy. It is followed by chapter 5, which describes experimental details including sample preparation methods, experimental setups and the data processing.

After this, chapter 6 follows with the results and discussion. It starts with the characterization of some basic properties of prototype perovskite thin films and single crystals, in terms of morphological and structural properties. Then, the surface crystal structure as well as the band dispersion of cleaved $MAPbI_3$ and $MAPbBr_3$ single crystals are investigated by means of low-energy electron diffraction (LEED) and angle-resolved photoelectron spectroscopy (ARPES), as detailed in section 6.2. Supported by density-functional theory (DFT) calculations, the surface lattice structure and the band dispersion are elucidated, with the aim of gaining a better understanding of the intrinsic electronic properties. Based on these findings, we can resolve some of the challenges discussed in the community, such as how to determine the valence band onset with high reliability, which is the topic of section 6.3. Subsequently, in section 6.4.1, the surface electronic properties of $MAPbI_3$ thin films, as one of the prototypical HaPs, are examined by ultraviolet photoelectron spectroscopy (UPS). As a measure to elucidate the origin of the n-type behavior on perovskite surfaces, white light illumination is additionally applied during UPS measurements. Shifts in energy levels, as already induced by varying UV flux, by up to 0.7 eV under additional illumination, are observed, which can be interpreted as compensating the surface band bending at sufficient illumination-intensity. This phenomenon, known as surface photovoltage (SPV), is further investigated in section 6.4.2 by combining UPS and X-ray photoelectron spectroscopy (XPS). Based on these observations, the general

observation of SPV in perovskite materials from standard photoemission studies is further discussed and demonstrated in section 6.4.3. Results reveal that SPV, due to surface band bending likely induced by Pb^0-related surface states, can readily take place using different UV excitation flux during UPS measurements, highlighting the importance of lowering intensity of the optical excitation in order to obtain the energy levels at thermal equilibrium. Eventually, we will demonstrate in section 6.5 that due to the presence of donor-type surface states, the ELA at perovskite/electron accepter interfaces can be drastically modified. As a result, different ELA scenarios can be obtained even for the same material systems depending on the density of surface states. Finally, the work will end with a summary and outlook.

2 Fundamentals

2.1 Theory of electronic structure of solids

Understanding the movement of particles in a solid, to be specific, the motion of electrons or holes, is of fundamental importance for uncovering the electrical properties. This can be (partially) understood by the solid state electronic structure theories. Here some of the fundamental concepts and terms will be briefly introduced. In addition, two complementary methods for calculating the band structure, known as free electron and tight-binding approximations, will be shortly discussed.

2.1.1 Free and nearly-free electron approximation

It is instructive to start the discussion of the electronic structure with a simplified picture, in which the electrons in the solid are considered nearly free. Considering a solid being perfectly formed in periodicity, finding the quantum mechanical allowed eigenstates for the electrons can be approached by the (time-independent) Schrödinger equation for a single electron,[58]

$$\mathcal{H}\Psi = [-\frac{\hbar^2}{2m}\nabla^2 + U(\mathbf{r})]\Psi = E\Psi \qquad 2.1$$

in contrast to free-electrons, where the effective potential $U(\mathbf{r})$ is zero, the electron potential obeys

$$U(\mathbf{r}) = U(\mathbf{r} + \mathbf{R}) \qquad 2.2$$

following the same crystal periodicity. Now we can describe the motion of electrons in a non-vanishing periodic potential in order to solve the Schrödinger equation. The general form of electron wavefunction can be written as

$$\psi_{\mathbf{k}}(\mathbf{r}) = e^{i\mathbf{k}\cdot\mathbf{r}}\mu_{\mathbf{k}}(\mathbf{r}) \quad 2.3$$

where $\mu_{\mathbf{k}}(\mathbf{r})$ is a lattice periodic function, and it follows

$$\mu_{\mathbf{k}}(\mathbf{r}) = \mu_{\mathbf{k}}(\mathbf{r} + \mathbf{R}) \quad 2.4$$

One can write down the lattice potential as a Fourier series, using the reciprocal lattice vectors $\boldsymbol{G}$,

$$U(\boldsymbol{r}) = \sum_{\boldsymbol{G}} U_{\boldsymbol{G}} e^{i\boldsymbol{G}\cdot\boldsymbol{r}} \quad 2.5$$

where the vectors $\boldsymbol{G}$ are reciprocal lattice vectors

$$\boldsymbol{G} = h\mathbf{g}_1 + k\mathbf{g}_2 + l\mathbf{g}_3,\ h,\ k,\ l \text{ integers} \quad 2.6$$

Considering the solution of the Schrödinger equation to be a sum of plane waves,[74]

$$\psi_{\boldsymbol{k}}(\mathbf{r}) = \sum_{\boldsymbol{k}} c_{\boldsymbol{k}} e^{i\boldsymbol{k}\cdot\boldsymbol{r}} \quad 2.7$$

Inserting (2.5) and (2.7) into Schrödinger equation, one can eventually reduce the equation into the following form,

$$\left(\frac{\hbar^2 k^2}{2m} - E\right) c_{\boldsymbol{k}} + \sum_{\boldsymbol{G}} U_{\boldsymbol{G}} c_{\boldsymbol{k}-\boldsymbol{G}} = 0 \quad 2.8$$

Therefore, solving the Schrödinger equation is to solve the equation 2.8 for every $\boldsymbol{k}$ in the first Brillouin zone. Thus, the eigenvalues E of the Schrödinger equation (2.1) can be indexed as $E_{\boldsymbol{k}} = E(\boldsymbol{k})$, and the corresponding wavefunction is,

$$\psi_k(\mathbf{r}) = \sum_{\boldsymbol{G}} c_{\boldsymbol{k}-\boldsymbol{G}} e^{i(\boldsymbol{k}-\boldsymbol{G})\cdot\boldsymbol{r}} \quad 2.9$$

Eventually, the Schrödinger equation can be formalized as,

$$\mathcal{H}\Psi_{\boldsymbol{k}} = E(\boldsymbol{k})\Psi_k \quad 2.10$$

From above discussion, one can rationalize that the energy dispersion if neglecting the lattice potential ($U_{\boldsymbol{G}} = 0$) will be given by

$$E(\boldsymbol{k}) = E(\boldsymbol{k}-\boldsymbol{G}) = \frac{\hbar^2}{2m}(\boldsymbol{k}-\boldsymbol{G})^2 \quad 2.11$$

which is presenting a free electron situation, however, neglecting the lattice potential is often not the case for real solids.

Here, we would like to discuss an instructive case of a one-dimensional solid with a lattice constant of *a*. Thus the reciprocal lattice potential can be written in the following form,[58]

$$U(x) = U_0 + 2U_1\cos(gx) \qquad 2.12$$

where $g = 2\pi/a$, assuming that the potential U_1 is small compared to the kinetic energy of the electrons, the wavefunction can be expressed by a Fourier expansion,

$$\psi_k(x) = Aexp(ikx) + Bexp[i(k-g)x] \qquad 2.13$$

inserting (2.12) and (2.13) into Schrödinger equation, we will obtain a set of linear equations, which follow

$$\begin{bmatrix} (\hbar^2/2m)k^2 - U_0 - E & U_1 \\ U_1 & (\hbar^2/2m)(k-g)^2 - U_0 - E \end{bmatrix} \begin{bmatrix} A \\ B \end{bmatrix} = 0 \qquad 2.14$$

Solving matrix (2.14) results in the energy dispersion relation

$$E(k) = U_0 + E_1 + (\hbar^2/2m)k^2 \pm [{U_1}^2 + 4E_1(\hbar^2/2m)k^2]^{1/2} \qquad 2.15$$

where $E_1 = (\hbar^2/2m)(g/2)^2$,

The results are schematically presented in Figure 2.1 known as the band structure. As we can see the band structure is still very much like the one of free electrons (parabolic dispersion), however, the bands are not continuous at the Brillouin zones boundary. The

opening of the bands is referred to as the band gap with the width of $2U_1$.

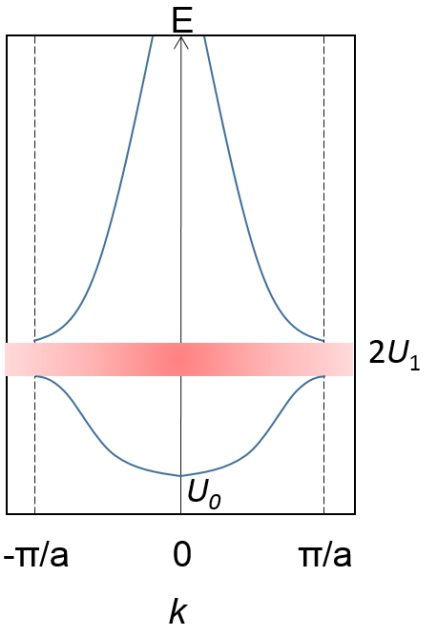

Figure 2.1 *Schematic of the energy dispersion curves E(k) (in parabola) for a one-dimensional lattice in the reduced first Brillouin zone. The opening gaps marked in red shadow are referred as band gaps, where no states are available.*

2.1.2 **Tight-binding approximation**

A complementary method, known as the tight-binding model or linear combination of atomic orbitals (LCAO), can be used to deal with electrons where there is strong overlap of interactions. In practice, it gives reasonable approximations to the band structure of covalently bonded crystals and localized electrons in transition metals. The basic procedure that is employed in this method will be shortly described. The details are referred to the textbook from Hofmann,[58] Ibach and Lüth.[62]

In contrast to the situation for a free electron, the Hamiltonian for an electron can be written as

$$\mathcal{H} = \mathcal{H}_0 + \mathrm{v} = -\frac{\hbar^2}{2m}\nabla^2 + U_A(\boldsymbol{r} - \boldsymbol{r_n}) + \mathrm{v}(\boldsymbol{r} - \boldsymbol{r_n}) \qquad 2.16$$

where $\mathcal{H}_0$ is the Hamiltonian for a single atom and v is a perturbation to the potential U_A of the free atom. Thus the perturbation can be given as

$$\mathrm{v}(\boldsymbol{r} - \boldsymbol{r_n}) = \sum_{m \neq n} U_A(\boldsymbol{r} - \boldsymbol{r_m}) \qquad 2.17$$

i.e. taking the sum over the potentials of other atoms. Within the tight-binding model, the

wavefunction $\psi_{\mathrm{k}}(\boldsymbol{r})$ can be approximated by a linear combination of atomic orbitals $\phi_i(\boldsymbol{r}-\boldsymbol{r_n})$ that satisfies the Bloch's theorem, which is formed as

$$\psi_{\mathrm{k}}(\boldsymbol{r}) \approx \frac{1}{\sqrt{N}}\sum_{\boldsymbol{n}} e^{i\boldsymbol{k}\cdot\boldsymbol{r_n}}\phi_i(\boldsymbol{r}-\boldsymbol{r_n}) \tag{2.18}$$

where N is the number of atoms in the crystal and the factor of $\frac{1}{\sqrt{N}}$ ensures a normalized Bloch wave. Considering the single particle states as described by equation 2.10, the solution to the Schrödinger equation, i.e. the band dispersion relations, can be calculated as

$$\mathrm{E}(k) = \frac{<\psi_{\mathbf{k}}|\boldsymbol{\mathcal{H}}|\psi_{\mathbf{k}}>}{<\psi_{\mathbf{k}}|\psi_{\mathbf{k}}>} \tag{2.19}$$

where $<\psi_{\mathbf{k}}|\boldsymbol{\mathcal{H}}|\psi_{\mathbf{k}}> = \int d\boldsymbol{r}\psi^*{}_{\mathbf{k}}\boldsymbol{\mathcal{H}}\psi_{\mathbf{k}}$ and $<\psi_{\mathbf{k}}|\psi_{\mathbf{k}}> = \int d\boldsymbol{r}\psi^*{}_{\mathbf{k}}\,\psi_{\mathbf{k}}$.

Knowing the solution to the free atom as discussed above, one obtains

$$\mathrm{E}(k) \approx \frac{1}{N}\sum_{n,m} e^{i\boldsymbol{k}\cdot(\boldsymbol{r_n}-\boldsymbol{r_m})}\int \phi_i{}^*(\boldsymbol{r}-\boldsymbol{r_n})\,[E_i + \mathrm{v}(\boldsymbol{r}-\boldsymbol{r_n})]\phi_i(\boldsymbol{r}-\boldsymbol{r_n})d\boldsymbol{r} \tag{2.20}$$

where E_i is the energy eigenvalue of the isolated atoms. One can already anticipate that the solution to E_i neglects the interaction between nearest neighbor atoms. On the other hand, the perturbation $\mathrm{v}(\boldsymbol{r}-\boldsymbol{r_n})$ only includes the overlap between the nearest neighbors. In order to come closer to the solution, we now consider a simple case where the atomic states ϕ_i possess spherical symmetry, the band dispersion can be readily reduced to

$$\mathrm{E}(k) \approx E_i - \alpha - \beta\sum_{m} e^{i\boldsymbol{k}\cdot(\boldsymbol{r_n}-\boldsymbol{r_m})} \tag{2.21}$$

where the two quantities are

$$\begin{aligned}\alpha &= -\int \phi_i{}^*(\boldsymbol{r}-\boldsymbol{r_n})\mathrm{v}(\boldsymbol{r}-\boldsymbol{r_n})\phi_i(\boldsymbol{r}-\boldsymbol{r_n})d\boldsymbol{r}\\ \beta &= -\int \phi_i{}^*(\boldsymbol{r}-\boldsymbol{r_m})\mathrm{v}(\boldsymbol{r}-\boldsymbol{r_n})\phi_i(\boldsymbol{r}-\boldsymbol{r_n})d\boldsymbol{r}\end{aligned} \tag{2.22}$$

Generally, the electronic structure in real solid is much more complex that the simple free electron or tight-binding models become invalid. Therefore, much more advanced methods have to be implemented.

2.1.3 **Density of states**

The density of states (DOS) function describes the number of states per energy interval that are available in a system. For a material system, it is essential for determining the number of electrons or holes at each energy which can be obtained by multiplying the number of states with probability that a state is occupied by an electron or a hole. If knowing the band dispersions E($\boldsymbol{k}$), one can simply integrate the states over the area *S* with the same energy, considering the spin of the electrons, the DOS can be written as[134] ,

$$D(E) = \ 2\frac{V}{(2\pi)^3}\int \frac{dS}{|\nabla_{\boldsymbol{k}} E|} \qquad 2.23$$

Note that at some points, where $|\nabla_{\boldsymbol{k}} E| = 0$, the DOS will exhibit singularities, known as Van Hove singularity.[148] Since E($\boldsymbol{k}$) is a periodic function in $\boldsymbol{k}$ space, there will be periodic points where $|\nabla_{\boldsymbol{k}} E| = 0$, such as band maximum and minimum $\boldsymbol{k}$ points.

As an example in a 3 dimensional system, where it can be treated as a free electron model, e.g. for the case of an infinite quantum well. Note that such model can also be generally applied to the band edges even in a tight-binding system, where the electron near these regions can be treated as free electrons. The semiconductor is then assumed as a cube with side of *L*. The solutions to the Schrödinger equation ($[-\frac{\hbar^2}{2m}\nabla^2 + \mathrm{U(x)}]\Psi = \frac{\hbar^2 k^2}{2m}\Psi$), where U(x) = 0 can be given as

$$\Psi = \mathrm{A}\sin(k_x \mathrm{x}) + \mathrm{B}\cos(k_x \mathrm{x}) \qquad 2.24$$

where A and B are constant. Given the boundary conditions, the wavenumber must be

$$k_x = \frac{n\pi}{L}, n = 1,2,3 \ldots \qquad 2.25$$

The analysis holds for y and z directions as well. The total number of solutions is obtained as

$$N_{3D} = \frac{2\frac{4\pi k^3}{3}}{(\frac{2\pi}{L})^3} = \frac{L^3}{3\pi^2}k^3 = \frac{L^3}{3\pi^2}(\frac{2m_0E}{\hbar^2})^{3/2} \quad 2.26$$

therefore, the DOS per unit energy and per unit volume in 3 dimension systems is,

$$D(E)_{3D} = \frac{dN}{L^3 dE} = \frac{8\pi\sqrt{2}}{h^3}m_0^{3/2}\sqrt{E}, for\ \ E \geq 0 \quad 2.27$$

Similarly, the number of states per unit energy and unit volume in 2 and 1 dimensional systems are[134]

$$D(E)_{2D} = \frac{4\pi m_0}{h^2} \quad 2.28$$

$$D(E)_{1D} = \sqrt{\frac{2\pi m_0}{h^2}}\frac{1}{\sqrt{E}}, for\ \ E \geq 0$$

respectively. The sketch below is an idealized depiction of the density of states in 3, 2 and 1 dimensional systems.

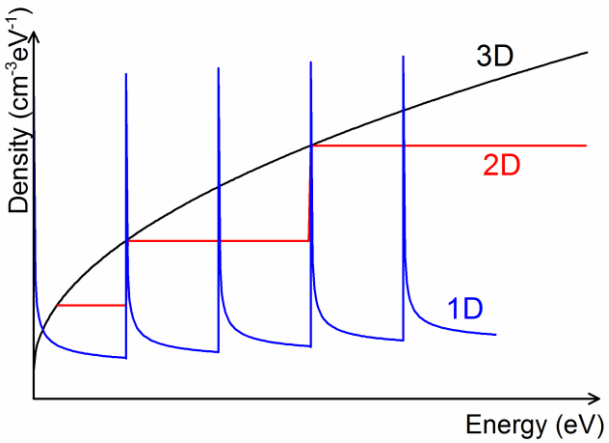

Figure 2.2 *Sketch of the density of states per unit volume and energy for a 3D (black), 2D (red) and 1 D (blue) systems.*

2.1.4 **Effective mass**

It is apparent that the electrons in a semiconductor crystal behave differently from the free electrons, as the electrons in a solid experience forces from other electrons and ions/atoms. The effective mass is thus introduced in order to describe the movement of

electrons in a solid with all of the forces imposed on them (within single-particle approximation). As we just discussed the free electron movement in a solid, the energy of the electrons at the maximum or minimum of the energy bands is given as

$$E = \frac{\hbar^2 \boldsymbol{k}^2}{2m_0} \qquad 2.29$$

where m_0 is the mass of electrons in vacuum. The effect in a solid is that it can change the effective mass of the electrons, thus, the effective mass can be much smaller or bigger than the free electron mass. From the band theory, we know that the interactions imposed on the electrons are taken into account in the band structure, the curvature of the bands in a solid thus takes the form as

$$E = E_0 + \frac{\hbar^2 \boldsymbol{k}^2}{2m^*} \qquad 2.30$$

where m* is the effective mass, which can be quite different form the free electron mass.

The concept of the effective mass can be intuitively understood when considering the classical equation of motion as described in the Drude model. Now consider the acceleration of an electron traveling with group velocity v_g, $a = \frac{dv_g}{dt}$. Given $v = \frac{d\omega}{dk}$ and the de Broglie equations ($E = \hbar\omega \ \ and \ \ p = \hbar k$), it can be further formulated as

$$a = \frac{dv_g}{dt} = \frac{1}{\hbar}\frac{d}{dt}\frac{dE(k)}{dk} = \frac{1}{\hbar}\frac{d^2E(k)}{dk^2}\frac{dk}{dt} = -\frac{1}{\hbar^2}\frac{d^2E(k)}{dk^2}F \qquad 2.31$$

where F is the applied force. Comparing with the classical mechanics ($F = ma$), the effective mass takes the form as

$$m^* = \hbar^2\{\frac{d^2[E(k)]}{dk^2}\}^{-1} \qquad 2.32$$

Thus, the effective mass sets the high limit for the carrier mobility in a solid.

2.1.5 **Fermi level**

One of the fundamental concepts to understand the energy level alignment of solids is the Fermi level (E_F). The Fermi level comes from Fermi-Dirac statistics in statistical

physics,

$$f(E) = \frac{1}{\exp(\frac{E - E_F}{k_B T}) + 1} \qquad 2.33$$

It is the surface of the 'electron sea' where the occupation probability of electrons equals 0.5 independent of the given materials, either for metals, semiconductors or insulators. It is worth to mention that, from definition, the term Fermi energy refers to the energy of the highest occupied energy level of electrons at absolute zero temperature in a metal, thus it is differently defined than the Fermi level.[62]

The Fermi level plays an important role in semiconductor physics, as the electron population depends upon the product of Fermi-Dirac function and the electron density of states. In addition, the doping concentration of a semiconductor can be approximated by their relative positions with respect the conduction or valence band edges.

As an example, one can calculate the number of electrons in the conduction band and holes in the valence band of a semiconductor,[105] which can be given as

$$n = \int_{E_C}^{E_{top}} D_C(E) f(E) dE\,, \qquad p = \int_{E_{bottom}}^{E_V} D_V[1 - f(E)] dE \qquad 2.34$$

where D_C and D_V are density of states in the conduction and valence bands, respectively. The actual location of the top conduction band or bottom valence band is not required to be known as the Fermi function goes to zero at high energies. Such integral can only be analytically solved at $T = 0$, however, for non-degenerate semiconductors for which the Fermi level is at least $3kT$ away from either of the band edges, the Fermi function can be replaced as a simple exponential function. Therefore, for a 3 dimensional system, combining with 2.27 the integral can then be solved analytically,

$$n \cong \int_{E_C}^{E_{top}} \frac{8\pi\sqrt{2}}{h^3} m_e^{*\frac{3}{2}} \sqrt{E - E_C}\, e^{\frac{E_F - E}{kT}} dE = N_C \exp\left(\frac{E_F - E_C}{k_B T}\right), and \qquad 2.35$$

$$p \cong \int_{E_{bottom}}^{E_V} \frac{8\pi\sqrt{2}}{h^3} m_h^{*\frac{3}{2}} \sqrt{E_V - E} e^{\frac{E-E_F}{kT}} dE = N_V \exp(\frac{E_V - E_F}{k_B T})$$

where the effective density of states in the conduction and valence band are defined as

$$N_C = 2(\frac{2\pi m_n^* kT}{h^2})^{3/2}, and \;\; N_V = 2(\frac{2\pi m_p^* kT}{h^2})^{3/2} \qquad 2.36$$

respectively.

2.2 Models and mechanisms of energy level alignment

Understanding of the electronic structure, in particular, the subject of energy level alignment either on the surface and/or interface, is of fundamental importance in order to optimize the energy offsets and further improve the performance of any functional devices.[11, 64, 75] In this subchapter, we will briefly review and discuss some basic models, terms and processes relevant in ELA. Starting with a short description of surface states and their impact on surface band bending, a qualitative analysis of the electrical properties of a semiconductor having a space-charge region is laid out under the condition of thermal equilibrium. Furthermore, detailed accounts of the charge-carrier distribution in space-charge regions upon illumination are given, providing a physical insight into the surface photovoltage phenomenon. The mathematical approach applied in this chapter is mainly based on the textbook from Mönch[105] and the review article from Kronik and Shapira.[82] Finally, two fundamental models to understand the ELAs, i.e. vacuum level alignment and Fermi level pinning, are introduced.

2.2.1 Surface states and surface band bending

Semiconductor surfaces and interfaces often exhibit modified electronic and structural properties in comparison with the bulk of the material. This often originates from surface and interface states, respectively. Surface states on semiconductor surfaces exhibit either

donor or acceptor character, depending on their position with respect to the Fermi level. The surface regime remains overall electrically neutral, therefore, the charged surface states would induce a space-charge layer beneath the surface. As a result, the condition of charge neutrality still satisfies,[82]

$$Q_{SC} + Q_{SS} = 0 \qquad 2.37$$

where Q_{SC} and Q_{SS} are the charges in space-charge layer and surface states, respectively.

The origins of surface states can range from dangling bonds on abrupt terminated semiconductor surfaces to adsorbate covered surfaces. The presence of surface states has

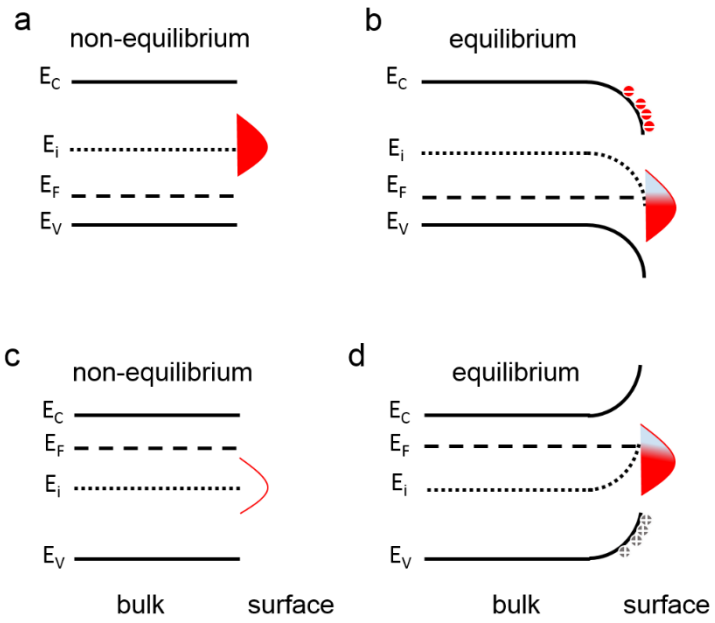

Figure 2.3 *Schematic energy level diagram of the donor-type surface states on a p-type semiconductor (a) before thermal equilibrium and (b) after equilibrium condition where surface states being partially ionized. A reversal process is also illustrated in (c) and (d), where acceptor-type surface states induced upward surface band bending on a n-type semiconductor surfaces.*

been demonstrated to have large impacts on the energy levels on semiconductor surfaces, such as in GaN and ZnO systems.[52, 126, 147]

In the case of a donor type surface states on a p-type semiconductor surface, as shown schematically in **Figure 2.3** (a) and (b), the difference in Fermi levels in the bulk and the

surface states will lead to the redistribution of electrons, so that the electrons from the surface states will fill up the energy levels below it in the semiconductor surface region following Fermi-Dirac statics in order to reach thermodynamic equilibrium. Accumulation of electrons in the semiconductor surface region will occur concomitant with a downward band bending (from bulk to surface). Such band bending will bring down the level of donor surface states, and eventually result in the common alignment of Fermi level between the bulk and surface states, reaching Fermi level alignment.

An opposite process occurs, as shown in **Figure 2.3** (c) and (d), in which the acceptor-type surface states on a n-type semiconductor surfaces will result in an upward surface band bending, so that the electronic equilibrium state can be reached.

2.2.2 **Surface space-charge in thermal equilibrium**

The aim of this section is to derive the space-charge Q_{SC} in dark condition so that the change in Q_{SC} upon illumination can be understood analytically. We start by considering carrier densities in space-charge layers for non-degenerately doped semiconductors* in thermal equilibrium, i.e. in dark condition. Considering a one dimensional situation, the spatial variation of band bending in the space-charge region as shown in **Figure 2.4** (b), can be described as,

$$\mathrm{V(z)} = \frac{1}{e}[E_{Vb} - E_V(z)] = \frac{1}{e}[E_{Cb} - E_C(z)] \qquad 2.38$$

where the subscript *b* denotes for the bulk properties, and $E_{V,C}$ stand for valence/conduction bands. The potential V(z) can be approached from Poisson's equation,

$$\Delta \mathrm{V(z)} = -\rho(\mathrm{z})/\varepsilon_0\varepsilon_\mathrm{r} \qquad 2.39$$

Here, ε_0 and ε_r are dielectric constant in vacuum and of the semiconductor, respectively. Assuming a constant doping concentrations, the space-charge consists of positive and

*Non-degenerate semiconductors refer to a certain level of dopant concentration under which the energy levels of the dopants can still be treated like in atoms.

negative charges and can be given as

$$\rho(z) = e[N_d^+ - N_a^- - n(z) + p(z)] \quad 2.40$$

From the classical Maxwell-Boltzmann statistics, the bulk carrier densities for the non-degenerated semiconductor can be given by

$$n_b = N_C \exp\left(-\frac{E_{Cb} - E_F}{k_B T}\right) = n_i \exp\left(-\frac{E_{ib} - E_F}{k_B T}\right) \quad 2.41$$

and

$$p_b = N_V \exp\left(\frac{E_{Vb} - E_F}{k_B T}\right) = n_i \exp\left(\frac{E_{ib} - E_F}{k_B T}\right), \quad 2.42$$

where the effective density of states for electrons and holes are defined as $N_C = 2(2\pi m_e^* k_B T/h^2)^{3/2}$ and $N_V = 2(2\pi m_h^* k_B T/h^2)^{3/2}$, respectively. Subscript i refers to the intrinsic quantities. Moreover, the electron and hole densities in the space-charge region can be related to the quasi-neutral bulk quantities from the Boltzmann relations, which can be given as

$$n(x) = n_b \exp[\frac{eV(x)}{k_B T}], \text{ and } p(x) = p_b \exp[-\frac{eV(x)}{k_B T}] \quad 2.43$$

Beside, in the quasi-neutral region the net charge density is zero so that

$$N_d^+ - N_a^- = n_b - p_b \quad 2.44$$

As a result, given 2.43 and 2.44 the space-charge density of 2.40 can be written as

$$\rho(z) = e\{n_b - p_b - n_b \exp[\frac{eV(z)}{k_B T}] + p_b \exp[-\frac{eV(z)}{k_B T}]\} \quad 2.45$$

assuming that the donors and/or acceptors are completely ionized in the bulk. Here, for simplicity, the reduced quantities are introduced, where v and u denote for the magnitude of band bending and the degree of doping in unit of $k_B T$, respectively, which are

$$v \equiv \frac{eV}{k_B T} = \frac{E_{ib} - E_i}{k_B T}, \text{ and } u \equiv \frac{E_F - E_i}{k_B T} \quad 2.46$$

This is illustrated in **Figure 2.4** (b) for the energy level diagram in the case of a p-type semiconductor. Now, the Poisson's equation can be re-written as

$$\Delta v(\mathrm{z}) = -\left(\frac{e^2}{\varepsilon_r \varepsilon_0 k_B \mathrm{T}}\right)(n_b - p_b - n_b e^{v} + p_b e^{-v}) = L_D^{-2}[\frac{\sinh(u_b+v)}{coshu_b} - tanhu_b], \quad 2.47$$

where the extrinsic Debye length is

$$L_D^2 = \frac{\varepsilon_r \varepsilon_0 k_B \mathrm{T}}{e^2(n_b + p_b)} \quad 2.48$$

Since now the Poisson's equation is independent of position *z*, one can integrated 2.47 once to obtain

$$\frac{dv}{dz} = \pm\frac{F}{L_D} \quad 2.49$$

where *F* is defined as space-charge function

$$F(u_b, v) = \sqrt{2}[\frac{\cosh(u_b + v)}{coshu_b} - v \cdot tanhu_b - 1]^{1/2} \quad 2.50$$

Finally, the space-charge density Q_{SC} can be quantified. Gauss's law gives the Q_{sc} as

$$Q_{SC} = \varepsilon_r \varepsilon_0 \frac{dV}{dz}|_{z=0}, \quad 2.51$$

Using relation of 2.49, Q_{SC} can be calculated as

$$Q_{SC} = \pm e(n_b + p_b) L_D F_S \quad 2.52$$

where the subscript "*S*" denotes for surface quantity.

To better illustrate the equation 2.50, the space-charge function F_S as a function of the surface band bending v_S for a p-doped semiconductor with different doping concentrations (u_b) is shown in Figure 2.4 (a). Three different regimes, which are related to depletion, inversion and accumulation of the mobile carriers at the surface, can be seen in Figure 2.4 (b). In this case, the bands are bent downwards, giving rise to positive values of v_S. Enhancing of surface band bending, i.e. conduction band at the surface becomes become closer to the Fermi level, leads to a depletion of majority carriers (holes in this case). When $|v_S|$ becomes larger than $|u_b|$, the very surface region turns into intrinsic condition and the inversion regions appear, i.e. the electron density, which is the minority carriers of the semiconductor will become more than the intrinsic carrier density. Further increasing v_S more than $2|u_b|$, the minority carriers then behave like majority carriers in the accumulation region.

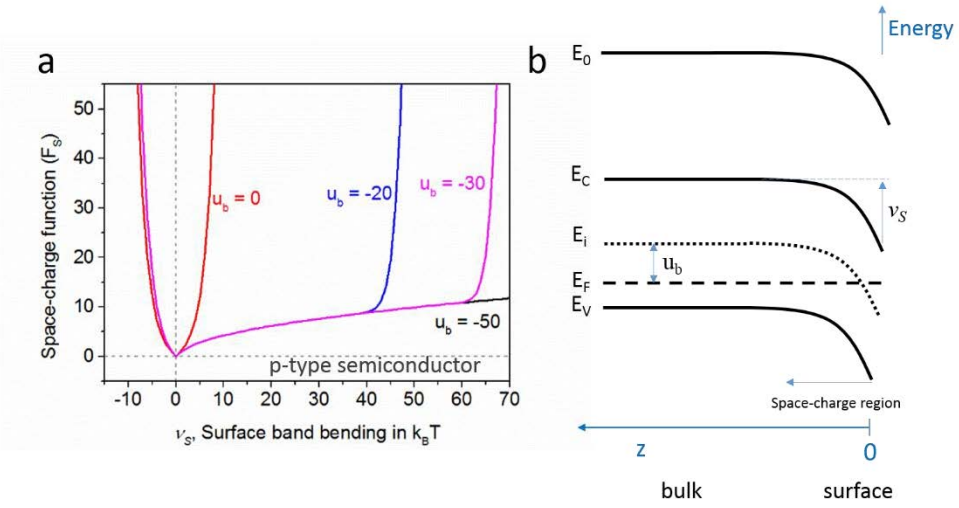

Figure 2.4 *(a) Space-charge function F_S as a function of surface band bending v_S for a p-doped semiconductor with different doping concentrations (u_b). u_b = 0 denotes for intrinsic situation. Data extracted from [105] (b) Sketch of the energy level diagram for a p-type semiconductor in the case of downward surface band bending.* v_S *and* u_b *are in the unit of* k_BT. *E_0 refers to electrostatic potential at 0, which is equivalent to vacuum level.*

2.2.3 **Surface photovoltage (SPV)**

In general, the surface photovoltage effect involves illumination-induced changes in surface potential and surface Fermi level position. A simplified picture of the influence of SPV on the energy levels of a p-type semiconductor is shown in **Figure 2.5**. The surface band bending, as depicted in the p-type semiconductor surface, can be attributed to the presence of donor-type surface states discussed in section 2.2.1. In this thesis, we only focus on super-band gap excitation, which concerns band-to-band absorption. Upon illumination, electron-hole pairs will be created and being pushed away in opposite direction by the electric field in the depletion layer. Therefore, a field is created that will compensate the

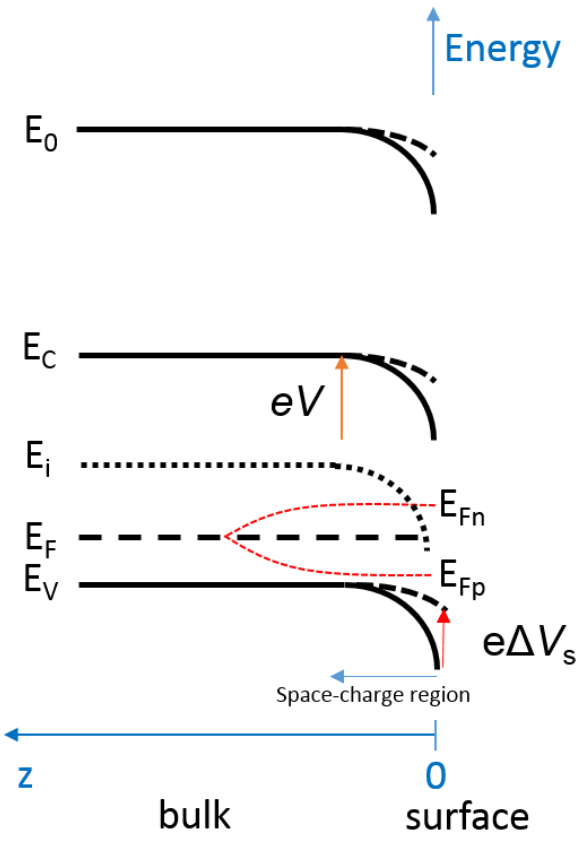

Figure 2.5 *Schematic drawing of a surface space-charge region band alignment. Solid lines represent equilibrium condition while dashes lines indicate the SPV effect in reducing surface band bending. eV and $e\Delta V_S$ denote the magnitude of initial band bending and change in surface band bending, respectively. E_{Fn} and E_{Fp} stand for quasi-Fermi level for electrons and holes upon illumination, respectively. E_0 refers to electrostatic potential at 0, which is equivalent to vacuum level.*

surface band bending. Assuming the photo-generated carriers are mostly located at the surface region, if recombination is low or can be sufficiently suppressed, the SPV would result in a flat band condition and the difference between the states of maximum and no SPV represents the magnitude of surface band bending.[3, 50]

In steady state illumination, the quasi-equilibrium distribution of electrons and holes can be expressed by quasi-Fermi levels given as E_{Fn} and E_{Fp}, respectively. This is depicted schematically in **Figure 2.5** for a p-type semiconductor. The spatial carrier density of electrons and holes in the space-charge region are given as

$$n(z) = n_i \exp\left[\frac{E_{Fn} - E_i(z)}{k_B T}\right] = n_b \gamma_n \exp[v(z)] \qquad 2.53$$

and

$$p(z) = n_i \exp\left[-\frac{E_{Fp} - E_i(z)}{k_B T}\right] = p_b \gamma_p \exp[-v(z)] \qquad 2.54$$

Where γ_n and γ_p are normalized carrier excesses for electrons and holes, respectively, which are given as

$$\gamma_n = \frac{n_0(z)+\Delta n(z)}{n_0(z)} = \exp(\frac{E_{Fn}-E_F}{k_B T}),\ \gamma_p = \frac{p_0(z)+\Delta p(z)}{p_0(z)} = \exp(-\frac{E_{Fp}-E_F}{k_B T}) \qquad 2.55$$

The subscript 0 refers to thermal equilibrium condition, i.e. in dark. Note that the charge neutrality requires $\Delta n = \Delta p$, one would get

$$(\gamma_p - 1)(\gamma_n - 1) = \exp(2u_b) \qquad 2.56$$

Therefore, under non-equilibrium condition, i.e. under illumination, the space-charge density can be re-written as

$$\rho(z) = e\{n_b - p_b - n_b\,\gamma_n exp[v(z)] + p_b \gamma_b \exp[-v(z)]\} \qquad 2.57$$

Considering 2.56, the resulting Poisson's equation is

$$\Delta v(z) = L_D^{-2}[\frac{\sinh(u_b + v)}{cosh u_b} - tanh u_b + (\boldsymbol{\gamma_p} - \mathbf{1})\exp(-\boldsymbol{u_b})\boldsymbol{sinh v / cosh u_b}] \qquad 2.58$$

Comparing with the Poisson's equation of 2.47 in thermal equilibrium, it reveals the fact that the third term (in bold) in the bracket on the right side accounts for non-equilibrium condition. Applying Gauss's law on the once integrated Poisson's equation lead to the solution of the space-charge, which is

$$Q_{SC} = \pm e(n_b + p_b)L_D[F^2(v_s, u_b) + 4(\gamma_p - 1)\exp(-u_b)sinh^2(v_s/2)/coshu_b]^{1/2} \quad 2.59$$

It is noted that the total charges $Q_{tot} = Q_{SS} + Q_{SC}$ in the space-charge region and surface states always remain constant even under illumination. In order to picture the influence of illumination on surface band bending in space-charge region, we first assume the space-charge will not be changed. Comparing with the space-charge in thermal equilibrium, as demonstrated by 2.52, we can immediately note that the second term in the bracket of 2.59 is always positive and, consequently, the space-charge function will become smaller than that in the dark, which leads to a decreasing of surface band bending, as illustrated in **Figure 2.4** (a), i.e. the surface band bending tends to vanish upon illumination. Eventually, the bands will become flat at sufficient illumination-intensity and the corresponding SPV can be interpreted as reflecting the magnitude of surface band-bending in thermal equilibrium.

The above discussion provides a simplified picture where the space-charge is considered unchanged upon photo-excitation. However, it is worth noting that, in a more general case, both space-charges and surface states may change, possibly significantly, upon illumination, though the total charges remain constant. For the case of donor type surface states on p-type semiconductor surface, as shown in **Figure 2.3**, illumination will result in an increase of surface states, leading to a decrease of space-charge density. Comparing the space-charge density in dark and under illumination, one would note a smaller $F(v_s, u_b)$ upon illumination, which subsequently, gives rise to decreasing of surface band bending, i.e. band flattening upon illumination. The detailed analysis can be found in previous studies,[82, 105] which involves sophisticated case-by-case treatments.

Note that the SPV-induced shifts in energy levels discussed in this thesis only concerns the potential change in the space-charge region. It does not involve light induced photochemical reaction, giving rise to shifts due to the changes in the surface and/or bulk chemical composition or bonding.

2.2.4 **Vacuum level alignment**

Vacuum level alignment (VLA), also known as the Schottky-Mott limit, occurs when there is no rearrangement of electric charges across the interface. This typically holds for non- or weakly interacting interfaces.[76] In this case, the energy offset between two contacting semiconductors can be well predicted by assuming the alignment of vacuum level. This is schematically illustrated in **Figure 2.6** for an energy level alignment at an inorganic/organic interface, where the energy offset for electrons and holes can be estimated as the difference in electron affinity (ΔEA) and ionization energy (ΔIE), respectively. In such a case, a favored energy level alignment can be predictably achieved by choosing a known semiconductor material with appropriate EA and/or IE.

It is very clear that this ELA scheme, i.e. the Schottky-Mott limit holds, only if the substrate's Fermi level comes to lie within the highest occupied molecular orbital (HOMO) and the lowest unoccupied molecular orbital (LUMO), as shown in **Figure 2.6**. This can be characterized from the parameter S *(=1)* that is defined as $S = dE_F/d\Phi_{sub}$, where Φ_{sub} is the substrate's work function and E_F is the Fermi level of the organic semiconductor. It is noted that for interfaces where "push-back" and/or chemisorption occurs, the parameter S can be different than 1 for the case of VLA.[68, 75] In the other case, by and large, in contrast to the VLA situation, there often exists abrupt changes in the vacuum level when bringing two materials into contact. Such change has been largely attributed to interface dipole and/or

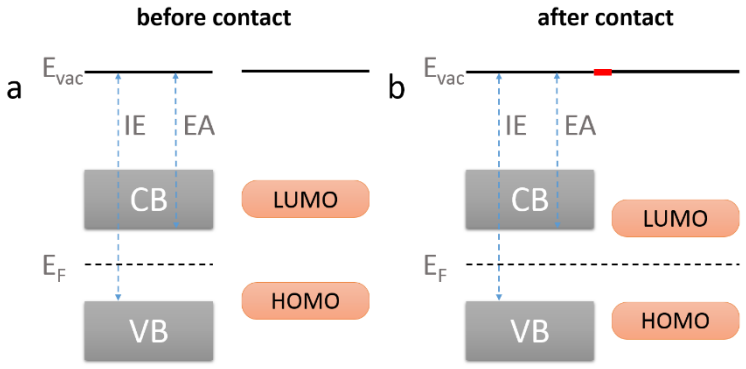

Figure 2.6 *The energy level diagrams for the case of vacuum level alignment at an organic-inorganic interfaces. (a) before contact and (b) after contact.*

band bending resulting from interfacial charge density rearrangements upon contact formation.[11, 61, 64, 68] In the following, the phenomenon of Fermi level pinning will be briefly introduced.

2.2.5 **Fermi level pinning**

Generally, Fermi level pinning refers to a situation in which the energy levels become fixed, giving rise to constant energy offset at the interface and/or surface. This is schematically shown in **Figure 2.7** (b) for the situation where the common Fermi level is

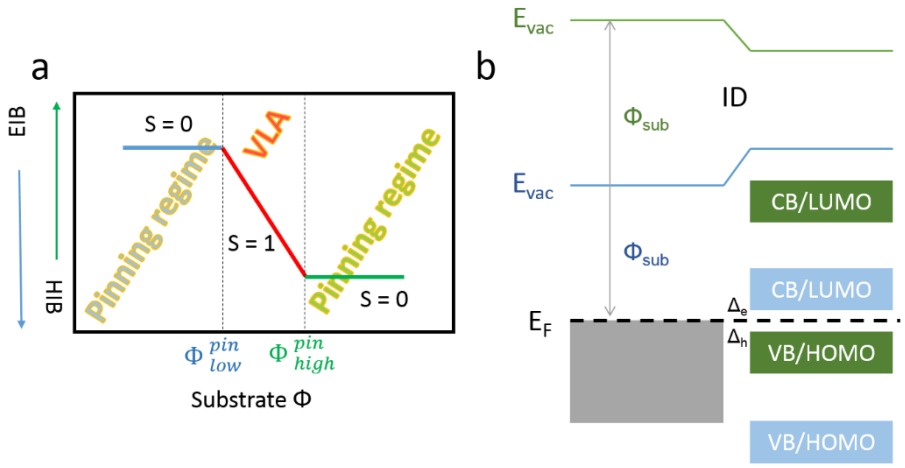

Figure 2.7 *(a) Schematic relationship plot between the hole injection barrier (Δ_h or HIB)/electron injection barrier (Δ_e, EIB) and substrate work function (Φ_{sub}). In the VLA regime (S = 1), the HIB or EIB can be manipulated by varying the substrate Φ_{sub}, while in Fermi level pinning regime (S = 0), the HIB or EIB is independent of the substrate Φ_{sub}. (b) Energy level diagrams between metal/semiconductor interfaces within the model of Fermi level pinning. Fermi level pinning at CB/LUMO (or VB/HOME) occurs if the substrate Φ_{sub} is smaller (or larger) than electron affinity (ionization energy) of the organic layer, in this case, the electrons (or holes) will flow into the organic layer in order to reach electrostatic equilibrium, i.e. Fermi level alignment.*

pinned at (or close to) the LUMO (or HOMO) of the organic layer. In such a case, pronounced charge transfer and, subsequently, steep potential changes cross the interface are observed. As a result, the parameter *S* equals 0, meaning no dependence on substrate Φ_{sub}.

Such phenomenon can be understood from the density of states controlled energy level alignment mechanism.[111] Upon forming an interface with two different materials, the electrostatic equilibrium requires Fermi level alignment instead of vacuum level alignment. The situation occurs that the LUMO (or HOMO) of the organic layers lies below (or above) the Fermi level of the substrate when apart from each other. Upon bringing them into contact, following Fermi-Dirac statistics, filling up of empty LUMO states (or emptying of HOMO states) occurs resulting in pinning of these states at the common Fermi level, which is accompanied by the formation of an interface dipole and/or band bending.[11, 57, 68, 111, 125, 158, 165] Such process is referred as Fermi level pinning. The respective pinning levels, i.e. Φ_{low}^{pin} and Φ_{high}^{pin} for LUMO or HOMO, respectively, are often specific for different organic semiconductors. This is schematically illustrated in **Figure 2.7** (b), where the CB/LUMO (or VB/HOMO) is fixed at (or close to) substrate Φ, giving rise to constant electron injection barrier (Δ_e, or hole injection barrier, Δ_h). The Fermi level pinning process at metal/semiconductor interface is valid for either inorganic or organic materials.

3 Fundamentals of halide perovskites

In this chapter, the fundamental properties of the halide perovskites will be introduced and discussed. Starting with the section 3.1, the basic structural parameters with respect to the 3D perovskites and their phase transition properties will be firstly introduced. The electronic band structure of the halide perovskites, which has been largely investigated theoretically, is then explicitly discussed in section 3.2. With the knowledge of band structure of perovskites, the optoelectronic properties can be better understood. In the following section 3.3, some important parameters, which have been experimentally determined, such as absorption coefficient and charge-carrier related parameters will be presented. Subsection 3.4 will summarize the methods of film preparation, as it is the key to achieve high quality perovskite films. Finally in section the 3.5, application and development of perovskites in the field of photovoltaics will be summarized.

3.1 Crystal structure

The structure term of "perovskite" originates from a class of mineral crystal structures of the form ABX_3, where the typical example is $CaTiO_3$, consisting of a corner-sharing BX_6 octahedral network and A cations in the interstices.[156] As shown in **Figure 3.1**, organic-inorganic hybrid perovskites adopt the "perovskite" crystal structure, where the A is a

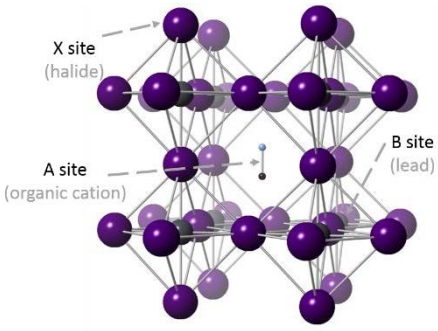

Figure 3.1 *Schematic crystal structure of a prototypical 3D HaPs.*

monovalent cation, which was initially organic cations [for example, methylammonium (MA or $CH_3NH_3^+$) or formamidinium (FA or $(CH_2)_2CH^+$)], B is typically lead (Pb), and X represents halide [iodine (I), bromine (Br) and chlorine (Cl)]. For brevity, we will refer the HaPs as perovskites in the following chapters. The perovskite family can be extended to a certain degree by substituting and/or mixing of, in principle, every component while maintaining the tolerance factor between 0.8 and 1.0 (according to Goldschmidt the tolerance factor is defined as $\alpha = \frac{r_A + r_X}{\sqrt{2}(r_B + r_X)}$, where r_i being the radii of the ions in ABX_3).[46] Further expanding the size of the cations breaks the 3 dimensional (3D) structure into lower dimensionalities, when this is proceeded in a controlled manner, 2D or even 1D perovskites can be formed.[26, 144, 149] Therefore, the complexity in composition enables the tunability of the material's properties for many applications. In this thesis, we will only focus on 3D-based perovskites.

Studies on the crystal structure of perovskite materials have revealed that the structure undergoes phase transitions upon changing the temperature (*T*). It was reported that depending on the $CH_3NH_3^+$ orientation, $MAPbI_3$ exhibits structural transitions upon increasing the *T* from orthorhombic *Pnma* phase below ~160 K to tetragonal *I4/mcm* phase (*T* within ~160 to 330 K), and to cubic *Pm-3m* phase above ~330 K.[117, 155, 157] It was demonstrated that in the low temperature phase, the MA cation is fully ordered, giving a fixed position in the PbI_6 octahedral cage; Upon increasing the temperature, the MA cation cannot be fixed due to the cubic symmetry, which becomes partially ordered at tetragonal phase and fully disordered at cubic phase, accompanied by a slight distortion of the PbI_6 cage.[117, 155, 157] Temperature-dependent structural transitions also occur for other perovskite systems, e.g. $MAPbBr_3$ and $MAPbCl_3$ systems, with the structural data summarized in **Table 1**.

Table 1. T*emperature-dependent structural parameters of three prototypical $MAPbX_3$ (X = I, Br, Cl). Data are taken from [117, 157]*

	Temperature (°C)	**Crystal system**	**Lattice (Å)**
$MAPbI_3$	> ~327	cubic	a = 6.328
	162 - 327	tetragonal	a = 8.855, c = 12.659
	< ~162	orthorhombic	a = 8.861, b = 8.581, c = 12.620
$MAPbBr_3$	> ~237	cubic	a = 5.901
	155 - 237	tetragonal	a = 8.322, c = 11.832
	150 - 155	tetragonal	a = 5.894, c = 5.861
	< ~145	orthorhombic	a = 7.979, b = 8.580, c = 11.849
$MAPbCl_3$	> ~ 179	cubic	a = 5.675
	173 - 179	tetragonal	a = 5.656, c = 5.630
	< ~173	orthorhombic	a = 5.673, b = 5.628, c = 11.182

3.2 Electronic structure of halide perovskites

The electronic structure of HaPs, which is at the core of understanding the intrinsic optoelectronic properties, has been largely investigated by the means of density functional theory and many-body perturbation theory.[14, 37, 42, 98] As revealed by DFT calculations for $MAPbI_3$ as the prototype of HaPs material, the top valence bands are found to be composed mainly from σ-antibonding states of Pb 6*s* and I 5*p* orbitals, and the bottom conduction band is found to consist of σ-antibonding states of Pb 6*p* and I 5*s* orbitals,[146] as presented in the **Figure 3.2**.

Band calculations have demonstrated that the lowest unoccupied states and highest occupied states, which are more relevant for the charge-transport properties, are composed

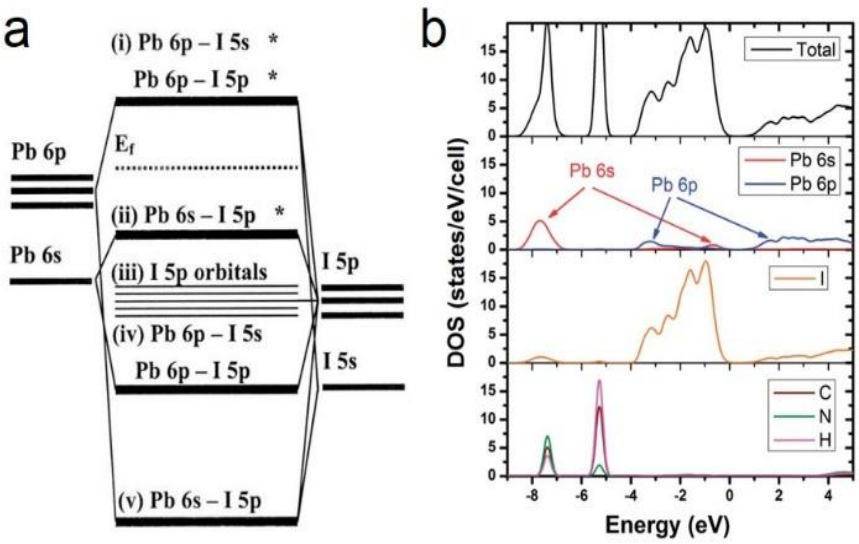

Figure 3.2 *(a) Bonding diagram of a $[PbI_6]^{-4}$ cluster. Reproduced with permission from Umebayashi et al.[146] (b) Density of states (DOS) of tetragonal phase $MAPbI_3$ calculated using Perdew-Burke-Ernzerhof (PBE) functionals. The valence band maximum is set to zero. Reproduced with permission from Du.[30]*

of hybridization states only from Pb and I orbitals, as shown in **Figure 3.2** (b). Thus, the cations do not contribute directly to the frontier bands. The band structure of cubic phase $MAPbI_3$, as a prototype HaPs material, is shown in **Figure 3.3**. From the electronic band structure, which was calculated with the DFT theory taking spin-orbit coupling into account, it can be seen that the cubic $MAPbI_3$ exhibit a direct-gap, meaning the valence band maximum (VBM) and conduction band minimum (CBM) occur at the same Brillouin zone *k*-position. This particular property is one of the key ingredients for the efficient charge-carrier generation, as this process does not require assistance of phonons. Additionally, studies have found the giant spin-orbit splitting, which might account for the long lived charge carriers within the materials.[110, 177] Note that HaPs materials often experience phase transition upon changing the temperature, as discussed in section 3.1. Therefore, the electronic band structure can be slightly modified, however, the direct band gap property seems independent of the phase.[12]

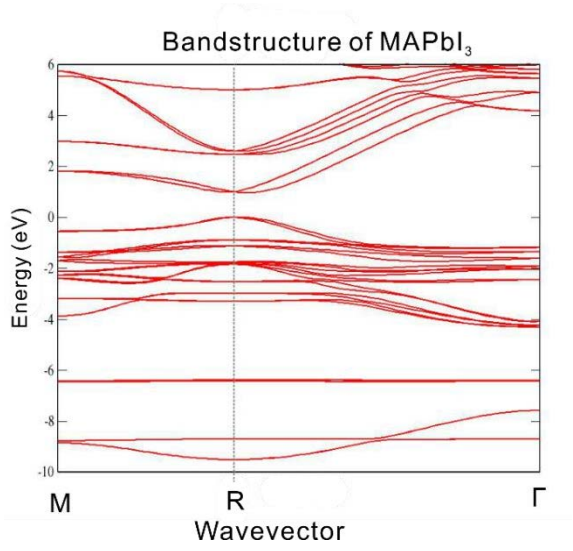

Figure 3.3 *Band structure of cubic-phase MAPbI3 calculated with DFT theory. M and R denote the boundary points close to (1/2,1/2,0) and (1/2,1/2,1/2), respectively. The VBM and CBM are slightly shifted away from R as a result of spin-orbit coupling. The VBM is set zero. Band calculation was performed by Dr. David Egger (Universität Regensburg).*

3.3 Optoelectronic properties

As we briefly discussed in the introduction, the unprecedented development of HaPs materials into wide range of applications, particularly in PVs, has benefited primarily from their excellent optoelectronic properties. This is demonstrated from their high absorption coefficient,[22] low exciton binding energy (comparable or even smaller than k_BT at RT),[41, 103] high charge carrier mobility,[54, 171] long diffusion length,[177] and so on. These properties are summarized in **Table 2**, together with other prototypical photovoltaic materials for comparison, including inorganic and organic semiconductors.

Among these optoelectronic properties, **Figure 3.4** shows the effective absorption coefficient of $MAPbI_3$ thin films, together with other prototypical photovoltaic materials, including crystalline silicon and GaAs. It can be clearly seen that the $MAPbI_3$ thin films present a particularly sharp absorption edge, with an Urbach energy of ca. 15 meV. The absorption coefficient for $MAPbI_3$ is found to be in the order of 10^5 cm^{-1}, very comparable to that of GaAs owing to the direct bandgap character of these materials.[22] In contrast, the absorption spectrum of polycrystalline Si shows 1-2 order of magnitude less in absorption coefficient in the visible light range with a large Urbach tail owing to their indirect bandgap. Another important fact is that the HaPs exhibit relatively small effective

mass, similar to those of well-known inorganic PV materials, e.g., similar to that of the crystalline Si. However, experimentally, the mobility of the HaPs is determined to be much smaller than that of Si. This particular property, which was recently brought into discussion, will be dealt with in section 6.2.

Table 2. *Some basic parameters of the optoelectronic properties for two prototypical perovskite systems, together with other photovoltaic systems.*

Materials	**Absorption coefficient (cm^{-1})**	**Diffusion length (μm)**	**Mobility ($cm^2V^{-1}s^{-1}$)**	**Effective mass* (m_0)**	**References**
$MAPbI_3$ crystals	~ 10^5	2 - 8	2 - 164	e^- / h^+ 0.24-0.50	[12-13, 22, 54, 164, 185]
$MAPbBr_3$ crystals	~ 10^5	3 - 17	24 - 115	e^- / h^+ 0.25-0.59	[12-13, 47, 54, 152, 185]
Si	10^3 ~ 10^4	e^- 10^3 h^+ 600	1450 500	0.19 0.16	[12, 118]
GaAs	~ 10^5	e^- 7 h^+ 1.6	8000 400	0.063 0.076	[7, 12, 22]
Organic crystals	~ 10^5	~ 0.05	~ 1	e^- / h^+ 1.4-6.4	[17, 92, 112, 161]

In addition, technically, these remarkable optoelectronic properties can be achieved with low-cost and low-temperature solution-processing methods, which makes HaPs-based devices very promising for commercialization. Therefore, fundamental understanding of their unique structural and optoelectronic behavior is of paramount importance to further push the HaPs-based devices into application. In contrast to the rapid development of the device performances, many fundamental questions regarding, for example, role of organic

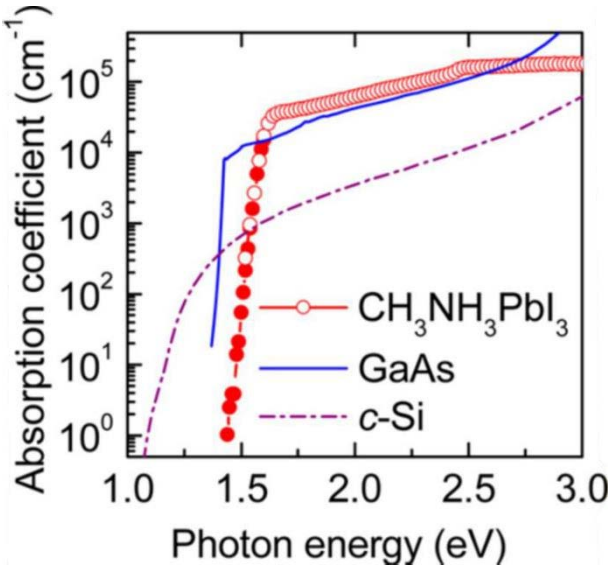

Figure 3.4 *Effective absorption coefficient of a $MAPbI_3$ thin film, crystalline silicon (a-Si) and GaAs at room temperature. Figure reprinted with permission from Wolf et al.[22]*

cations,[40, 108, 163, 182] role of defects[29, 31, 72, 169], the charge-carrier scattering and transport mechanism,[69, 181, 183] and low non-radiative recombination rate,[135-136, 138] still remain.

3.4 Film formation and engineering

The preparation methods of halide perovskites have been developed from a range of different deposition routes. Depending on the fabrication process, it can be generally categorized into three methods: 1) vacuum deposition[89] 2) solution processing[16, 35] and 3) hybrid vapor-solution process.[19, 87] Obviously, vacuum deposition requires the starting materials to be thermally evaporated in a vacuum chamber, for instance, by co-evaporating inorganic compounds $PbCl_2$ and organic compounds MAI to obtain mixed halide perovskite $MAPbI_{3-x}Cl_x$. The films prepared from this method feature full coverage and homogenous crystallites with the size on the scale up to micrometer.[19, 87] In addition, relatively large scale production can be achieved using this method. Solution-processing method has been widely and commonly used to fabricate perovskite films because of its simplicity and low-cost. Devices employing this method can easily achieve high performance owing to the fast crystallization process of the perovskite materials.[179] However, the films often suffer poor morphology and reproducibility issues. Besides, it is also very challenging to obtain large area with sufficient reproducibility. As for the hybrid

vapor-solution process, it basically involves both techniques mentioned above. As a result, perovskite films with superior uniformity over a range of scales can be obtained, but such method complicates the manufacturing process.

Recently, the necessary treatments (steps) require more than above mentioned basic processes in order to obtain high quality perovskite films in terms of device performance. Such treatments consist of varying precursor stoichiometry,[83] implementing of additives,[88, 187] optimizing processing atmosphere,[178] solvent engineering[24, 53] and so on. In short, it is essential to fabricate high quality films with controlled morphology and crystallinity in order to obtain high performance in functional devices. The crystallization process, which directly affects charge transport properties in resulting perovskite films, is highly dependent on numerous factors as just discussed in this section.

3.5 Applications in solar cells

The first attempt to use the halide perovskite as sensitizer was started with dye-sensitized liquid-type solar cells in 2009, however, little attention was payed due to its poor PCE of ca. 3%.[78] Two years later, PCE of 6.5% was reported by Park's group with great improvement in stability.[63] Soon after that, the perovskite "fever" started followed by the realization of the full solid-state perovskite solar cell in 2012 with a PCE of 9.7% exhibiting even longer stability.[71] Over the last few years, the efficiency has being pushed forward

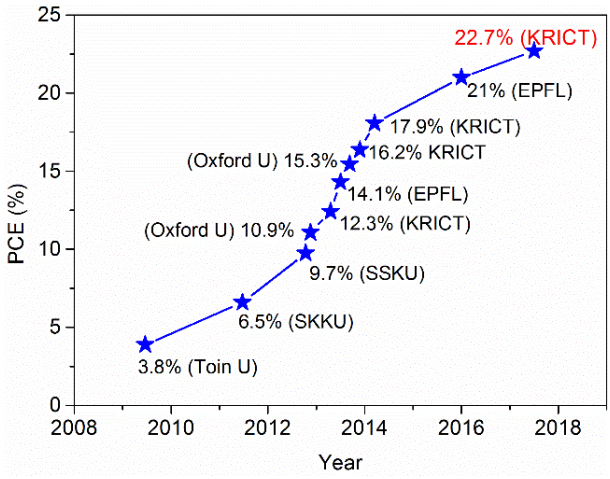

Figure 3.5 *Progress in efficiency for single-junction perovskite solar cells. Efficiency values were taken from Ref[115] and from NREL's latest efficiency chart.[59]*

in such a speed that the photovoltaic industry has never witnessed before, as summarized in the efficiency chart in **Figure 3.5**.

4 Fundamentals of experimental techniques

4.1 Low-energy electron diffraction (LEED)

Low-energy electron diffraction (LEED), is a powerful tool for detailed surface crystallographic study with low perturbation.[100] The instrument, which is schematically presented in **Figure 4.1** (a), consists of an electron gun, a phosphorous screen and focusing grids. A charge-coupled device (CCD) camera is used to record the images. In this experiment, following the de Broglie wavelength of $\lambda = h/p$, an incident beam of electrons with primary energy typically within 20 - 300 eV impinges on the sample surface in normal direction. The intensity of elastically backscattered electrons will vary with diffraction angle θ depending on constructive or destructive interference.

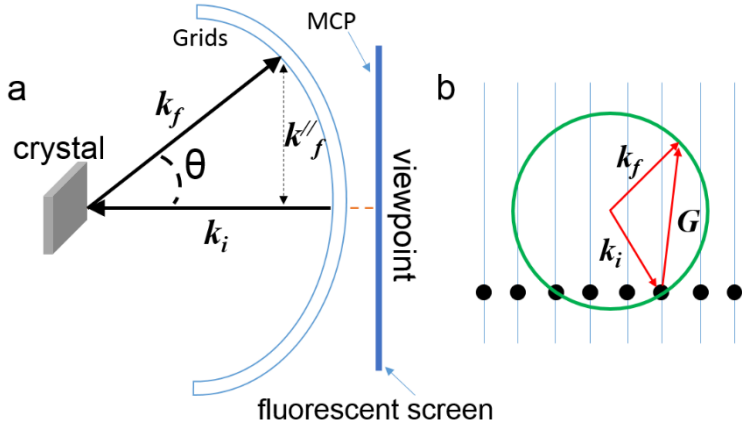

Figure 4.1 *(a) A schematic diagram of a MCP-LEED (micron-channel plates) apparatus with planar display. Electron trajectories are indicated by arrows. Retarding and subsequent accelerating grids in front of the fluorescent screen are generally applied in order to suppress the inelastic scattered electron and compensate the intensity drop, respectively. (b) Construction of Ewald's sphere for a 2D lattice. The allowed diffraction spots are determined by the intersections between Ewald's sphere and reciprocal lattice.*

From the kinematic theory, the condition for occurrence of a diffraction pattern follows the Laue equation in reciprocal space:

$$\boldsymbol{k_f} - \boldsymbol{k_i} = \boldsymbol{G} \qquad 4.1$$

where $\boldsymbol{k_f}$ and $\boldsymbol{k_i}$ are the final and initial wave vector, respectively, and $\boldsymbol{G}$ the reciprocal lattice vector. This relation can be illustrated by a Ewald's construction as shown in **Figure 4.1** (b). The amplitude of the initial wave vector does not change, i.e. $|\boldsymbol{k_i}| = |\boldsymbol{k_f}|$. As the mean free path of the low energy electrons in a crystal is generally within a few angstroms, only the very surface atomic layers contribute to the LEED pattern.[60] From **Figure 4.1** (b), we can anticipate that the LEED pattern is a direct picture of the reciprocal lattice, hence, the real space lattice and surface structure can be reconstructed.

We can now apply these concepts to a LEED experiment. The electron beam hits the surface at normal direction, i.e. $\boldsymbol{k}_i^{//} = 0$. Under such condition, the diffraction can be directly related to the surface reciprocal lattice, such that $\boldsymbol{k}_f^{//} = \boldsymbol{G}$. We can, therefore, calculate the position of the diffraction points on the viewpoint for the case of a cubic lattice, which is given as

$$\sin\theta = |\boldsymbol{k}_f^{//}|/|\boldsymbol{k_f}| = n\frac{2\pi}{a|\boldsymbol{k_f}|} = n\frac{\hbar 2\pi}{a\sqrt{2m_0E_{kin}}} \approx n\frac{2\pi}{a(0.512\sqrt{E_{kin}})} \qquad 4.2$$

where the n is the order of diffraction and E_{kin} the kinetic energy of the incident electrons. Knowing the geometry of the LEED apparatus, i.e. radius of the fluorescent screen and the distance between the sample and the screen, the diffraction angle θ can be calculated from the diffraction spots. Thus, the lattice constant can then be determined. One can already anticipate that with increasing the electron energy, the diffraction spots will shrink towards the center of the screen, and there is a minimum threshold electron energy in order to see the diffraction pattern.

4.2 Macroscopic Kelvin probe (KP)

The principle of Kelvin probe method was first introduced by Lord Kelvin in 1898.[70] It was shown that a potential is established when two different electrodes are brought into contact. If two materials with different work functions are brought together, electrons will flow from the low work function to high work function sides in order to reach electrostatic equilibrium. It is schematically shown in **Figure 4.2** that the contact potential difference (CPD) can be determined by measuring the charge flow. By vibrating the probe, the capacitor is vibrated periodically such that an AC current is generated. The AC current can be formulated as

$$i = \frac{d}{dt}[C(t)V_C(t)] \qquad 4.3$$

where $C(t) = \frac{\varepsilon_0 \varepsilon_r A}{d(t)} = \frac{\varepsilon_0 \varepsilon_r A}{d_0 + d_1 \sin(\omega t)}$, ε_0 is the permittivity in vacuum, ε_r (=1 in vacuum) the relative permittivity, A the capacitance effective area, d_0 the average distance between the tip and sample surface, d_1 the amplitude of vibration and ω the vibration frequency. $V_C(t)$ is the total voltage on the capacitor. This equation can be further simplified as

$$i = (V_{CPD} + V_b)\frac{d}{dt}C(t) \qquad 4.4$$

Experimentally, the DC bias can be varied until the AC current is nullified. Thus V_{CPD} will equal to the applied bias V_b.

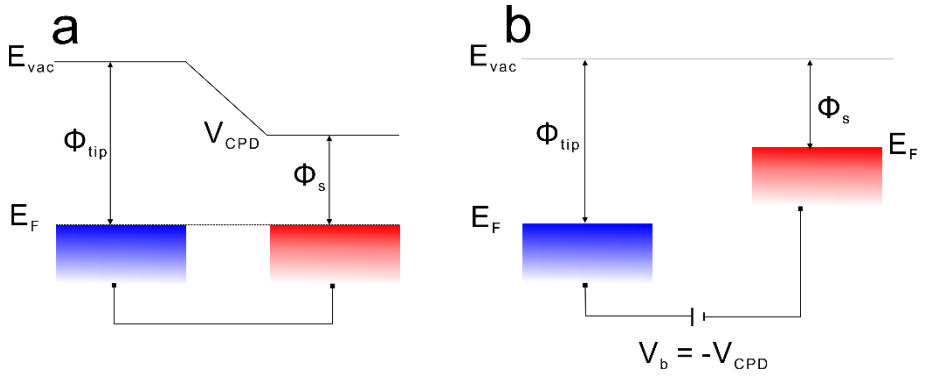

Figure 4.2 *Schematic band diagrams of two different conductors (a) in contact and (b) when an external bias is applied such that the capacitor is discharged.*

4.3 Photoelectron spectroscopy (PES)

Photoelectron spectroscopy (PES), generally speaking, is a technique to investigate the electronic structure of a system. It is based on the photoelectric effect, in which a photon of energy *hv* excites an electron away from the solid. In order to describe the photoemission process, different models have been applied to describe the electronic structure of the solids in the initial and final states.[10, 15, 51, 85, 133, 150] Thus, this section will introduce some of the theoretical approximations in order to explain the complicated photoemission process. Among different approaches, the one-step model, or the so-called time-reversed LEED state,[143] is able to treat the photoemission process very accurately, however, the accuracy highly depends on the level of sophistication and the extent to which the many-body effects are taken into account.[10]. In contrast, the three-step model,[85, 133] which has been widely and successfully applied, makes the photoemission process intuitively understandable and will be briefly introduced in this chapter. The theory in this chapter is mainly inspired from the discussion by Suga, Sekiyama and Hüfner.[60, 141]

4.3.1 Three-step considerations

The three-step model can be generally divided into three individual steps:

1. Photoexcitation of an electron inside a solid,

2. Propagation of the photoelectron to the solid surface,

3. Emission of the photoelectron into the vacuum.

The overall photoemission intensity is then proportional to the product of the probabilities of each step. If the probabilities for each step are denoted by P(E, $h\nu$), T(E, $h\nu$) and D(E), respectively, the photoemission intensity is thereby proportional to

$$P(E, h\nu)\cdot T(E, h\nu)\cdot D(E) \qquad 4.5$$

1. Photoexcitation probability. This process involves the absorption of incident photons

and creation of photoelectrons. Such process can be approximated from Fermi's golden rule, from which the photoexcitation or transition probability per unit time is given as

$$\frac{dP}{dt} = \frac{2\pi}{\hbar}|< \varphi_f|\boldsymbol{H}|\varphi_i > |^2[\delta(E_f - E_i - h\nu)] \quad 4.6$$

Given the small perturbation induced by incident radiation, the full Hamiltonian can be formalized as

$$\boldsymbol{H} = \boldsymbol{H_0} + \frac{e}{2mc}(\boldsymbol{A}\cdot\boldsymbol{P} + \boldsymbol{P}\cdot\boldsymbol{A}) - e\Phi + \frac{e^2}{2mc^2}|\boldsymbol{A}|^2 \quad 4.7$$

where **A** and Φ are the vector and scalar potentials of the incident light field, and **P** the momentum operator $\boldsymbol{P} = i\hbar\boldsymbol{\nabla}$. If one assumes the amplitude of the incident light being very small, i.e. Φ = 0, and neglects the term $\boldsymbol{A}\cdot\boldsymbol{A}$ and $\boldsymbol{\nabla}\cdot\mathbf{A} = 0$. Given the relation $\boldsymbol{A}\cdot\boldsymbol{P} + \boldsymbol{P}\cdot\boldsymbol{A} = 2\boldsymbol{A}\cdot\boldsymbol{P} + \boldsymbol{\nabla}\cdot\mathbf{A}$**,** one obtains

$$\boldsymbol{H} = \boldsymbol{H_0} + \frac{e}{mc}\boldsymbol{A}\cdot\boldsymbol{P} \quad 4.8$$

2. Propagation function. This process involves the propagation of photoexcited electrons to the surface. The propagation function T(E, $h\nu$) can be generally expressed as a function of the absorption coefficient α($h\nu$) and the electron inelastic mean free path (IMFP) *λ(E)*, and is given as[141]

$$T(E, h\nu) = \frac{\alpha(h\nu)\lambda(\mathrm{E})}{1 + \alpha(h\nu)\lambda(\mathrm{E})} \quad 4.9$$

The electron IMFP dependence is shown in **Figure 4.3**,[129] and can be described by the

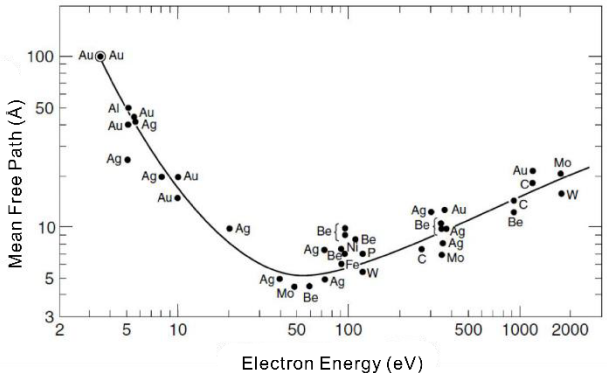

Figure 4.3 *Electron inelastic mean free path as a function of the kinetic energy for different material systems. Figure reproduced from [175]*

Lambert-Beer law $I(d) = I_0 e^{-d/\lambda(E)}$, where $\lambda(E)$ is the distance at which the electrons intensity attenuated to $1/e$ of the primary intensity I_0. It can be seen that energy dependence of the IMFP is independent of the material systems and normally results in 1-10 Å for the energy of 10-200 eV in most material systems. Therefore, the valence band photoemission spectra will mainly reflect the electronic structure of the solid surface region. However, one could increase the bulk contribution by tuning the photon energy, e.g. by using photon energy of more than 600 eV.

3. Escaping of the photoelectron into the vacuum. The last step consists of the emission of photoelectrons into vacuum. It is apparent that the electrons have to be emitted through the solid surface, and the electrons must overcome the surface potential barrier.

The process leaves the parallel component of the electron wave vector conserved, which is given as $\mathbf{K}_{//} = \mathbf{k}_{//} + \mathbf{G}$, $\mathbf{k}_{//}$ denotes the wave vector inside of the solid and $\mathbf{K}_{//}$ in the vacuum. The process is illustrated in **Figure 4.4**.

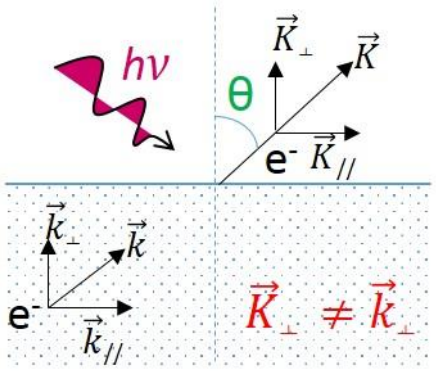

Figure 4.4 *Electron momentum relation at the solid-vacuum interface. During the photoemission process, the parallel electron momentum is conserved while the perpendicular wave vector changes.*

4.3.2 Valence-states and core-level photoemission

The basic principles of the photoemission process were briefly discussed in the above session. Details regarding the theory are referred to the textbooks and review articles.[10, 15, 51, 60, 85, 133, 141, 150] In the following, two typical photoemission experiments, i.e. valence-states and core-level photoemission, will be presented. Following the photoelectric effect, the basic equation of photoemission process can be written as

$$E_{kin} = h\nu - \phi_s - E_B \qquad 4.10$$

where the E_{kin} is the kinetic energy of the emitted photoelectrons, $h\nu$ the incident photon energy and ϕ_s the work function of the sample.

A typical photoemission spectrum is schematically illustrated in **Figure 4.5**, for a semiconductor, where the occupied DOS, the work function (Φ) and ionization energy of the semiconductor can be accessed. It should be noted that what is really measured by the

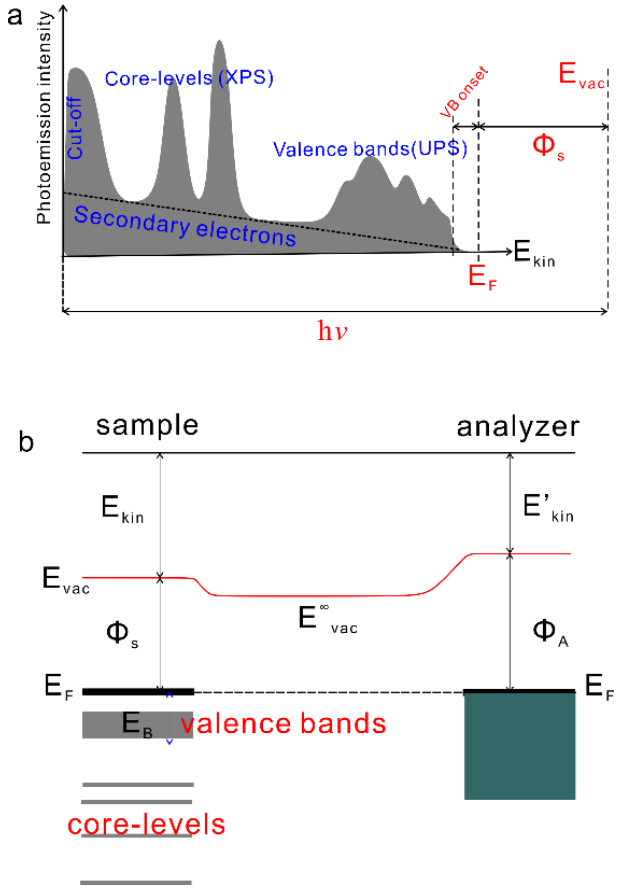

Figure 4.5 *(a) Schematic of a typical photoemission spectrum of a semiconductor. (b) Schematic energy level diagram for the interconnected sample-analyzer system. E_B denotes the binding energy with respect to Fermi-level. E_{vac} and E^{∞}_{vac} are vacuum levels in vicinity of the sample and at infinity, respectively.*

electron analyzer is the electrons that experienced the contact potential difference between the sample and the analyzer, and it is clearly demonstrated in **Figure 4.5** (b). As a result, the experimentally measured kinetic energy of the photoelectrons can be rewritten as

$$E'_{kin} = h\nu - \phi_A - E_B \qquad 4.11$$

The electrons with highest kinetic energy originate from the top occupied states, which are from the Fermi-level for a metal and top valence bands/HOMO for a semiconductor. The slowest electrons with the lowest kinetic energy are the secondary electrons, which have lost their energy in the propagation processes, and barely made it out of the sample. In order to detect those electrons, a negative bias is normally applied to the sample. In this way, the work function of a sample can be determined.

Ultraviolet photoelectron spectroscopy is the most commonly used technique to investigate the valence bands electronic structure, where the band dispersions and hybridization states can be studied in great detail.[57, 77, 145] UPS measurements, combined with synchrotron radiation, offer widest applications in the study of electronic structure for functional materials.[77, 93] For one case, one can access the hole injection barrier (HIB) by analyzing the frontier bands and/or molecular orbitals at the metal/semiconductor interfaces,[68] which can be given as $HIB = IE - \phi_{metal}$.

X-ray photoelectron spectroscopy, by irradiating the sample with photons at high energies (at least few hundreds of eV), probes the atomic core-levels of a solid. Because each element has a unique set of binding energies, XPS can be generally applied to identify and quantify the elements in a sample.[65] Laboratory X-ray sources for XPS measurements are the X-ray K-alpha line at 1486.6 eV using an aluminum anode and at 1253.6 eV using a magnesium anode. XPS spectra can be used to identify elements and access the chemical states of the compounds from the variations in binding energies and lineshapes,[43-44, 48] as exemplified in **Figure 4.6** for C 1s in ethyl trifluoroacetate compounds. It can be clearly seen that due to different chemical environment experienced

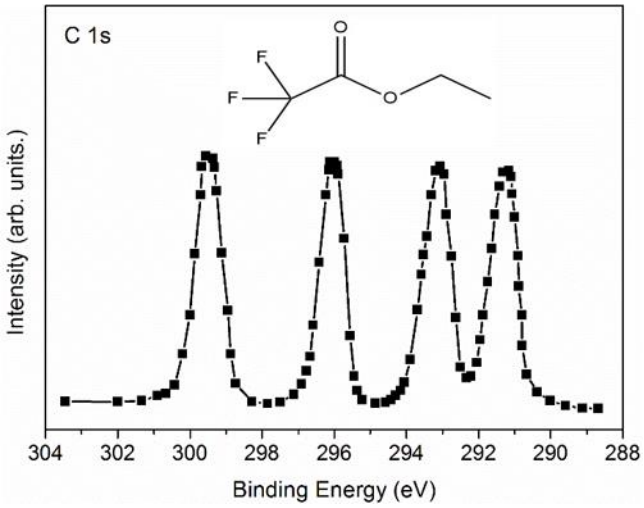

Figure 4.6 *XPS core-level spectrum of C 1s of ethyl trifluoroacetate. Large variations in binding energy for C 1s at different chemical bondings. Inset: chemical structure of ethyl trifluoroacetate. Data extracted from reference[44]*

by carbon, C 1s exhibits variations in binding energies.[44]

In addition, XPS measurements would also be able to determine the relative atomic concentration of the constituents. The intensity of photoelectrons emitted from a homogeneous sample and collected by the analyzer can be given as [65]

$$I = n \cdot I_{flux} \cdot \sigma \cdot \lambda \cdot \theta \cdot T(E_{kin}) \qquad 4.12$$

where n is the number of atoms of the element per cm^3, I_{flux} the X-ray flux, σ the photoelectron cross-section for the atomic orbital of the interest, λ the mean free path of the emitted electrons, θ the angle efficiency factor based on the angle between the incident beam and emitted electrons and $T(E_{kin})$ the spectrometer transmission function. From above discussion, relative atomic ratio between A and B elements in a sample can be given as

$$\frac{n_A}{n_B} = \frac{I_A/S_A}{I_B/S_B} \qquad 4.13$$

$S_X = \sigma \cdot \lambda \cdot \theta \cdot T(E_{kin})$ is defined as atomic sensitivity factor, which can be found in great detail in reference [151].

4.3.3 Angle-resolved photoelectron spectroscopy (ARPES)

In ARPES, the study of the energy and angular dependence of the photoemitted electrons allows us to access the electronic band structure of the solids. Given the three-step model, the kinetic energy and wave vector of the collected electrons can be described in the following relations. Firstly, it is straightforward to write down the parallel component which is conserved during the photoemission process,[60]

$$\frac{|\boldsymbol{p}_{//}|}{\hbar} = |\boldsymbol{K}_{//}| = |\boldsymbol{k}_{//} + \boldsymbol{G}| = \sqrt{\frac{2m_0}{\hbar^2} E_{kin}} sin\theta \approx 0.51 \text{Å}^{-1} \sqrt{E_{kin}(eV)} sin\theta \quad 4.14$$

where $\mathbf{K}_{//}$ is the parallel wave vector of the emitted electrons, $\mathbf{k}_{//}$ the parallel wave vector of the photoexcited electrons in the crystal, **G** the wave vector in the reciprocal lattice, m_0 the free electron mass and, θ the photoelectron emission angle with respect to the surface normal (polar angle).

The process regarding the perpendicular momentum $\mathbf{K}_{\perp}$ is more complex, because there is no direct relation between wave vector outside $\mathbf{K}_{\perp}$ and inside $\mathbf{k}_{\perp}$ of the solids. The general and simple approach is to treat the final states using a free-electron model,[60] thus the perpendicular wave vector can be expressed as

$$|\boldsymbol{k}_{\perp}| = \sqrt{\frac{2m^*}{\hbar^2} E_{kin} cos^2\theta + V_0} \quad 4.15$$

V_0 presents the potential barrier which photoelectrons have to overcome in order to cross the surface, m* is the effective electron mass where m_0 is normally employed. Therefore, from equation 4.14 and 4.15, the band dispersions along $\mathbf{k}_{//}$ and $\mathbf{k}_{\perp}$ can be accessed experimentally by changing the polar angle θ and by varying the incident photon energy (i.e. changing kinetic energy $\mathbf{E}_{kin}$), respectively. The schematic process is illustrated in **Figure 4.7**. The free-electron model can be a very good approximation for the final states if applying a high excitation energy, as the effect of the crystal potential becomes weaker. However, one has to note that further increase of excitation energy (up to ca. 100 - 150 eV)

leads to a decrease of the electron mean free path which can result into intrinsic wave vector broadening.[139]

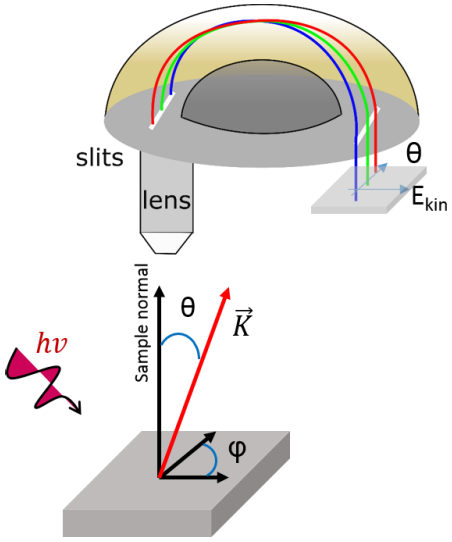

Figure 4.7 *Schematic view of an ARPES setup equipped with a 2D analyzer. θ and φ are the polar angle and azimuthal angle, respectively.*

5 Materials and experimental setups

5.1 Materials and sample preparation

$CH_3NH_3PbI_{3-x}Cl_x$ thin films. The perovskite precursor was prepared by mixing methylammonium-iodide (MAI) with lead chloride ($PbCl_2$, Sigma-Aldrich, anhydrous, 99.999%) in anhydrous N, N-dimethylformamide (DMF) (Sigma-Aldrich, anhydrous, 99.8%) solvent at 3:1 molar ratio for a final concentration at 30 wt%. MAI was synthesized according to the literature.[7] Indium tin oxide (ITO) on glass substrates were cleaned sequentially with detergent, ethanol and acetone in ultrasonic bath for 15 min, then PEDOT:PSS (Clevios 4083, Heraeus) was spin-coated at 3000 rpm for 50 s, followed by annealing in the N_2-filled glove box. The perovskite $CH_3NH_3PbI_{3-x}Cl_x$ films were prepared from one-step spin-coating and gradually annealed from 60 °C up to 100 ˚C.

Illuminated $CH_3NH_3PbI_{3-x}Cl_x$ thin films (with high density of surface states). The illuminated perovskite samples were prepared by illuminating pristine perovskite films under white halogen lamp (@150 mW cm^{-2}, daylight rendering spectrum) for 40 min in ultra-high vacuum (UHV) condition in order to obtain high density of Pb^0.

Mixed cations and halides perovskite thin films. ITO substrates were firstly treated with UV-Ozone for 4 min and Poly[bis(4-phenyl)(2,4,6-trimethylphenyl)amine] (PTAA, Sigma-Aldrich, 1.5mg/mL in toluene, dissolved over night by stirring) was spin-coated at 6000 rpm for 30 sec after spreading around 20 μL on the substrate prior to starting. The substrate is subsequently annealed at 100°C for 10 minutes and left to cool for 5 minutes. The perovskite solution consisted of 1 mmol PbI_2(Alfa Aesar), 1 mmol MAI (dyesol), 0.85

mmol Dimethyl sulfoxide (DMSO, Sigma Aldrich) and 0.15 mmol Thiourea (Sigma-Aldrich) in 636 µL anhydrous DMF (Alfa-Aesar). The perovskite solution MAFA is prepared by dissolving (stirring overnight) MABr (0.2M, dyesol), FAI (1.03M, dyesol), PbI_2 (1.13M, Alfa-Aesar) and $PbBr_2$ (0.2M TCI) in anhydrous DMF/DMSO = 4:1 (v/v, Alfa-Aesar and Sigma-Aldrich, respectively). In parallel CsI (1.5M, Sigma-Aldrich) and RbI (1.5M Sigma-Aldrich) are dissolved in DMSO and DMF/DMSO(4:1, v/v), respectively. CsMAFA is mixed by combining MAFA:CsI = 960:40 µL/µL to produce a composition with the stoichiometry $Cs_{0.05}[MA_{0.17}FA_{0.83}Pb(I_{0.83}Br_{0.17})_3]_{0.95}$. An aliquot of this mixture is then further mixed CsMAFA:RbI = 960:40 µL/µL to produce RbCsMAFA ($Rb_{0.05}\{Cs_{0.05}[MA_{0.17}FA_{0.83}Pb(I_{0.83}Br_{0.17})_3]_{0.95}\}_{0.95}$). Typically, 30 µL of either perovskite solution is drop-casted on the ITO substrates and spin-coated at 3500prm with 3 seconds acceleration (i.e. 1160 rpm/s) for 35 seconds. 10 seconds after the start of the spin-coating 100 µL of ethyl acetate (Sigma-Aldrich) are dispensed on the spinning substrate inducing a color change to dark brown ($MAPbI_3$) or reddish-brown (mixed perovskites), depending on the composition. The samples are thereafter annealed for 1 hour at 100°C and never exposed to air between any of the measurements.

PbI_2 thin films. PbI_2 film was prepared on ITO substrates by spin-coating the PbI_2 solution in DMF, followed by annealing at 100 °C for 15 min in the glove box.

Perovskite single crystals. The large-sized single crystals in millimeters ($MAPbBr_3$ and $MAPbI_3$) with high crystalline quality, were grown from a saturated solution using a seed-induced nucleation method.[90] The crystals were cleaved with a scalpel in a N_2-filled glove box before photoemission measurements and transferred to the UHV system without air exposure.

Accepter molecules deposition. 1,4,5,8,9,12-hexaazatriphenylenehexacarbonitrile (HATCN) and 2,2-(perfluoronaphthalene-2,6-diylidene) dimalononitrile (F6TCNNQ)

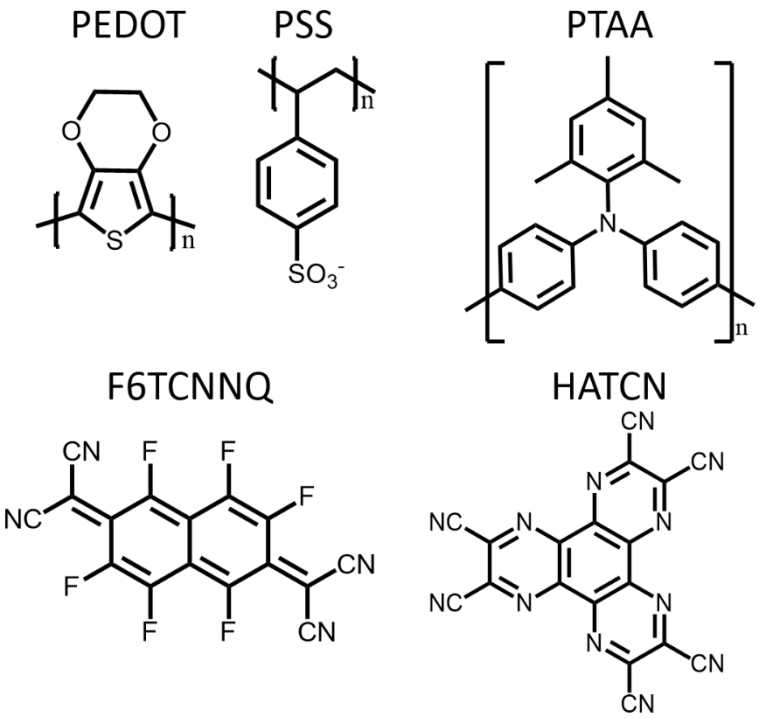

Figure 5.1 *Chemical structures of the materials employed in this thesis. PEDOT:PSS solution was obtained in 1.3 to 1.7 wt.% in water with the PEDOT/PSS ratio of 1/6.*

molecules were purchased from Novaled, with the molecular chemical structure shown in **Figure 5.1**. Both materials were used as received and thermally evaporated from resistively heated quartz crucibles. The nominal deposited thickness was monitored by a quartz crystal microbalance.

PEDOT:PSS and PTAA pre-covered ITO substrate. $CH_3NH_3PbI_{3-x}Cl_x$ thin films were prepared on PEDOT:PSS pre-covered ITO substrates, while the PTAA was used as substrate layer for $MAPbI_3$ and mixed perovskite thin films in order to mimic the actual device architecture. As shown in **Figure 5.2**, the work functions of PEDOT:PSS and PTAA layers are 4.84 eV and 4.52 eV, respectively.

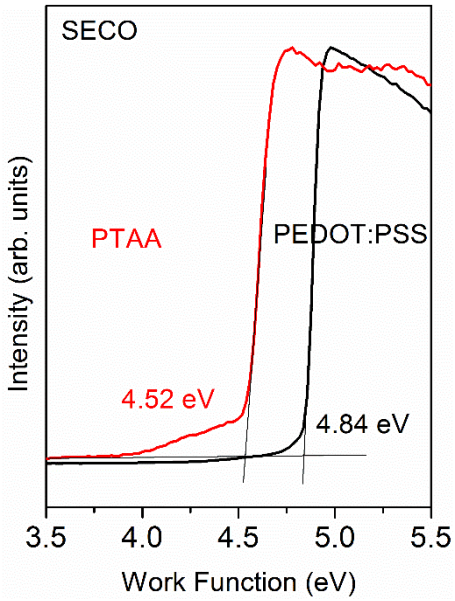

Figure 5.2 *Secondary electron cut-off (SECO) spectra of the PEDOT:PSS (black) and PTAA (red) layers on top of ITO substrates.*

5.2 Experimental setups

Optical properties.

Optical absorption properties can be obtained via UV-vis absorption measurements, where, experimentally, transmitted light is normally measured. The relation with respect to the change of light intensity ΔI can be formulated as

$$\Delta I = I_{abs} + I_{sca} + I_{ref} + I_{int} \qquad 5.1$$

where I_{sca}, I_{ref} and I_{int} represent the fraction of scattered, reflected and interference light, respectively. Those are usually a small contribution to the absorption, and can be neglected.[28]

In general, following the law of Beer-lambert, the intensity of the attenuated light I, when passing through a material at thickness of x, can be written as

$$I = I_0 - \Delta I = I_0 e^{-\alpha x} \qquad 5.2$$

where α is the absorption coefficient of the material and x the propagation path of the incident light.

UV-vis absorption measurements in this work were performed using LAMBDA 750

UV-vis-NIR spectrophotometer from Perkin Elmer. Transmission mode was employed while reflection and scattering are neglected.

Morphological properties.

Atomic force microscope (AFM), often referred as scanning probe microscopy (SPM) is widely used to characterize the surface properties, i.e. the interactions between the tip and sample surface, for instance, van der Waals, electromagnetic force and so on.[18, 121]

The working principle of a AFM is schematically shown in **Figure 5.3**, a sharp tip is brought closely to a sample surface, and interactions between the tip and the sample surface are measured by monitoring the displacement of the free end of the cantilever. The small movement of the lever is normally determined by a laser beam that is reflected off the cantilever and redirected onto the photodetector.

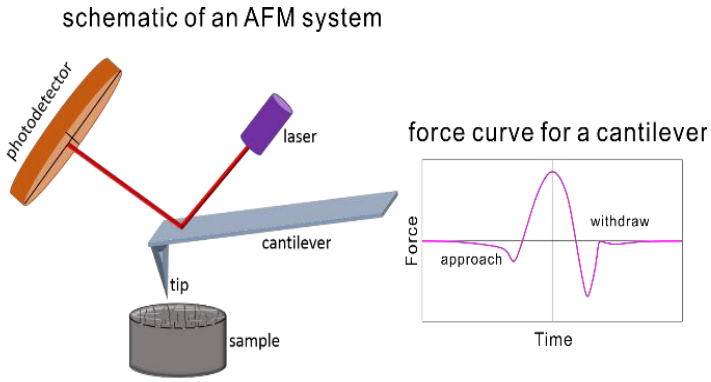

Figure 5.3 *A schematic of an AFM system consisting of a laser source, cantilever and photodetector (left). Force curve as a function of time for the cantilever operated at PeakForce Tapping mode (right).*

AFM measurements in this thesis were performed using PeakForce Tapping mode, similar to Tapping mode where the cantilever is oscillated at or near resonance frequency normal to the sample surface, in contrast, it operates well below the resonance frequency, thus avoiding the dynamics of a resonating system. The measurements were carried out using Bruker Dimension FastScan system. ScanAsyst mode,[1] which is based on PeakForce Tapping mode, is employed for all measurements.

Surface potential measurements by Kelvin probe.

Kelvin probe measurements were conducted using KP Technology (KP6500)

instrument in a N_2 filled glove box. The 2 mm diameter gold tip was calibrated using a highly oriented pyrolytic graphite (HOPG) sample, whose work function was directly measured by photoemission yield spectroscopy (PYS) in air and UPS in UHV condition. Therefore, work function of HOPG in inert atmosphere is estimated to be at 4.66 ± 0.09 eV by averaging the values measured by PYS and UPS. The results of PYS and UPS on HOPG are shown in section 5.3.

Surface potential characterization upon illumination, i.e. surface photovoltage measurement, was carried out where the sample was illuminated from the side with a corrected power intensity at ca. 20 mW/cm^2.

Molecular film thickness

The deposited molecular thickness was determined by using a quartz crystal microbalance (QCM). It is based on a piezoelectric crystal, from which a small amount of mater placed on the crystal surface can be quantified by measuring the change in the resonating frequency, known as Sauerbrey equation.[94]

$$\Delta f = -\frac{2{f_0}^2}{\sqrt{\rho_q u_q}}\frac{\Delta m}{A} \qquad 5.3$$

where f_0 is the resonance frequency, ρ_q the density of quartz (2.648 g/cm^3), u_q the shear modulus of quartz (2.947×10^{11} g/(cm·s^2)), A the effective area. Therefore, from this formula, the thickness of the deposited material can be evaluated from the change of oscillation frequency, given the density of the material. However, it is noted that this is a good approximation for rigid and compact layers, i.e. layer-by-layer growth materials. The determined film thicknesses in this thesis are only considered as nominal thicknesses.

Photoemission and LEED measurements.

LEED experiments were conducted using a micro-channel plate LEED (OCI BDL800IR-MCP). All LEED patterns were corrected from distortion following the procedure described by Mom *et al*.[104]

Most of the photoemission results presented in this thesis were performed at an UHV system (Humboldt-Universität zu Berlin) consisting of sample preparation and analysis chambers (base pressure 1×10^{-9} mbar), as well as a load-lock (base pressure 1×10^{-6} mbar). Spectra were recorded at room temperature and normal emission (unless specified otherwise) using a SPECSPhoibos 100 hemispherical analyzer.[1]

UPS performed at this system was using helium (He) discharge lamp (21.22 eV) with a filter to reduce the photon flux. XPS was recorded using aluminum (Al) Kα radiation (1486.7 eV) generated from a twin anode X-ray source. The full-width at half maximum (FWHM) of the Al Kα source is 0.85 eV.[5] The FWHM of the He source is much smaller and is typically below 10 meV. Therefore, the experimental broadening form the He excitation can be neglected. The overall resolution was set at 130 meV for UPS and 1.2 eV for XPS. The energy resolution of the instrument can be determined from the Fermi edge spectrum of a test metal. As shown in **Figure 5.4**, in the case of UPS measurements using a pass energy of 5 eV, the Fermi edge spectrum of a polycrystalline gold can be well fitted with a convolution of a Fermi function (at 300 K) and a Gaussian function. The instrument

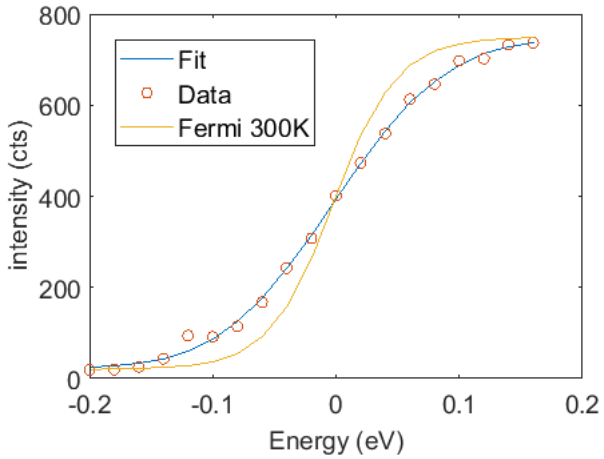

Figure 5.4 *UPS spectrum around E_F of a polycrystalline gold sample at 300 K. The instrumental resolution is determined by convoluting a Fermi function (T = 300 K, yellow line) with a Gaussian function of FWHM at 130 meV.*

resolution is then given by the FWHM of the Gaussian function, which is 130 meV. The same procedure can be applied to XPS spectrum in order to evaluate the experimental

resolution. The secondary electron cut-off (SECO) measurements were conducted while the sample was negatively biased at 10 V.

High resolution XPS experiments were carried out using a monochromated Al Kα source and a SPECSPhoibos 150 hemispherical analyzer (FUNSOM, Soochow University).

The angle-resolved photoelectron spectroscopy experiments was conducted at an UHV system (FUNSOM, Soochow University), which is equipped with SPECSPhoibos 150 hemispherical analyzer[1] and SPECS UV300[1] excitation source. The Phoibos 150 analyzer comprising with a 2D-CCD detector (1376 × 1040 pixels) allows us to determine kinetic energy as well as the emission angle of the photoelectrons simultaneously without changing the polar angle. In combination with the plane-grating monochromator SPECS TMM 302 for the UV excitation, high resolution measurements can be completed. Angular acceptance of up to ± 12 degree can be acquired simultaneously.

Photoelectron energy and acceptance angle were calibrated using a clean Au (111) single crystal. As shown in **Figure 5.6** for the dispersion of the Au (111) surface states, the crossing of the Fermi level at ± 4.65 ± 0.1°, which corresponds to momentum at ± 0.20 $Å^{-1}$, agrees well with the expected value at ± 4.55 ± 0.1°.[120]

5.3 Data analysis

Sample work function from Kelvin probe measurements is determined from the following equation:

$$\Phi_{sample} = CPD + \Phi_{tip} \qquad 5.4$$

where the Φ_{tip} is calibrated using a highly ordered pyrolytic graphite (HOPG) sample. Φ_{HOPG} of 4.57 eV and 4.76 eV for the HOPG sample are directly determined from UPS in UHV and PYS in air, respectively, as shown in **Figure 5.5**. As a result, a Φ_{HOPG} of 4.66 ±

0.09 eV in inert atmosphere is estimated by taking the averaged values.

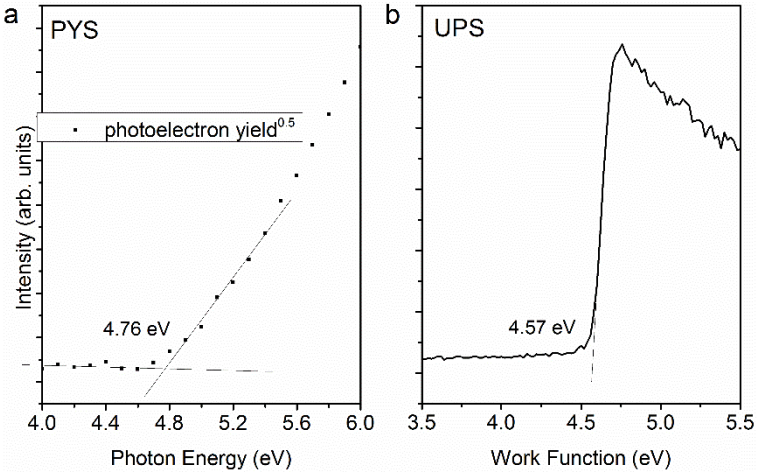

Figure 5.5 *HOPG work function measurements by (a) PYS in air and (b) UPS in UHV condition.*

Angle-integrated UPS spectra were corrected by subtracting the satellite contributions from He I_β (23.09 eV, ~ 2-3%) and He I_γ (23.74 eV, ~ 0.8%).

ARPES data were processed following the below steps:

1. The amplified photoelectron image can sometimes have constant light intensity due to aging of the photodetector system, therefore, these constant intensity or hot pixels were replaced by averaging the neighbor data points.

2. Normalization was applied to the energy distribution curves (EDCs) of the ARPES data.

3. To improve the contrast and visualization of the band dispersions, the 2D curvature

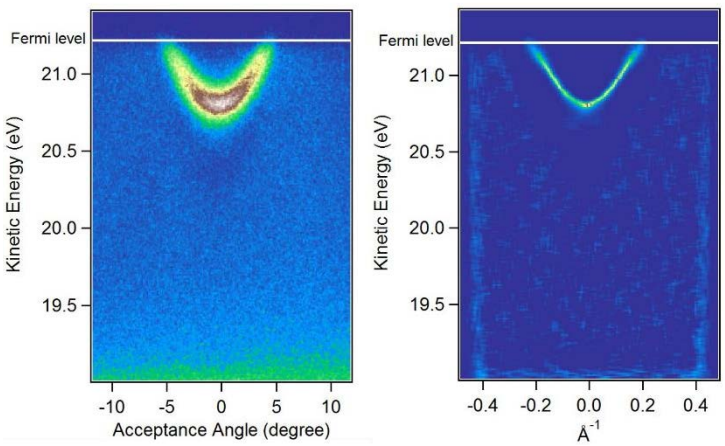

Figure 5.6 *ARPES mapping of the dispersion of the Au (111) surface states. (left) Raw dispersion spectra of the surface states, (right) 2D curvature method processed dispersion of the surface states.*

method[173] was applied to the ARPES data. One example can be found in **Figure 5.6**. for the dispersion of Au (111) surface states. It can be clearly seen that the 2D curvature processed spectra present much improved localization of the band extrema and reduced peak broadness while maintaining the peak positions.

6 Results and discussion

As briefly mentioned in the introduction, this chapter will first start with a characterization of halide perovskites in section 6.1. Then a detailed investigation on the band dispersion on two prototypical perovskite single crystals is laid out in section 6.2. With these benchmark data, in section 6.3, the global VB maxima are identified and the challenges of determining the VBM or VB onset with high reliability are resolved. The results of section 6.2 and 6.3 are mainly based on our published work in reference [185]. Turning our focus on the electronic properties of polycrystalline thin films, section 6.4 will elucidate the origin of the n-type behavior observed on perovskite surface and demonstrate the effect of SPV in characterizing halide perovskites by photoemission. The results shown in 6.4 were published in [184]. The following section of 6.5 will go one step further and explore the impact of surface state density on the energy level alignment at halide perovskite/electron acceptor interfaces. This section is based on our published results in [186].

6.1 Characterization of halide perovskites

Surface morphology

The physicochemical properties of HaPs are inherently related to the surface morphology,[35, 54, 123, 160] as it has been extensively demonstrated to be crucial for charge dissociation efficiency,[54] device stability and the resulting solar cell

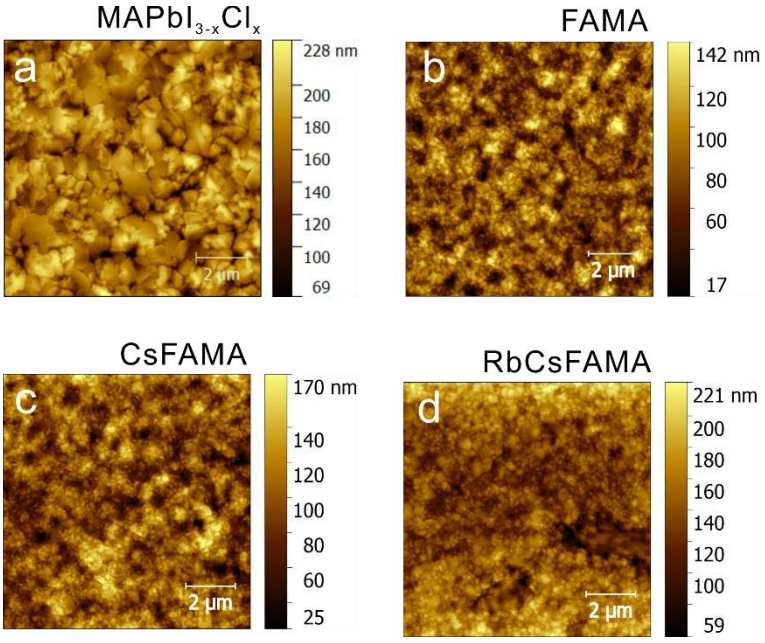

Figure 6.1 *AFM surface morphology of (a) $MAPbI_{3-x}Cl_x$ (b) FAMA (c) CsFAMA (d) RbCsFAMA perovskite surfaces. (a) is adapted from [184]*

performances.[35, 123, 160] Particularly, the inhomogeneous nature of the films is one of the practical issues in device fabrication. Therefore, extensive efforts have been devoted to this field in order to obtain high surface coverage and high quality films, as we discussed in section 3.4. In this section, we will first examine and discuss the basic morphological and crystal structure of the perovskite films, because it will provide a solid platform to conduct detailed investigations on the optoelectronic properties.

The typical surface morphology of the perovskite films is presented in **Figure 6.1**, for different perovskite compositions. Clearly, rather homogeneous and compact grains with high surface coverage can be achieved for $MAPbI_{3-x}Cl_x$ using the one-step spin-coating method. Also, the individual crystallites are well defined and exhibit rather large grain size up to 2 µm. In contrast, the AFM images for mixed cations and halides perovskites exhibit globally similar surface morphology with rather small grain sizes (within the range of ca. 100 nm). Adding of small amount of cations (Cs and/or Rb) does not seem to have large

impact on the surface morphology of FAMA perovskites.

Crystal structures

$MAPbI_{3-x}Cl_x$ films, as the prototype of the hybrid perovskites, are further studied by means of X-ray diffraction, as shown in **Figure 6.2** (a). The XRD pattern plotted in linear intensity scale reveals highly oriented crystallites, preferentially along [110] direction. This agrees well with the large crystallites observed in AFM images [**Figure 6.1** (a)] and has been widely reported in the community.[33, 176]

Powder XRD crystallographic analysis on $MAPbI_3$ single crystals in **Figure 6.2** (b)

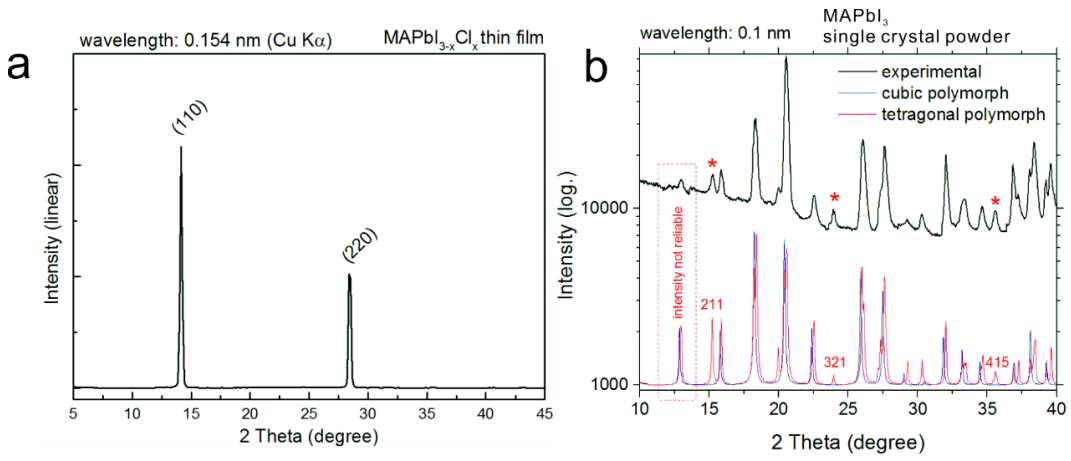

Figure 6.2 *X-ray diffraction pattern of (a) a $MAPbI_{3-x}Cl_x$ film on ITO/PEDOT:PSS substrate and (b) $MAPbI_3$ single crystal powders at room temperature. Figures are adapted from [184].*

shows that the crystal structure, as expected, exhibits the tetragonal phase at room temperature, which can be identified from tetragonal diffraction peaks at (211), (321) and (415). Furthermore, lattice parameters of the unit cell are evaluated as $a = b = 8.85$ Å and $c = 12.64$ Å, similar to those reported in the literature.[90]

6.2 Band structure of halide perovskite single crystals

In contrast to their success as the active materials in the optoelectronic devices, fundamental optoelectronic properties of HaPs are still not fully addressed and understood.

In particular, the electronic band structure is the key for unraveling the intrinsic charge transport properties of a semiconductor, as the effective mass can be directly accessed from it.[134] In the following section, the surface lattice and the electronic band structure will be studied by combining LEED and ARPES measurements, complemented by DFT calculations.

6.2.1 LEED studies of halide perovskite single crystals

1) LEED studies of $MAPbBr_3$ single crystal surface

The first bulk and surface Brillouin zone of a simple cubic lattice is displayed in **Figure 6.3** (a). The LEED pattern of the $MAPbBr_3$ single crystal at RT in **Figure 6.3** (b), exhibits a square diffraction spots, which corresponds to the (001) surface of a cubic lattice. The lattice parameters can be estimated from the LEED pattern, and are here determined to be $a_{LEED} = b_{LEED} = 5.72 \pm 0.10$ Å, in good agreement with the lattice constants of the cubic structure ($a = b = c = 5.90$ Å, space group P*m*-3*m*) from X-ray diffraction.[90] As expected, when lowing the temperature to 200 K, the crystal undergoes structural transition towards the β phase of the tetragonal structure ($a = b = 8.32$ Å, $c = 11.83$ Å, space group I4/mcm).[117] This is observed in **Figure 6.3** (c), where additional diffraction spots form a smaller square lattice rotated by 45° with respect to that of the cubic lattice at RT. The lattice constants estimated from the low temperature LEED pattern amounts to 8.37 ± 0.10 Å, which corresponds well to that of the β phase of the tetragonal structure, as discussed in section 3.1. It is noted that the first order diffraction spots (0, 1) of the cubic lattice (1.064 $Å^{-1}$) coincides with that of the (1,1) diffraction spots of the tetragonal lattice (1.067 $Å^{-1}$), as

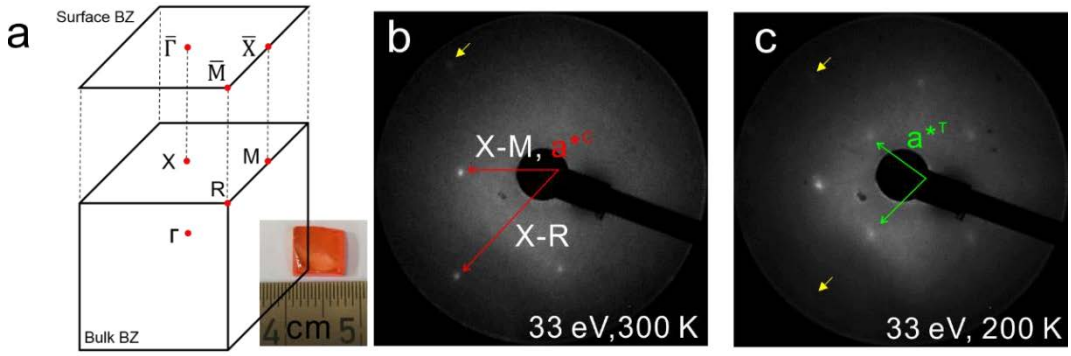

***Figure 6.3 Single crystal surface structure**. (a) The first bulk Brillouin zone (BZ) and surface Brillouin zone (SBZ) of a cubic lattice. LEED pattern of the (001) plane of a $MAPbBr_3$ single crystal at an electron energy of 33 eV at (b) 300 K and (c) 200 K. The reciprocal lattice parameter a^{*C} refers to the cubic phase, and a^{*T} to the tetragonal phase. Yellow arrows in (b) and (c) indicate the position of weak intensity diffraction spots. The inset in (a) shows a photograph of one of the $MAPbBr_3$ single crystals. Figures are taken from [185]*

a consequence, it is difficult to conclude whether the transition is complete or if both phases coexist on the sample surface.

2) LEED studies of $MAPbI_3$ single crystal surface

X-ray diffraction measurements of $MAPbI_3$ crystals reveal that it retains a tetragonal structure at RT. However, reports have shown that $MAPbI_3$ features the coexistence of tetragonal and cubic phases already at RT, as deduced from transmission electron microscopy.[73] A different investigation, employing X-ray diffraction, also concluded that already starting from 300 K, $MAPbI_3$ exhibits phase transitions over a wide range of temperature.[157] Similar observations are made in our work, as deduced from the LEED patterns taken at two different incident electron energies for a cleaved $MAPbI_3$ single crystal, shown in **Figure 6.4**. The obtained LEED patterns exhibit a square pattern, which demonstrates that cleavage of the sample results in the (001) surface being exposed. Remarkably, the LEED pattern shown in **Figure 6.4** (a) is composed of bright and dim spots at an electron energy of 21 eV, whereas the dim spots are markedly vanished in the LEED pattern taken with 33 eV primary energy, as shown in **Figure 6.4** (b). After distortion correction, the lattice parameter determined from the dim spots observed in **Figure 6.4** (a)

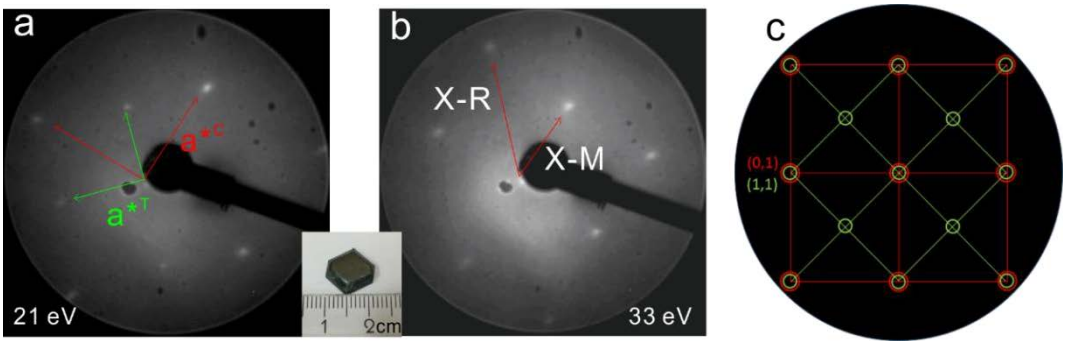

Figure 6.4 *LEED patterns of the (001) plane of a $MAPbI_3$ single crystal at 300 K at an electron energy of (a) 21 eV and (b) 33 eV. The reciprocal lattice parameter a^{*C} refers to the cubic phase, and a^{*T} to the tetragonal phase. ARPES measurements were performed along the X-M and X-R directions [highlighted with red lines in (b)]. The inset shows a photograph of a $MAPbI_3$ single crystal. (c) Schematic representation of a LEED pattern obtained for co-existing cubic and tetragonal surface structures (red: cubic, green tetragonal). Figures are taken from [185].*

amounts to $a^T = 7.96 \pm 0.16$ Å, which corresponds within 10% to the lattice parameter of the (001) surface of the tetragonal phase (8.87 Å), as determined by X-ray diffraction.[90]

Regarding the LEED patterns for $MAPbI_3$, we remark that the ratio between the lattice parameter of the tetragonal and cubic phases is such that coexisting phases, with lattice orientation rotated by 45° with respect to each other, as observed for $MAPbBr_3$, would provide a diffraction pattern as displayed in **Figure 6.4** (c), i.e., with the diffraction pattern of the tetragonal phase in coincidence with a c(2x2) superimposed structure with respect to the cubic phase diffraction pattern. Considering the LEED pattern in **Figure 6.4** (b), the determined lattice parameter amounts to $a^C = 6.02 \pm 0.11$ Å, which is in satisfactory agreement with the known lattice parameter of the pseudo-cubic phase (6.30 Å). Therefore, one may attribute the square pattern in **Figure 6.4** (b) to the (001) plane of the cubic phase, whose presence, as discussed in the following, is unambiguously confirmed by ARPES measurements.

6.2.2 ARPES studies of halide perovskite single crystals

1) ARPES studies of $MAPbBr_3$ single crystals

Figure 6.5 (a) and (d) show the as-obtained ARPES spectra of the VB for $MAPbBr_3$ crystal, as a function of $k_{//}$ along the high symmetry directions determined by LEED. Here, $k_{//}$ is the electron wave vector component parallel to the sample surface, determined according to the relation 4.14 as discussed in section 4.3.3:[60]

$$\hbar k_{//} = \sqrt{2m_0 E_{kin}} \times sin\theta; \qquad 6.1$$

where E_{kin} is the measured kinetic energy of the photoelectrons and θ the electron emission angle with respect to the surface normal. Because the wave vector perpendicular to the surface is not conserved in ARPES measurements, and the integration in $k_{\perp}$ highly depends on the ration between the electron mean free path and the lattice constant, the measured band structure can be interpreted as between the bulk band structure regime and projected one-dimensional DOS.[139] In the latter case, where the IMFP is much smaller than the lattice constant, the measurement directions can be assigned to $\bar{\Gamma}$-$\bar{M}$ and $\bar{\Gamma}$-$\bar{X}$ of the surface BZ, as presented in **Figure 6.3** (a) for the surface BZ. Therefore, DFT calculated bands are used in order assign accurately the probed directions.

DFT calculated valence bands are presented in **Figure 6.6**, and are used to assign the probed directions more accurately. We can clearly see that highly dispersive bands, in particular for the top valence bands, are observed with the band width of 1.5 eV for *X*-*R* and 0.8 eV for *X*-*M* directions. In addition, the VBM is found at *R* point for the cubic structure of $MAPbBr_3$, in agreement with the observations in the theory.[114, 162] We further find that the calculated bands along the *X*-*M* and *X*-*R* momentum directions match well with the ARPES spectra, especially for the strongly dispersive top valence bands, as shown in **Figure 6.5**. As a comparison, strong discrepancies are observed between the experimental spectra and the theoretical calculated bands along *Γ*-*X* and *Γ*-*M* directions.

To improve the visualization of the bands, the ARPES spectra were analyzed using the 2D curvature method,[173] displayed in **Figure 6.5** (b) and (e). These treated ARPES data

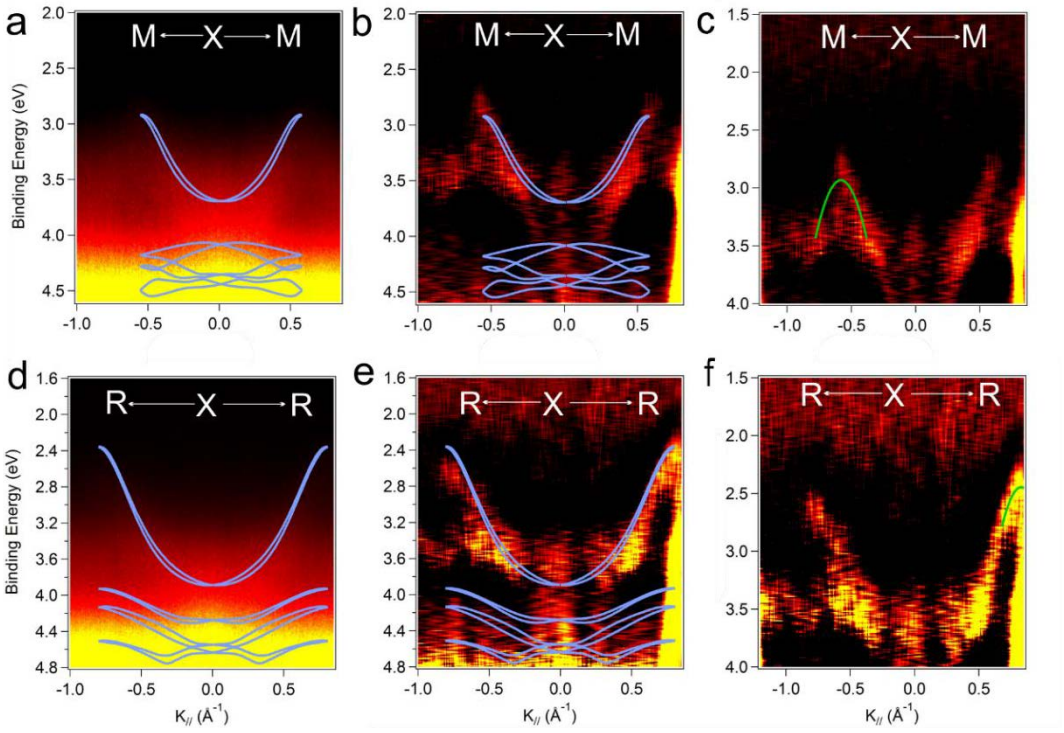

Figure 6.5 *ARPES k-space maps of the $MAPbBr_3$ single crystals along the (a) X-M and (d) X-R high symmetry momentum directions. (b) and (e) are the corresponding 2D curvature band maps. 2D curvature band maps near the VBM, along the (c) X-M and (f) X-R directions, fitted with parabolic curves (lines in green color) near the band extreme. DFT calculated bands, shown in light blue lines are shifted in energy and superimposed onto the ARPES maps for comparison. The bandwidths determined from the 2D curvature are ~0.7 eV and ~1.3 eV along the X-M and X-R directions, respectively. Hole effective masses from the parabolic fit are evaluated to be ~0.30 ± 0.15 m_0 for the X-M and ~0.25 ± 0.05 m_0 for the X-R momentum directions. The binding energy is referenced to the Fermi level (E_F), with E_F = 0 eV. Figures are adapted from [185].*

appear much sharper, which help track the *k*-dependent peak positions and provide a more straightforward comparison with the DFT-calculated band structure. These spectra clearly show that the VBM occurs at the *R* point (i.e., BZ edge) and the bandwidth amounts to 1.3 eV and 0.7 eV along the *X-R* and *X-M* directions, respectively, also in very good agreement with the calculated bandwidths. Therefore, we provide experimental evidence of valence bands dispersion in good agreement with the theoretically predicted bands. Furthermore, the ARPES spectra along *X-M* direction allow us to determine the lattice constants, which give rise to $a_{ARPES} = 5.56 \pm 0.29$ Å, in agreement with the LEED analysis of the cubic phase

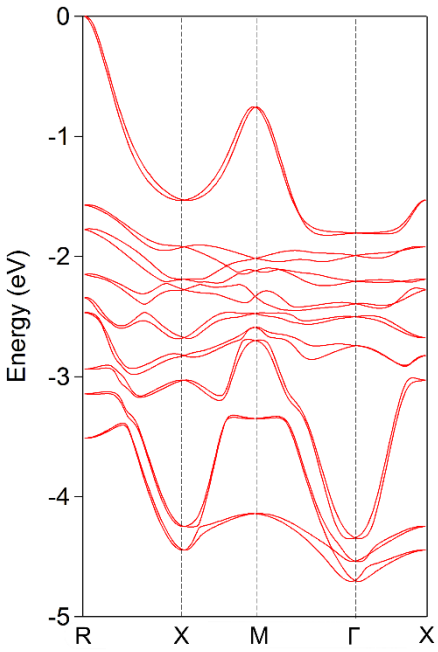

Figure 6.6 *DFT calculated valence band structure of $MAPbBr_3$ at cubic phase. Valence band maximum (VBM) is shifted at 0 eV. The calculated band structure along X-M and X-R directions corresponds well with the ARPES results, with the calculated bandwidth of 1.5 eV for X-R direction and 0.8 eV for X-M direction. In comparison, Γ-M and Γ-X directions show the bandwidth of 0.8 eV and 0.3 eV, respectively, which exhibit large discrepancy with ARPES determined values. Figure is taken from [185].*

structure. One key quantity to understand charge transport properties of the halide HaPs semiconductors is the hole effective mass, which we determine here to be 0.30 ± 0.15 m_0 for the *X-M* direction and 0.25 ± 0.08 m_0 for the *X-R* direction by applying a parabolic fit to the VBM, as illustrated in the magnified valence band region in **Figure 6.5** (c) and (f), respectively.

2) ARPES studies of $MAPbI_3$ single crystals

The as-obtained ARPES spectra of $MAPbI_3$ single crystal are shown in **Figure 6.7** (a) and (d), together with the 2D curvature processed spectra shown in **Figure 6.7** (b) and (e). It can be clearly seen that the as-measured ARPES spectra exhibit sharp dispersive bands, especially for the top valence bands. To locate along which momentum direction the measurements were performed, the DFT calculated bands, as shown along *X-M*, *X-R*, *Γ-M* and *Γ-X* high symmetric directions in **Figure 6.8**, are systematically compared to the experimental results. We found that the calculated bands along *X-M* and *X-R* directions agree overall very well with the ARPES spectra. In contrast, the comparison between

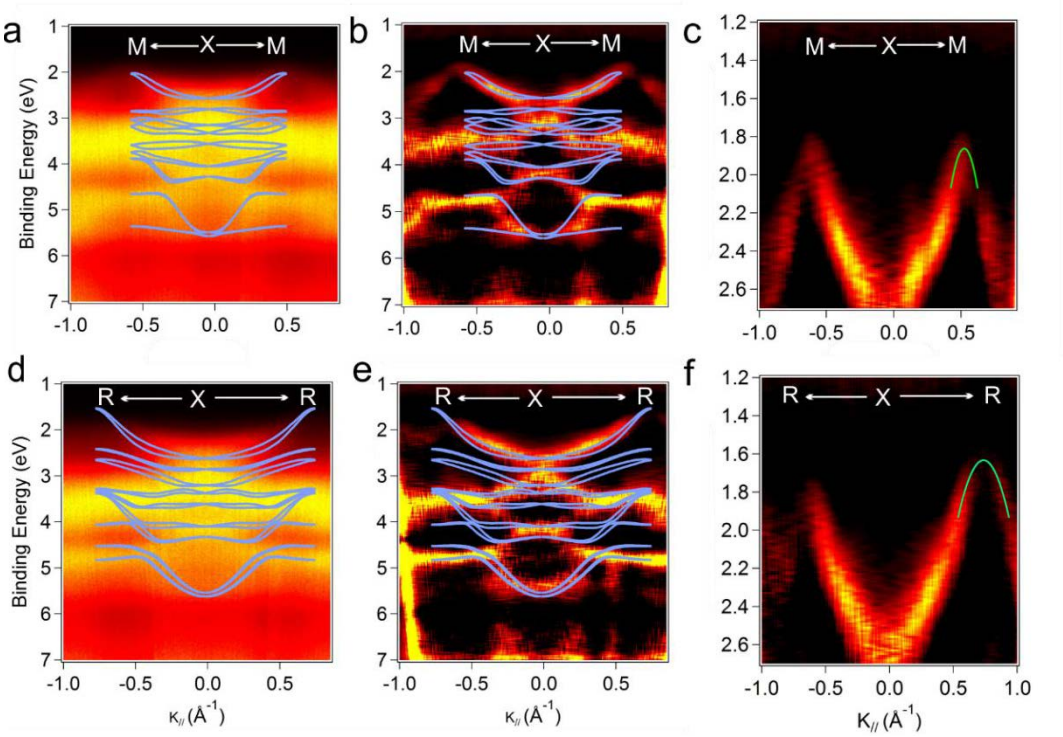

Figure 6.7 *ARPES k-space maps of a $MAPbI_3$ single crystal along the (a) X-M and (d) X-R high symmetry momentum directions. (b) and (e) are corresponding 2D curvature band maps. 2D curvature band maps near the VBM, along the (c) X-M and (f) X-R directions fitted with parabolic curves (line in green color) near the band extreme. DFT calculated bands, shown in light blue lines, are shifted in energy and superimposed onto the band maps for comparison. The bandwidths determined from the 2D curvature are ~0.6 eV and ~1.0 eV along the X-M and X-R directions, respectively. Hole effective masses from the parabolic fit are evaluated to be ~0.18 ± 0.06 m_0 and ~0.50 ± 0.10 m_0 for X-M and X-R directions, respectively. Figure are taken from [185].*

experiments and theory exhibits large difference in bandwidth along *Γ-M* and *Γ-X* directions. Minor differences can still be noted that some calculated bands are seemingly missing from experimental data. This can be possibly ascribed to the matrix element effects given the polarization of the excitation light, from which the photoelectron yield can be possibly modified.[107] We further observe in the 2D curvature spectra that the top VB exhibits large bandwidth, which amounts to 0.6 eV for *X-M* and 1.0 eV for *X-R* directions, in excellent agreement with that of the calculated bands (0.6 eV and 1.1 eV for *X-M* and *X-R*, respectively). Moreover, it can be seen that the VBM is found at *R* point, which is consistent with the theoretical calculations of the band structures at cubic phase.[14]

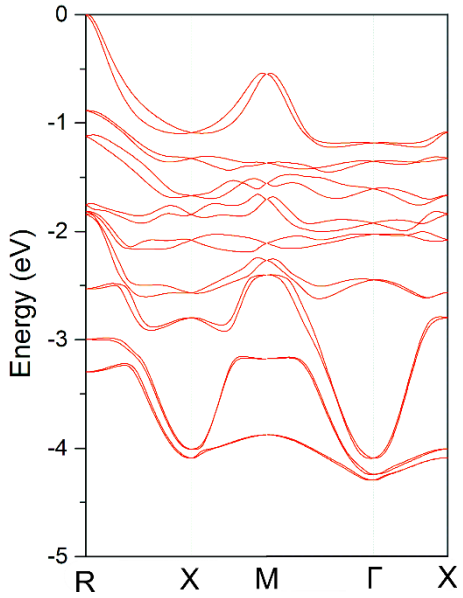

Figure 6.8 *DFT calculated valence band structure of $MAPbI_3$ at cubic phase. VBM is shifted at 0 eV. Again, the bandwidth of X-M and X-R directions corresponds well with the ARPES determined values, with the calculated bandwidth of 1.1 eV for X-R direction and 0.6 eV for X-M direction. As a comparison, the bandwidth of Γ-M and Γ-X directions only exhibits 0.6 eV and 0.1 eV, respectively. Figure is taken from [185].*

It is also noted that the tetragonal phase, though visible at low intensity in LEED pattern, is missing from ARPES spectra. This can be understood from the fact that the lack of tetragonal band structures in ARPES is consistent with the predominant intensity of the diffraction spots from cubic phase, as the final states in photoemission corresponds to the time-reversed LEED states within one-step theory of photoemission process.[143] Besides, slight temperature increase on the sample surface by incident UV light cannot be excluded. Such effect might already induce surface phase transition and account for the cubic band structure being only observed in the ARPES spectra.

Parabolic fitting has also been applied to fit the top VB bands in order to evaluate the hole effective mass for $MAPbI_3$, as presented in **Figure 6.7** (c) and (f). This yielded rather small hole effective masses of 0.18 ± 0.06 m_0 for *X-M* and 0.50 ± 0.10 m_0 for *X-R* momentum directions by applying parabolic fitting to the very top valence bands.

3) Discussion of the fundamental charge transport mechanism of HaPs

At this stage, it will be desirable to discuss the mechanism that governs the charge transport in HaPs. Knowing the effective masses from ARPES data, based on similar values of m_h*, a theoretical approach[49] based on Kane model has estimated the hole mobility for the pseudocubic $MAPbI_3$ to be 800-1500 $cm^2/V{\cdot}s$, which, in contrast, are 1-2 orders of magnitude higher than these experimental values,[54] as summarized in section 3.3.

Different models have been proposed to explain such discrepancy between the small effective mass and the low mobility.[69, 130, 171, 181, 183]

Electron-phonon interaction model using scattering theories was firstly applied to explain such phenomenon.[69] Within this model, which approximates the electron-phonon interactions from the change in the electronic structure induced by the optical phonons, the temperature-dependent factor of the mobility[124] can be well predicted, however, the RT mobilities are much higher than the experimental values. In comparison, large polaron model,[183] which is based on the Fröhlich interaction,[38] can yield right order of magnitude for the RT mobility, but it contradicts with the experimental determined temperature-dependent factor of the mobility.[124] So far, identifying which scattering mechanisms govern the charge transport process is still an open question.

6.2.3 **Summary**

By combining LEED and ARPES measurements, the electronic band structure of $MAPbBr_3$ and $MAPbI_3$ single crystals with cubic structure surface along high symmetry directions was demonstrated. The two methods, applied to $MAPbBr_3$, consistently reveal that the (001) surface of the cubic phase was exposed upon crystal cleaving. The results obtained for the $MAPbI_3$ surface, however, demonstrate the coexistence of cubic and tetragonal phases already at RT. Only the former, which dominates the LEED pattern, is also observed in ARPES. The ARPES spectra exhibit strongly dispersive features along the *X*-*M* and *X*-*R* directions at 300 K, with a bandwidth of 1.3 eV and 1.0 eV along the *X*-*R* direction for $MAPbBr_3$ and $MAPbI_3$, respectively. The experimentally determined lowest hole effective masses, ~0.25 m_0 for $MAPbBr_3$ and ~0.18 m_0 for $MAPbI_3$ crystals, match the theoretical values calculated by DFT well. This suggests that ARPES measurements on halide perovskites probe bare-particle like excitations, and not fully or partially dressed particles such as (large) polarons. Additionally, the *global* valence band maxima at *R* point for both prototypical perovskites is identified.

6.3 Determining the valence band onset of halide perovskites

While the fundamental electronic band structure, and the evaluated hole effective mass discussed above could help contribute to a better understanding towards the charge transport properties of the HaPs, it is also very important to address the issue of choosing an appropriate method for evaluating the VB onset from PES measurements, as it could lead to inaccurate interpretation of the electronic property of HaPs materials. In this section, we aim at clarifying which method should be applied and at providing solid ground for the use of that method as explained in the following.

The conventional method for VB onset determination, as usually applied in inorganic and organic materials,[80, 99, 125, 145] consists of plotting the EDCs on a linear intensity scale. In contrast, for HaPs materials it was proposed that using a logarithmic extrapolation could lead to a more accurate VB onset determination. Due to the relatively low DOS in the top VB region (i.e. at the *R* point) as a consequence of large dispersive valence bands, the linear extrapolation method could overlook the onset and overestimate the VBM.[34] However, the very low DOS at top VB contradict with the fact that the HaPs typically exhibit very sharp optical absorption edge.[22] As it was argued that the low DOS at top valence bands is a consequence of large dispersion of the VBM from a DFT calculation, at this point, this could be directly compared and addressed from our experimental determined *k*-mapped band structure for the case of $MAPbI_3$.

In the following sections, we will demonstrate and discuss the fundamental differences in determining the VB onset between linear and semi-logarithmic plots, as exemplified mainly based on $MAPbI_3$ data.

6.3.1 Linear vs logarithmic plot for valence band onset

To clearly demonstrate the differences in evaluating the VB onset between linear and logarithmic plot methods, a simulated Gaussian peak with a FWHM of 200 meV, which represents the typical resolution in photoemission spectroscopy, is displayed in **Figure 6.9**. It can be seen that, by taking the intersection point between the background and the tangent line of the top VB DOS, the linear plot can indeed overlook some low DOS below the intersection point (marked in shaded green color), which could lead to an overestimate VB onset. In contrast, those DOS, which result from top valence bands, are taken into account using semi-log plot. However, we further note that, as illustrated in **Figure 6.9** (b), the background level or baseline is very much dependent on instrument (background intensity and the dynamic range of electron analyzer) and the presence and the abundance of gap-

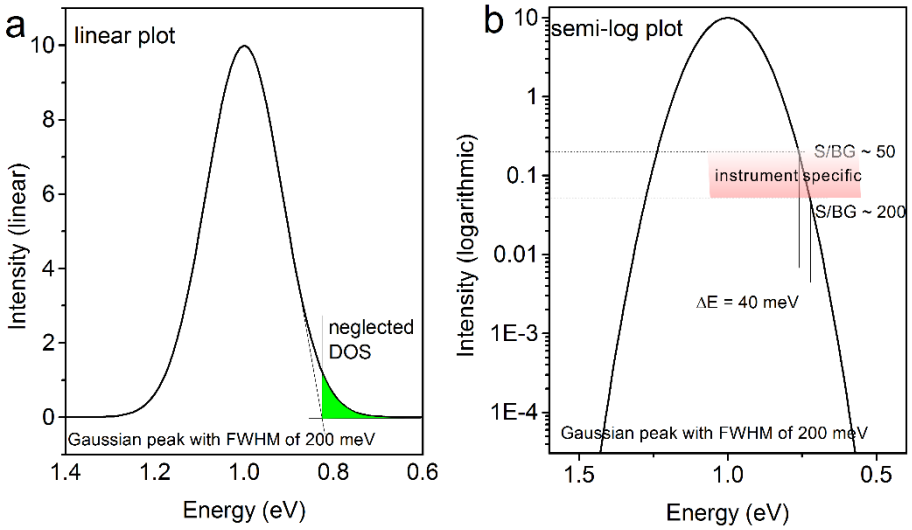

Figure 6.9 *A simulated Gaussian peak with a full-width at half maximum (FWHM) of 200 meV is plotted in (a) linear and (b) logarithmic intensity scale. Signal-to-background ratio is gives as S/G. Figures are taken from [185].*

states.[140] As a result, this can lead to slight variations in evaluating onsets between different experimental setups using semi-log plot. In addition, satellite contribution, if exists, from Helium I_β and I_γ cannot be completely corrected for which further reduces the accuracy in determining the VB onset using semi-log plot method.

To further evaluate the effect of experimental broadening in determining the VB onset for real HaPs VB spectra, the angle-integrated $MAPbI_3$ valence band spectrum is further broadened by 200 meV in FWHM with a Gaussian function. One can immediately see that such broadening gives rise to almost identical valence band spectra on linear intensity scale. However, the VB onset BE is underestimated by 50 meV using the semi-log intensity plot.

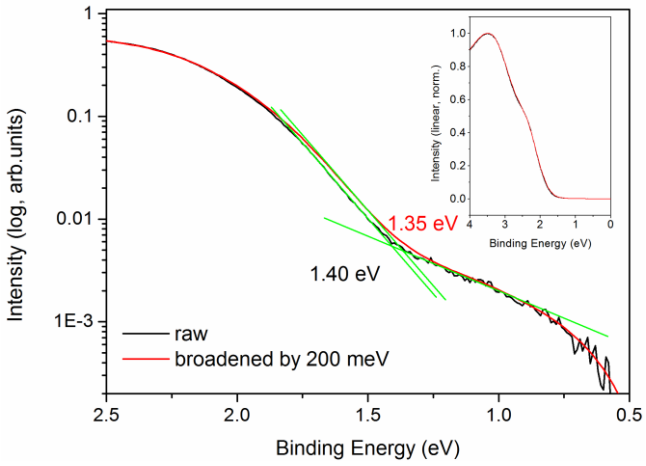

Figure 6.10 *Effect of experimental broadening on the accuracy of using logarithmic plots in determining the VB onset. Inset: the same broadening applied in a linear plot. Figure is taken from [185].*

This indicates an intrinsic resolution of ca. 50 meV by applying logarithmic intensity plots for estimating VB onset, given the typical experimental broadening by 200 meV.

6.3.2 **Valence band onset determination for halide perovskite systems**

Based on the detailed knowledge on the fundamental difference between linear and logarithmic extrapolation methods, and knowing the band structure of the two HaPs in *k*-space, we can unambiguously understand the electronic structure of the polycrystalline films and resolve the issue of reliable valence band onsets determination for HaPs films. This is firstly exemplified by the $MAPbI_3$ results, from which we can pinpoint the VB onset in the BZ using linear and semi-log plots. **Figure 6.11** (a) and (b) present the EDCs at selected *k*-values in the top VB region for *X*-*M* and *X*-*R* directions, respectively. It can be clearly seen that the linear plot extrapolated VB onsets are strongly dependent on the position in the BZ, which essentially follow the top valence band dispersion, with the VB

onset located at 1.41 eV at BZ edge. This indeed agrees with the VBM *k*-location, which is expected at the *R* point. The corresponding logarithmic intensity plots for the selected $k_{//}$-cut EDCs are displayed in **Figure 8.1** (a) and (b) for *X*-*M* and *X*-*R* directions, respectively. A direct comparison of the VB onsets using the two above-mentioned methods at varied $k_{//}$ values is presented in **Figure 6.11** (c). It is noted that the *k*-dependent VB onsets evaluated from linear plot clearly exhibit a very similar dispersion curve as that shown above in **Figure 6.7** for the top VB dispersion. In contrast, the *k*-dependent VB onsets extrapolated from semi-log plot are typically weakly dispersive and therefore cannot reproduce the dispersion curve near the BZ center. In addition to show only little variation with $k_{//}$ on the log-scale, the VB onset is also found at R with 1.30 eV BE. Therefore, the lowest binding

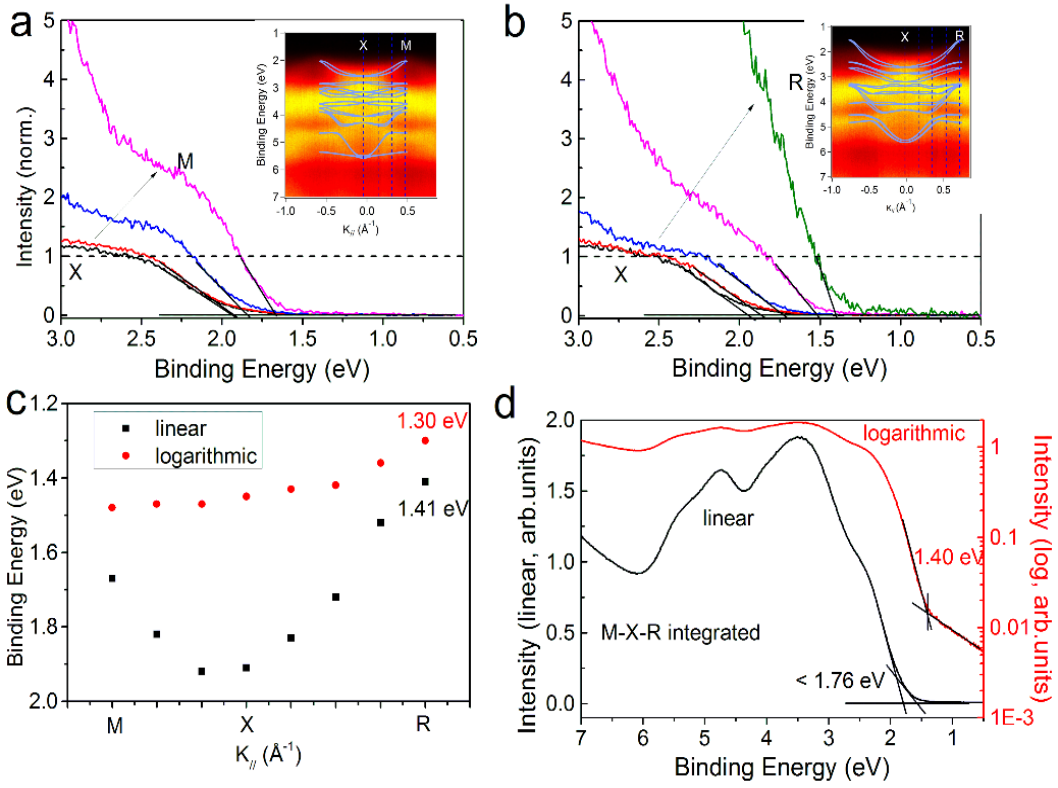

Figure 6.11 *Energy distribution curves (EDCs) at varied k-values along (a) X-M and (b) X-R directions, respectively. The corresponding k for taking the EDCs are shown in the corresponding ARPES k-space maps [insets in (a) and (b)]. (c) K-dependent valence band onsets evaluated using linear and logarithmic extrapolation methods along M-X-R direction. (d) Integrated DOS spectra in linear and logarithmic scale over the full surface BZ. EDCs in (a) and (b) are normalized to the corresponding top valence band peaks in order to better illustrate the k-dependence of the valence band onsets. Figures are taken from [185].*

energy VB onset is expected in the range of 1.30 eV – 1.41 eV, where indeed the global VBM is located (see **Figure 6.8** of calculated bands), depending on determination procedure. Possibly, the nearly-absent $k_{//}$-dependence of the onset determined on logarithmic scale is due to very low photoemission intensity originating from surface patches in the tetragonal phase, whose global VBM is expected at the BZ center. Additionally, this low intensity aside from *R* may arise from the photoelectrons originating from *R* and being scattered by adsorbates at the surface. Such phenomenon has been previously ascribed to final-state diffraction effects in photoemission experiments.[8, 45] Nevertheless, as expected, the semi-log determined VB onsets are overall smaller than that obtained by the linear extrapolation method.

In order to obtain a VB EDCs comparable to that of a polycrystalline $MAPbI_3$ film, the single crystal EDCs integrated over the two main directions of the BZ are shown in **Figure 6.11** (d). It can be clearly seen that the VB onset evaluated from the "artificial" polycrystalline VB spectra by means of linear extrapolation can be as large as ca. 1.8 eV. It is furthermore relatively subjective without a detailed knowledge of the top VB structure and can lead to overestimated VB onset. As a comparison, semi-log plot results in an onset at 1.40 eV, which is readily more comparable to the global VBM identified by ARPES spectrum taken at *R* [Figure 6.7 (e)].

Fully analogous data analysis for $MAPbBr_3$ are shown in **Figure 6.12**. Similar to the observation from $MAPbI_3$ results, the onsets extrapolated using linear intensity plot show some $k_{//}$-dependence, representing the similar dispersion curve in **Figure 6.5**. In contrast, log-scale determined VB onsets in **Figure 8.2** exhibit approximately constant values, as summarized in **Figure 6.12** (c), demonstrating essentially the same observation made for $MAPbI_3$ data. Angle-integrated DOS along the two high symmetry directions of the BZ of $MAPbBr_3$, as shown in **Figure 6.12** (d), demonstrate essentially the same features as

observed for $MAPbI_3$, with the semi-log determined VB onset being more closer to the *R* point.

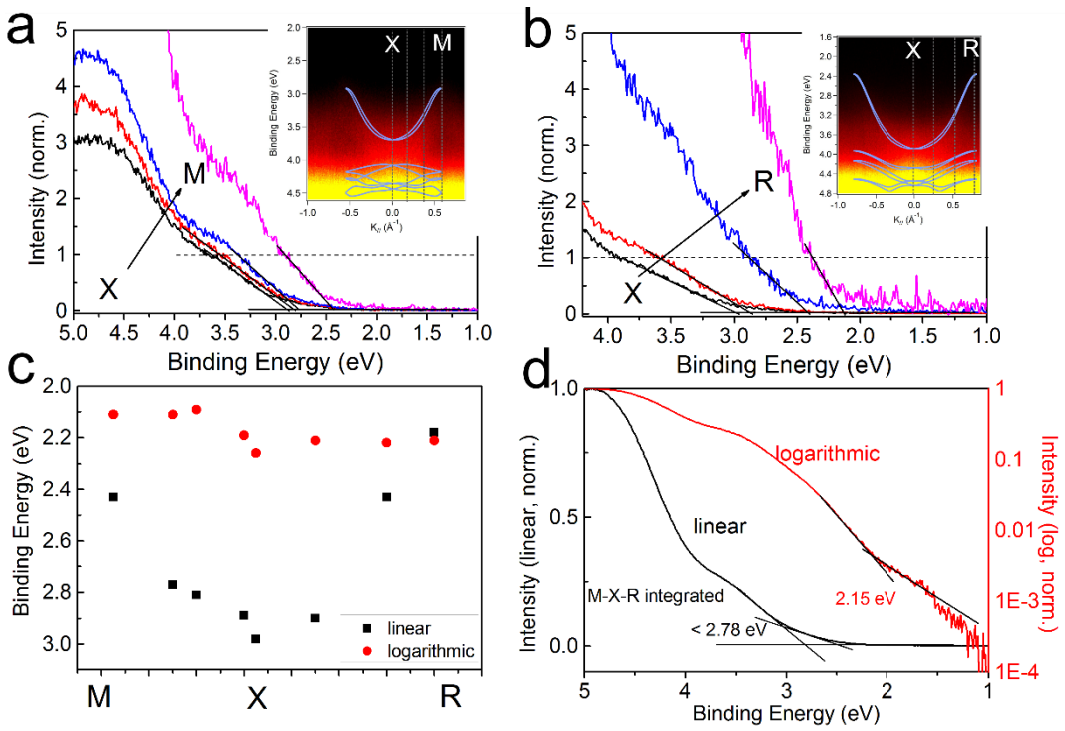

Figure 6.12 *Energy distribution curves (EDCs) and VBM determination for $MAPbBr_3$. (a) and (b): EDCs at selected k-values along the X-M and X-R directions, respectively. The corresponding k values for the EDCs are indicated by the vertical dashed lines in the ARPES k-space maps [insets in (a) and (b)]. Spectra are normalized at the corresponding top valence band peaks positions in order to better illustrate the k-dependence of the valence band onsets. (c) Valence band maximum determination from EDCs plotted in (a) and (b), using linear and logarithmic intensity scales for selected k values along M-X-R. (d) Simulated $MAPbBr_3$ polycrystalline thin film UPS spectrum, obtained by summation of all EDCs from (a) and (b), on linear and logarithmic scale, to highlight the variation in VBM determination. Figures are taken from [185].*

To further evaluate the reliability and universality of applying the semi-log plots for HaP thin films VB onset determination, two different $MAPbI_3$ polycrystalline thin films measured using two different photoemission systems for comparison are displayed in **Figure 6.13**. The overall valence band structures are very similar, with one apparent peak at 3.7 eV BE for both films (linear intensity scale). Similar to the observations made for the "artificial" thin film spectrum of **Figure 6.11** (d), the logarithmic-scaled intensity plots for both films lead to VB onset values within 1.4 – 1.5 eV that are close to the global VBM as

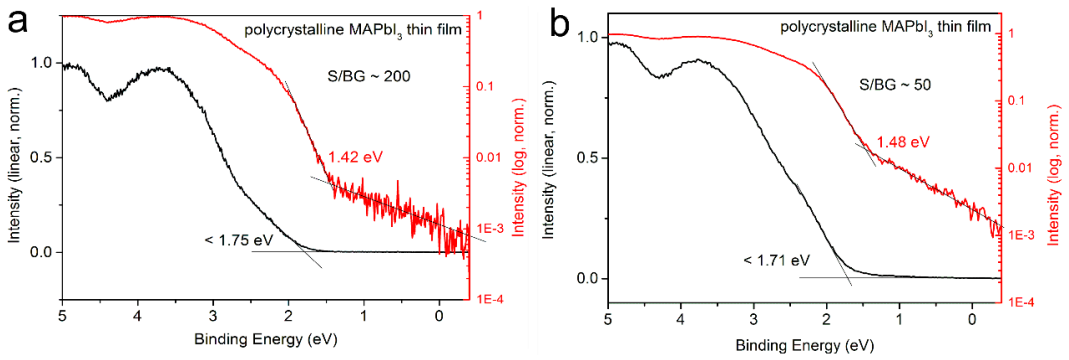

Figure 6.13 *UPS spectra of two different $MAPbI_3$ polycrystalline thin films measured using (a) SPECS Phoibos 150 analyzer (same system as ARPES) and (b) SPECS Phoibos 100 analyzer; the S/BG of the spectra differs by a factor of four (see* ***Figure 6.9*** *for details). Figures are taken from [185].*

determined previously. Furthermore, we note that the VB onset position of $MAPbI_3$ films varies with the density of surface states[184] and the history of exposure to water and oxygen[119], i.e., these values are sample-specific and not an intrinsic material constant. In contrast, the linear-scale plots give rise to overestimated and subjective VB onset BE. Therefore, as for standard PES measurements on polycrystalline $MAPbI_3$ films, semi-log plot can be preferably applied to estimate the VB onset, in agreement with the observation of Endres. *et al.*[34]

It is worth pointing out that the signal-to-background level differs by a factor of 4 between the two spectra shown in **Figure 6.13**; however, this impacts the onset determined in the semi-log plot by only ca. 40 meV, as demonstrated by the simulated Gaussian broadening in **Figure 6.9** . Similarly, we also show in **Figure 6.10** that even ca. twofold variation of the typical experimental broadening changes the VB onset determined on logarithmic intensity scale by only 50 meV. However, it is also important to note that HaPs films tend to form textured thin films with preferential surface orientation,[176, 186] as a result, the VB onset may not be probed from standard normal-emission PES measurements. Furthermore, a careful consideration of the presence and abundance of gap-states[140] as well as non-monochromated light source satellites is advisable when studying HaP thin films with PES.

6.3.3 Summary

From the experimental single crystal band structure measurements, the representative electronic spectra of polycrystalline thin films were constructed, revealing that the comparably small contribution from the global VBM at *R* to area- and angle-averaged spectra compromises a straightforward valence band onset determination of HaPs. As suggested earlier,[34] our study confirms that using a logarithmic intensity scale to determine the VB onset is thus preferable (with a remaining fundamental uncertainty of ca. 50 meV, mostly underestimating the onset BE), but all experimental parameters, such as instrumental limitations and sample gap-states, must still be carefully considered. It is particularly important to know the surface structure of thin films when discussing HaPs electronic properties in relation to energy levels in devices. We expect that the fundamental insights on thin film electronic spectra, derived from benchmark single crystal band structures, will enhance progress in device performance, as superior consistency of correlating electronic level alignment and device characteristics is readily enabled.

6.4 Surface electronic properties of halide perovskite thin films

In the following sections, the structural and electronic properties of HaPs thin films, covering a range of different compositions, will be presented. First of all, the surface electronic structure of $MAPbI_3$ thin films, as the prototype of HaPs, will be investigated. The aim of this study is to understand the behavior of the energetics of $MAPbI_3$ thin films upon varied excitation-intensity. Secondly, the surface electronic and chemical structures of $MAPbI_{3-x}Cl_x$ thin films upon illumination and the origin of the n-type behavior of the surface are investigated. In the last part of this section, the significance of SPV effect when characterizing perovskite systems using photoemission measurements is demonstrated.

6.4.1 **Origin of surface n-type character**

UPS studies of $MAPbI_3$ and $MAPbI_{3-x}Cl_x$ thin films have widely shown a strong n-type character on the surface, with E_F located very close (or even within) the CBM, given the transport gap of ca. 1.7 by combining UPS and inverse photoemission studies.[86, 127] Depending on the type of defects present in perovskites, first-principle calculations found that these materials can either be n-type (methyl amonium vacancy, iodine vacancy and lead interstitial), intrinsic, or p-type (lead vacancy).[169] Experimentally, regardless of the variations due to differences in sample composition and preparation,[33] employed substrates,[101] or even the method used for the VB onset determination,[34] most previous studies have reported n-type $MAPbI_3$ and $MAPbI_{3-x}Cl_x$ films. For instance, Miller et al.[101] have shown strong n-type behavior on n-type substrates and less n-type behavior on p-type substrates. To explain this discrepancy, Conings et al.[21] proposed that the strong n-type character of the perovskite surface is due to Fermi-level pinning induced by the presence of lead Pb^0 as shown by high-resolution XPS measurements. Another reason, as put forward by Wang et al.,[154] could be that the $MAPbI_3$ films formed from stoichiometry mixed precursors are nevertheless heavily n-doped. Nonetheless, it appears crucial to further explore the origin of n-type behavior of the perovskite surface in order to fundamentally comprehend the working mechanism of the corresponding devices.

In order to demonstrate the n-type character of HaPs thin films, UPS spectra of 4 different $MAPbI_{3-x}Cl_x$ thin films on PEDOT:PSS substrate prepared from different batches are shown in **Figure 6.14**. As we can see from the SECO region, all samples exhibit very similar work function, which gives rise to an average value at ca. 4.1 eV. Similarly, the valence bands for all samples, as presented in **Figure 6.14** (b), show very comparable electronic structure, leading to an average VB onset at ~1.6 eV extrapolated by linear intensity plots. Unambiguously, similar to the observation in the community, this implies that the Fermi level lies very close to the CBM, suggesting a strong n-type surface character given the transport gap of 1.7 eV.[127] Note that the above discussed VB onsets are

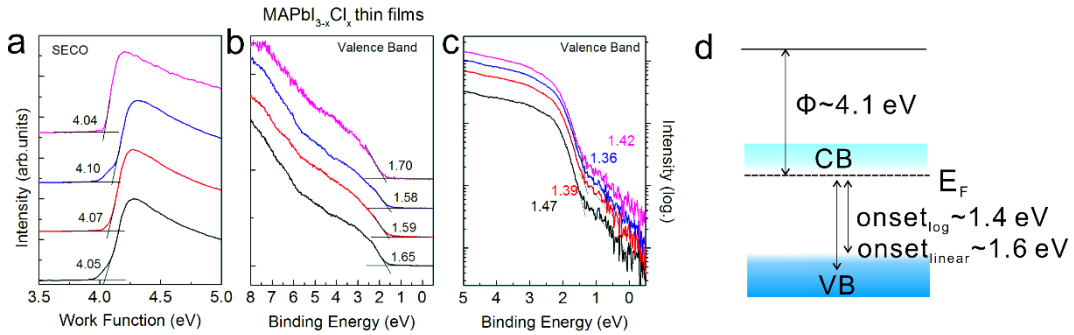

Figure 6.14 *UPS spectra of 4 different $MAPbI_{3-x}Cl_x$ thin films prepared from different batches. (a) SECO spectra, (b) VB spectra in linear intensity scale, (c) VB spectra in logarithmic intensity scale and (d) corresponding energy levels with respect to Fermi-level, exhibiting a n-type character on the perovskite surface.*

evaluated using linear extrapolation method. As a comparison, the valence bands are further exhibited by using semi-log plot in **Figure 6.14** (c). In analogous to the previous discussion, the VB onsets extrapolated using semi-log plots are overall smaller by ca. 0.2 eV in average than that of the linear extrapolated ones. For example, the first sample in black line shows the VB onset at 1.65 eV using linear plot, as compared to 1.47 eV using logarithmic plot. The details regarding such differences can be understood in section 6.3. Nevertheless, the puzzling origin of the n-type character on perovskite surfaces still remains.

Figure 6.15 shows the UPS measurements of a prototypical $MAPbI_3$ perovskite film where filters in different thicknesses were applied in order to attenuate the UV flux. By applying different filters, we are able to attenuate the UV flux by a factor of ca. 20 and ca. 500 when using thin and thick filters, respectively. Hereafter, UV_L and UV_M will denote the low (using thick filter) and medium (using thin filter) UV flux, respectively. In addition, UV_H refers to the high UV flux without filtering the UV light, as generated directly from the Helium discharge lamp. The UPS spectra of the $MAPbI_3$ films exhibit well-structured VB features, similar to that of the integrated $MAPbI_3$ single crystal spectra in **Figure 6.11** (d), indicating a high quality solution-processed $MAPbI_3$ film. The valence band maximum

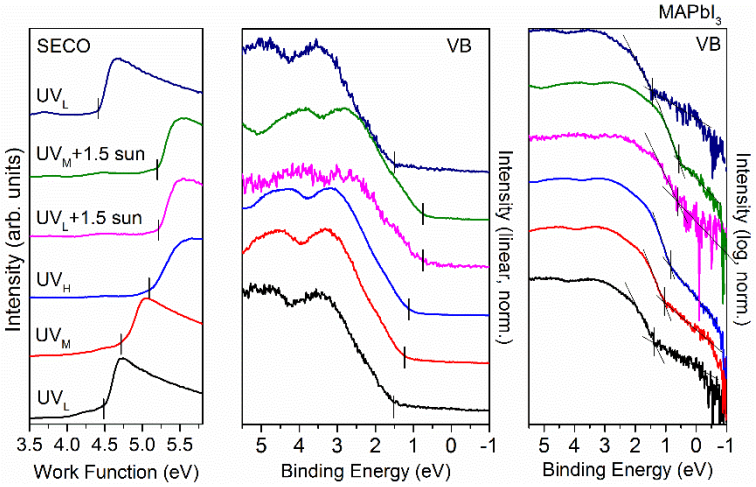

Figure 6.15 *UPS spectra of a $MAPbI_3$ thin film probed with varied incident UV flux and additional white light illumination (150 mW/cm²). Valence bands in linear and logarithmic intensity scale are presented in middle and right panels, respectively.*

is first determined using the linear extrapolation method. Initially, the VB $onset_{linear}$ is positioned at 1.51 eV BE probed using UV_L, similar to that of the $MAPbI_{3-x}Cl_x$ thin films, exhibiting a strong n-type character in the surface region. Upon increasing the UV flux, the VB $onset_{linear}$ decreases gradually to 1.23 eV using UV_M and to 1.12 eV using UV_H. Concomitantly, as shown from the SECO spectra in **Figure 6.15** (left), the work function continuously increases from 4.48 eV to 5.09 eV when switching from UV_L to UV_H. This trend of shifts in VB onset and work function against different UV flux represents the typical SPV effect, as illustrated in **Figure 2.5**, which has been widely observed to induce large variations in determining the Schottky-barrier at metal-semiconductor interfaces using PES technique.[3, 66] In this case, the perovskite surface demonstrates predominant n-type behavior as a result of downward surface band bending. During photoemission process, photo-generated electron-hole pairs are separated and redistributed by the electric field, producing an opposite voltage, which reduces the initial surface band bending of either direction.

This is well illustrated in **Figure 2.5** for a n-type surface, where the SPV can readily shift the energy levels and eventually lead to a flat band condition at sufficient illumination-intensity. In order to further address the effect of SPV at higher illumination-intensity, UPS

spectra were taken while the samples were further illuminated with white light at an intensity of 150 mW/cm^2, as also shown in **Figure 6.15**. It can be clearly seen that additional white light exposure further increases Φ up to 5.20 eV, accompanied with a decrease of VB onset$_{linear}$ down to 0.75 eV, giving rise to constant IE values at 6.0 ± 0.1 eV. Therefore, a flat band condition can be readily reached at sufficient illumination-intensity. We note that light exposure, neither UV light nor white light, was found to induce degradation and/or decomposition of the perovskite sample during the measurements, as Φ and VB onset values at UV_L exposure recover back to their typical initial values of 4.42 eV and 1.52 eV, respectively. In addition, no changes in VB structures can be seen, evident from a consistent lineshape throughout the measurements.

An alternative approach consisting of plotting the VB DOS in logarithmic intensity scale, as discussed in section 6.3, is also applied on the VB onset evaluation. The valence band spectra processed in this manner are also presented in **Figure 6.15** (right). We note that, as expected, the VB onsets using the semi-log extrapolation method are found to be ca. 0.15 eV in average smaller than those determined by the standard linear extrapolation. Specifically, with the semi-log scale extrapolation, the VB onset$_{log}$ is originally found at 1.37 eV when using UV_L. It monotonously decreases with increasing photon flux and saturates at 0.58 eV using UV_M with additional white light illumination due to SPV. Interestingly, we stress that upon reaching flat band condition, the VB onset$_{log}$ at 0.58 eV away from E_F indicates a p-type character in the bulk, in agreement with the observations from Hall effect measurements.[25, 131]

The Φ and VB onset values against varied illumination conditions are summarized and plotted in **Figure 6.16**. Notably, the trend of Φ and VB onset values as a function of illumination conditions undoubtedly demonstrates that SPV due to optical excitation can strongly affect the determination of the energy levels of perovskite surface. Such shifts in energy levels can be interpreted as reflecting the magnitude in surface band bending at

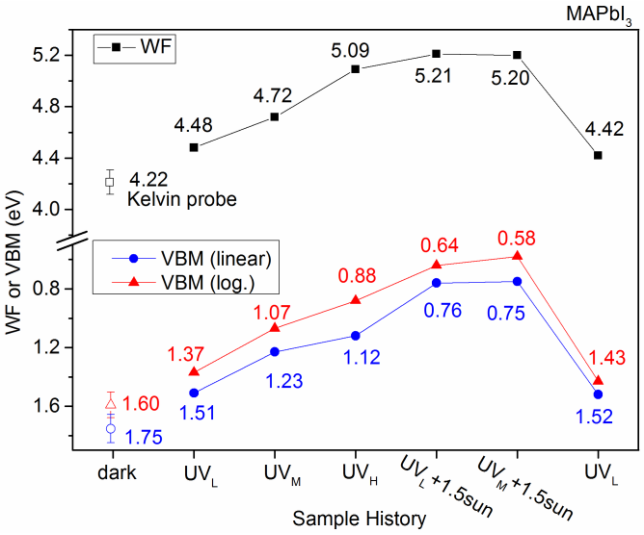

Figure 6.16 *Summarized work function and VBM values extrapolated using linear and logarithmic intensity plots at varied excitation flux from* ***Figure 6.15****. Work function in dark is determined from KP measurements. VBM values in dark are extrapolated by taking into account of the averaged WF difference between KP and UPS data, i.e.* $VBM_{dark} = \frac{(VBM_{sat}+\Delta WF_{sat-dark})+(VBM_{UV_L}+\Delta WF_{UV_L-dark})}{2}$*, where sat stands for saturation.*

sufficient light intensity. We argue that the back contact effect (i.e. the interface between perovskite and substrate) can be ruled out as the SPV already takes place by varying the UV flux only, which is expected to be attenuated significantly within 20 nm. The origin of surface band bending in perovskites will be discussed in the following section.

The above findings on the SPV effect were additionally investigated and confirmed by means of Kelvin probe method. As described in section 4.2, this technique has been applied to measure the contact potential difference between the reference electrode and the sample surface. Thus, the samples' surface potential or Φ can be derived given a known electrode Φ. In this study, the measurements were conducted in inert atmosphere while switching between dark and under illumination. Therefore, this technique allows us to access the perovskites Φ in completely dark condition, as well as under white light illumination. It is worth noting that for both experiments (UPS and CPD) the same set of samples were investigated, ensuring consistent results. **Figure 6.17** shows the Φ values as a function of time, derived from CPD measurements, of the $MAPbI_3$ thin film when

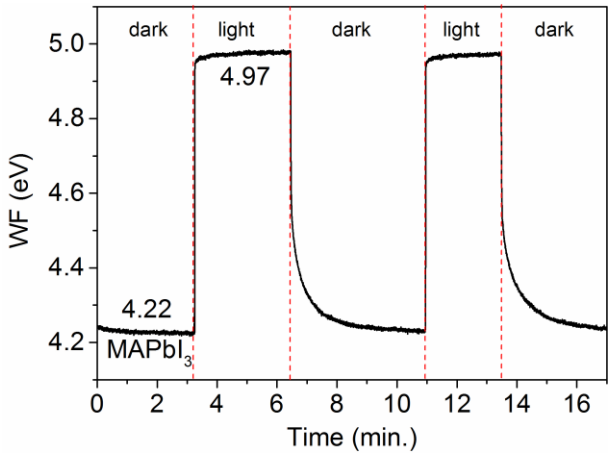

Figure 6.17 *KP measurements of the $MAPbI_3$ thin film over multiple on-off illumination cycles. White LED light was used for illumination with corrected intensity at 20 mW/cm².*

switching between dark and under illumination. It can be clearly seen that starting with a Φ at 4.22 eV in dark, upon illumination, we observe a steep increase of Φ, which immediately saturates at 4.97 eV. For the next on-off illumination cycles, the shifts in work function are found to be completely reversible. Interestingly, a low decay process is noted when switching back to dark condition. Clarifying the reason for this observation goes beyond the scope of this study, nevertheless, we suggest that it is possibly related to the releasing of trapped slow carriers within the material.[82] In any case, the difference in surface work function in dark and under illumination represents the same trend that was demonstrated from UPS measurements with varied excitation flux. Therefore, these results strongly support the interpretation of SPV effect in $MAPbI_3$ thin films and elucidate the downward surface band bending at $MAPbI_3$ surface. We note that, as one would expect, the work function (4.22 eV) probed by KP method is slightly smaller than the value (4.48 eV) determined by UPS even at UV_L, which strongly suggests that probing the energy levels using UPS technique even at low photon flux can be already problematic. Hence, attention must be paid in photoemission studies for characterizing the electronic structure of HaPs thin films, as the SPV can lead to variations in interpreting the energy levels.

6.4.2 Impact of illumination on electronic and chemical structures

The focus in this section is to unravel the origin of the surface band bending as observed from SPV effect in the previous section, and to develop a comprehensive understanding of the surface electronic and chemical properties upon illumination. In this section, the thick filter is applied constantly for all UPS measurements unless otherwise specified. UPS measurements were performed while the sample was illuminated using white light.

Figure 6.18 shows the UPS spectra of a $MAPbI_{3-x}Cl_x$ perovskite thin film illuminated with white light of gradually increasing intensity during UPS measurements. Initially, the VB $onset_{linear}$ is found at 1.73 eV BE in dark. Similar to the previous observation in 6.4.1, a continuous shift of the VB onset towards lower BE is noted when increasing the illumination-intensity from 5 up to 67 mW/cm^2 over a period of 30 min. Equivalent shifts

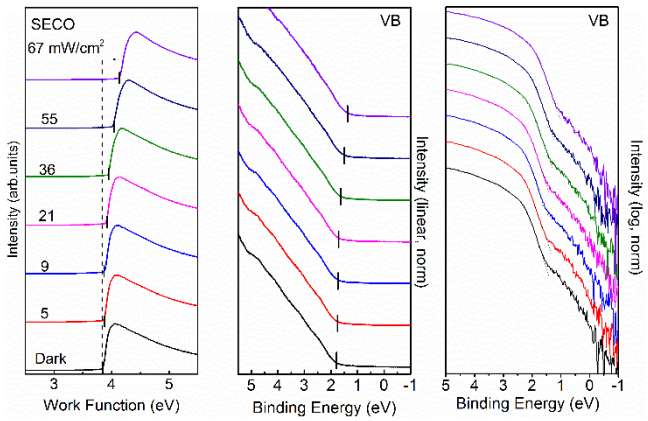

Figure 6.18 *UPS spectra of a $MAPbI_{3-x}Cl_x$ thin film on PEDOT:PSS substrate as a function of illumination power density over time. left: SECO region, middle and right panels: VB region in linear and logarithmic intensity, respectively. Figures are adapted from [184].*

of Φ towards high values are also observed. This evokes again the effect of surface photovoltage when optical excitation is employed. Time-dependent UPS spectra with illumination at constant intensity is further conducted, as shown in **Figure 6.19**. In this case, the VB $onset_{linear}$ continuously increases and saturates at 1.09 eV. This is accompanied by a work function increase from 3.85 eV to 4.59 eV, giving rise to constant ionization energy

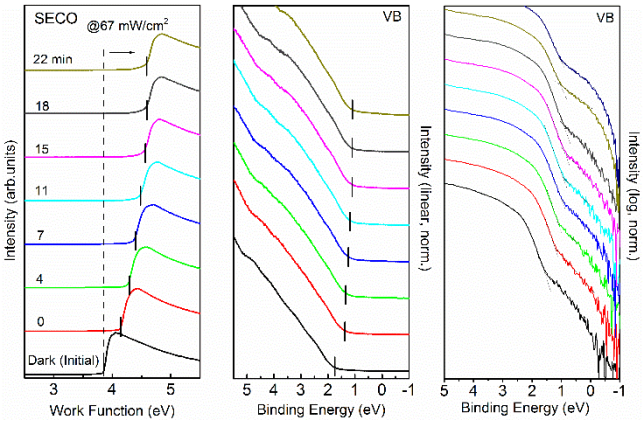

Figure 6.19 *Time evolution of the UPS spectra of the $MAPbI_{3-x}Cl_x$ thin film when illuminated at constant power density (67 mW/cm²). left: SECO region, middle and right panels: VB region in linear and logarithmic intensity, respectively. Figures are adapted from [184].*

values. The same observation is also noted for the VB onset extrapolated from logarithmic intensity plots, as presented in **Figure 6.18** and **Figure 6.19** (right panels). The VB $onset_{log}$ is found to decrease from 1.57 eV and saturate at 0.90 eV under illumination, consistent with changes by ca. 0.6 eV for the VB $onset_{linear}$. Since changes upon illumination are material related property and are independent on the extrapolation methods, in the following discussions, the VB onset, unless specified, will only be evaluated by linear intensity plots.

The work function and VB onset values from above UPS spectra are summarized in

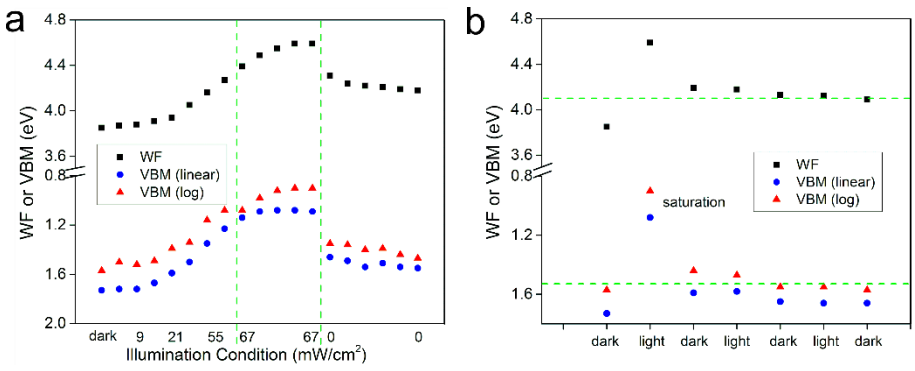

Figure 6.20 *(a) Evolution of work function and VBM values (extrapolated from linear and logarithmic intensity scale) determined from* ***Figure 6.18*** *and* ***Figure 6.19*** *as a function of illumination intensity and time..(b) Stabilized work function and VBM values for multiple consecutive on-off illumination cycles at 67 mW/cm². UPS spectra can be found in Appendix (****Figure 8.3****). Figures are adapted from [184].*

Figure 6.20 (a), upon illumination, Φ is found to increase, accompanied with a decrease with VB onset, essentially exhibiting photon flux dependent energy levels. Noteworthy, as shown in **Figure 6.20** (b), after one illumination cycle the VB onset does not recover fully to its initial value. For next on-off illumination cycles, the SPV is suppressed and the VB $onset_{linear}$ is fixed at 1.6 eV BE, very close to the initial value. The UPS spectra can be found in Appendix **Figure 8.3**. This indicates that light-induced chemical modification might occur, which quenches the surface photovoltage phenomenon as observed for subsequent illumination cycles.

To explore the origin of such chemical modification induced by illumination, stronger illumination intensities are employed during UPS measurements. In addition, XPS analysis is also performed on the perovskite sample before, under and after illumination in order to investigate the chemical changes, with the focus on Pb and I core levels in order to obtain high photoemission yield. As shown in **Figure 6.21** (a) for the valence band and SECO spectra of a $MAPbI_{3-x}Cl_x$ perovskite film, the VB $onset_{linear}$ decreases initially from 1.63 eV to 0.93 eV BE within a period of 7 min upon illumination (154 mW/cm^2). Simultaneously, the work function increases, equivalently, from 4.10 eV to 4.83 eV, giving rise to a constant ionization energy of 5.7 eV. Noteworthy, as displayed in **Figure 6.21** (b)

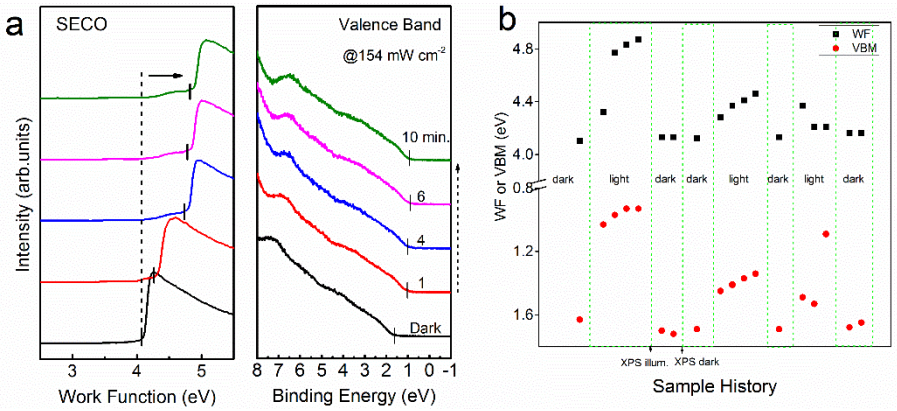

Figure 6.21 *(a) Time-dependent UPS spectra of a $MAPbI_{3-x}Cl_x$ thin film illuminated at constant intensity (154 mW/cm^2). (b) Evolution of the work functions and VB onsets over multiple on-off illumination cycles. The SECO and valence band spectra are attached in Appendix (**Figure 8.4**). The vertical dashed green lines indicate the moment at which the light was switches on or off. Figures are adapted from [184].*

over multiple illumination cycles, the VB $onset_{linear}$ and work function values are found to recover fully to its initial BE values after first illumination cycle. Again, this observation of the shifts in energy levels upon illumination is reminiscent of typical band flattening of a semiconductor, i.e. the surface photovoltage effect,[82] which is schematically illustrated in **Figure 2.5**. We note that the shifts in energy levels for $MAPbI_{3-x}Cl_x$ are not instantaneously saturated upon illumination, which are not yet fully understood. However, it is likely linked to the fact of photo-curing behavior, from which the charge carrier lifetime is enhanced upon radiation.[106]

As the described energy shifts are of electrostatic origin, they are also observed from XPS measurements, as shown in **Figure 6.22** (a) and (b) for Pb 4f and I 3d core levels, respectively. We can see that similar to the shifts of valence band, the core levels exhibit 0.69 eV shift towards lower BE upon illumination, and recover completely to their initial binding energies in dark condition. As we further noted, the SPV effect is reversible for the first-two illumination on-off cycles only, prolonged illumination results in quenching of the SPV effect, resulting in the pinning of Fermi level at the CB minimum in **Figure 6.21** (b).

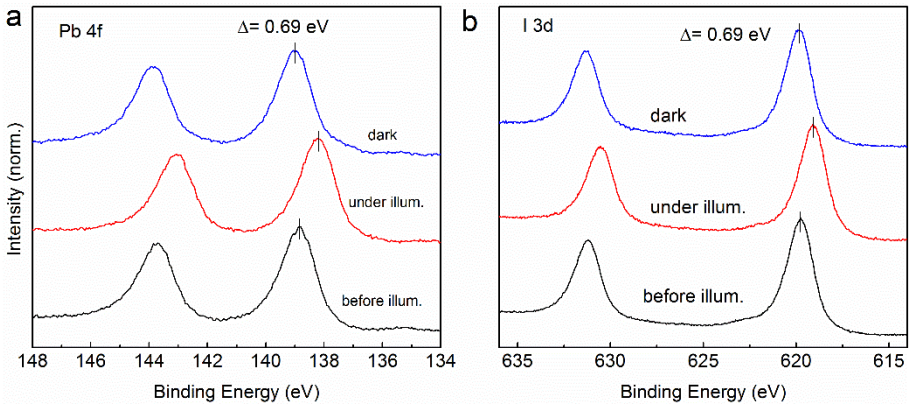

Figure 6.22 *Pb 4f and I 3d core levels measured on the perovskite films before, under and after illumination. The moments at which point the XPS measurements were taken are indicated in* ***Figure 6.21*** *(b). Figures are taken from [184].*

To further explore the origin of such Fermi level pinning induced by light exposure, XPS measurements were performed after multiple illumination on-off cycles for different take-off angles, as displayed in **Figure 6.23** (a). We note that the Pb 4f core levels are very different from that of the pristine sample, which exhibit, apart from the Pb 4f main peaks of 5/2 at 143.7 eV and 7/2 at 138.8 eV from perovskite structure, two additional peaks at lower BE. These two peaks at 142.0 eV and 137.1 eV at lower BE have been recently attributed to elemental Pb^0.[21, 122] In addition, angle-dependent XPS measurements show that the relative amount of $Pb^0/Pb2^+$ increases by ca. 30% when tuning from normal emission to 80° emission measurements. This implies that the Pb^0 species are enriched in the surface region. Such large amount of Pb^0 on the surface can be further confirmed from UPS results, where the spectrum in **Figure 6.23** (b) displays a clear Fermi edge at 0 eV BE. These findings suggest that such amount of Pb^0 on the surface after prolonged illumination are expected to induce strong Fermi level pinning, which quenches the SPV effect. In fact, the Pb^0-related defects in very small fraction could already initially act as an electron donor on the pristine films, which gives rise to the n-type behavior of perovskite surface, as schematically shown in **Figure 6.24**. This is also confirmed from Sadoughi et al.[122] that

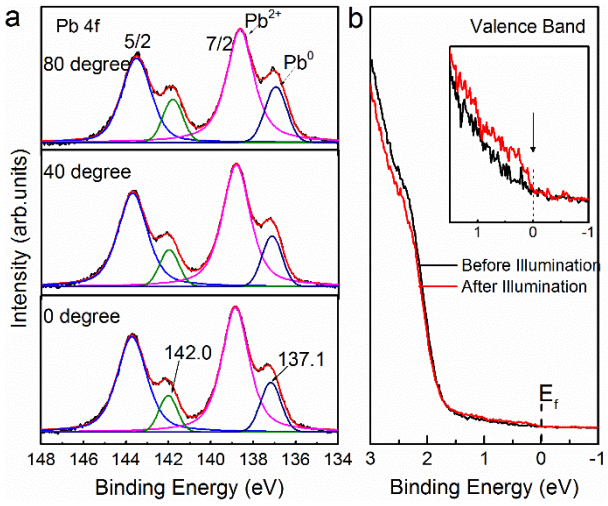

Figure 6.23 *(a) angle-dependent XPS spectra of a $MAPbI_{3-x}Cl_x$ thin film (sample from above figure) after prolonged illumination cycles. Background of secondary electrons is subtracted. (b) UPS spectra at top valence band region of the sample. Inset: zoomed-in valence band region in the vicinity of the Fermi level. Figures are reproduced from [184].*

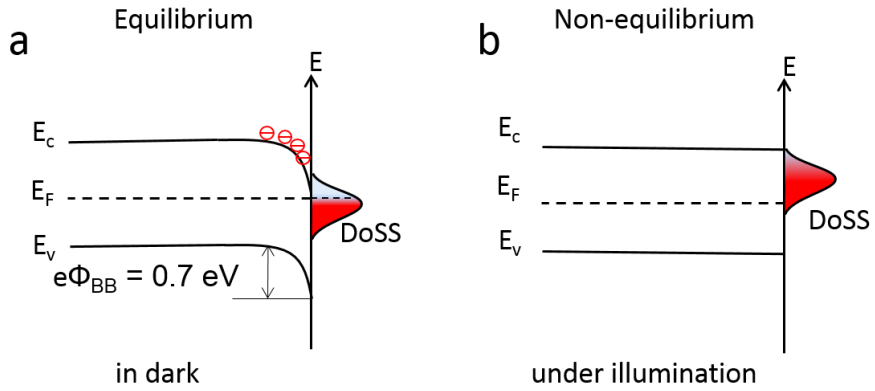

Figure 6.24 *Energy band diagram for perovskite thin films (a) at thermal equilibrium and (b) non-equilibrium as a result of surface photovoltage. $e\Phi_{BB}$ corresponds to the magnitude of surface band bending. DoSS: density of surface states.*

the presence of metallic Pb after standard annealing only is observed from hard X-ray measurements, further supporting the idea that the metallic Pb act as donor levels already on the pristine films.

Furthermore, UV-vis measurements reveal the fact that the changes induced by prolonged illumination are found not only in the surface region, but also in the bulk of the films. This can be observed from the absorption spectra of the perovskite film before and after prolonged illumination in our UHV chamber, as shown in **Figure 6.25**. After illumination, the absorbance decreases, accompanied with a new feature at ca. 500 nm. The latter, which is also present in the absorption spectrum of a pure PbI_2 film, is characteristic of the formation of PbI_2 in the film. This observation on the illumination induced degradation, notably into PbI_2 species, has been recently demonstrated in recent reports.[2,

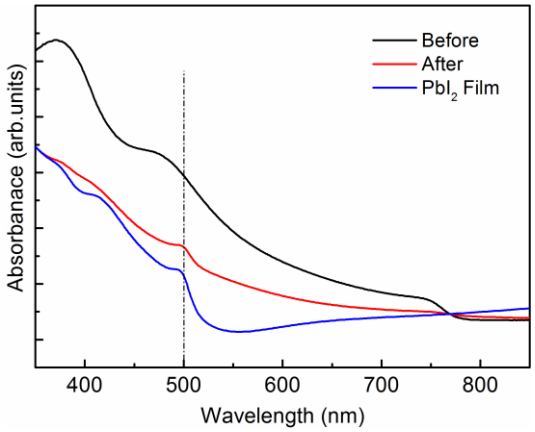

Figure 6.25 *UV-vis absorption spectra of a pristine $MAPbI_{3-x}Cl_x$ perovskite film before (black), after prolonged illumination (red) and a PbI_2 film (blue). Figure is taken from [184].*

174] In addition, the results reveal that the degradation of HaPs thin films into PbI_2 and metallic Pb species upon illumination occur in a short period of time in UHV condition.

We further note that upon white light illumination, the sample temperature rose up to ca. 50 °C. In order to rule out any heating-related effect, photoemission measurements were performed on $MAPbI_{3-x}Cl_x$ films while the samples were gradually annealed up to ca. 54 °C over a period of 30 min. As shown in **Figure 6.26** for a perovskite sample measured at 34 °C and 54 °C, respectively, no significant shifts in energy levels in the UPS spectra can be seen from heating effect. The VB $onset_{linear}$ remains constant at ca. 1.6 eV BE while the work function fluctuates slightly within 0.2 eV. The latter can be due to the desorption of

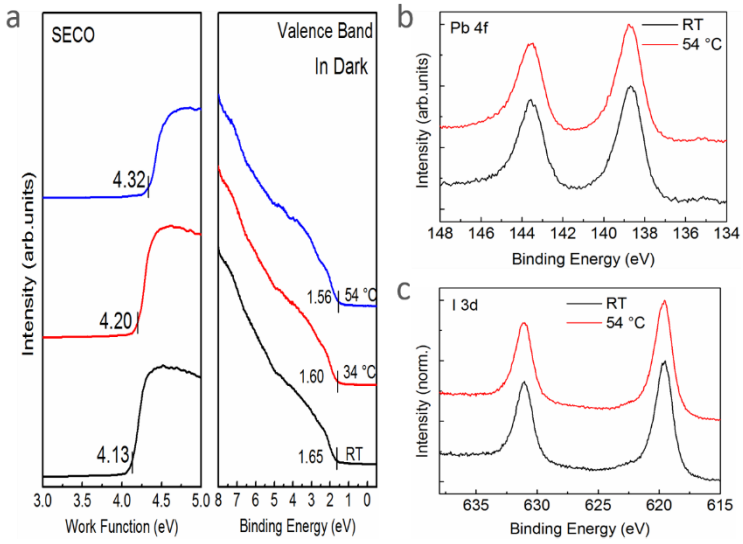

Figure 6.26 *(a) Temperature dependent UPS spectra of a $MAPbI_{3-x}Cl_x$ perovskite film. The measurements were performed at RT, 34 °C and 54 °C, respectively. (b) Pb 4f and I 3d core levels measured at RT and after annealing at 54 °C. Figures are taken from [184].*

water residues upon mild heating in UHV condition.[119] In addition, the Pb 4f and I 3d core levels do not exhibit changes in terms of BE and lineshape, as shown in **Figure 6.26** (b) and (c) respectively. Hence, a mild heating on perovskite in UHV condition does not noticeably modify the electronic and chemical structure of perovskite films. However, it becomes largely possible that the increased temperature upon illumination could accelerate the perovskite degradation process into metallic Pb and PbI_2. This is indeed observed by Misra et al.[102] that the perovskite films are stable to 100 suns at ca. 25 °C, but suffered

degradation around 50 °C.

6.4.3 **Effect of SPV in characterizing halide perovskites**

In order to further demonstrate and investigate the general observation of SPV when characterizing HaPs thin films using optical techniques, similar experiments were performed on mixed cations and halides perovskites, which have been extensively explored as efficient light absorber in perovskite solar cells.[95, 116, 135-136] Following above described procedure, UPS measurements were performed on $FA_{0.83}MA_{0.17}Pb(I_{0.83}Br_{0.17})_3$, $Cs_{0.05}[FA_{0.83}MA_{0.17}Pb(I_{0.83}Br_{0.17})_3]_{0.95}$ and $Rb_{0.05}\{Cs_{0.05}[MA_{0.17}FA_{0.83}Pb(I_{0.83}Br_{0.17})_3]_{0.95}\}_{0.95}$ perovskite thin films, respectively. Hereafter, we use the nomenclature of FAMA, CsFAMA and RbCsFAMA to denote the different perovskite compositions. We observed, similar to the results obtained from $MAPbI_3$ and $MAPbI_{3-x}Cl_x$ samples, that all samples exhibit excitation-intensity dependent energy level shifts in UPS measurements, elucidating that strong SPV can readily take place within varied UV flux for mixed cations and halides perovskites. The UPS spectra as a function of illumination-intensity of the mixed perovskites can be found in the Appendix 8.2.3. The summarized Φ and VB onset values against varied illumination-intensity as obtained from UPS are reported in **Figure 6.27**. Clearly, for all studied perovskites, the trends, the magnitude of the energy shifts as well as the absolute values in their energy levels under illumination are comparable to those observed for $MAPbI_3$, suggesting the same physics being at play.

As displayed in **Figure 6.27** (a) for FAMA, equivalent shifts in Φ and VB onset values can be seen at varied excitation-intensity. Starting at 4.37 eV using UV_L, the Φ shifts with increasing UV flux and further shifts up to 5.25 eV using additional white light illumination at UV_L, which is concomitant with the VB $onset_{linear}$ shifts decreasing from 1.54 eV down to 0.83 eV extrapolated from linear intensity plots. Equivalent estimation by using semi-log method locates smaller VB $onset_{log}$ values, which decrease gradually from 1.38 eV at low excitation-intensity and saturate at 0.60 eV at sufficient illumination-intensity. Furthermore, results of CsFAMA and RbCsFAMA thin films exhibit essentially the same trend as observed above. For CsFAMA shown in **Figure 6.27** (b), the Φ shifts from 4.29 eV using UV_L up to 5.15 eV with additional white light illumination. Equivalently, VB

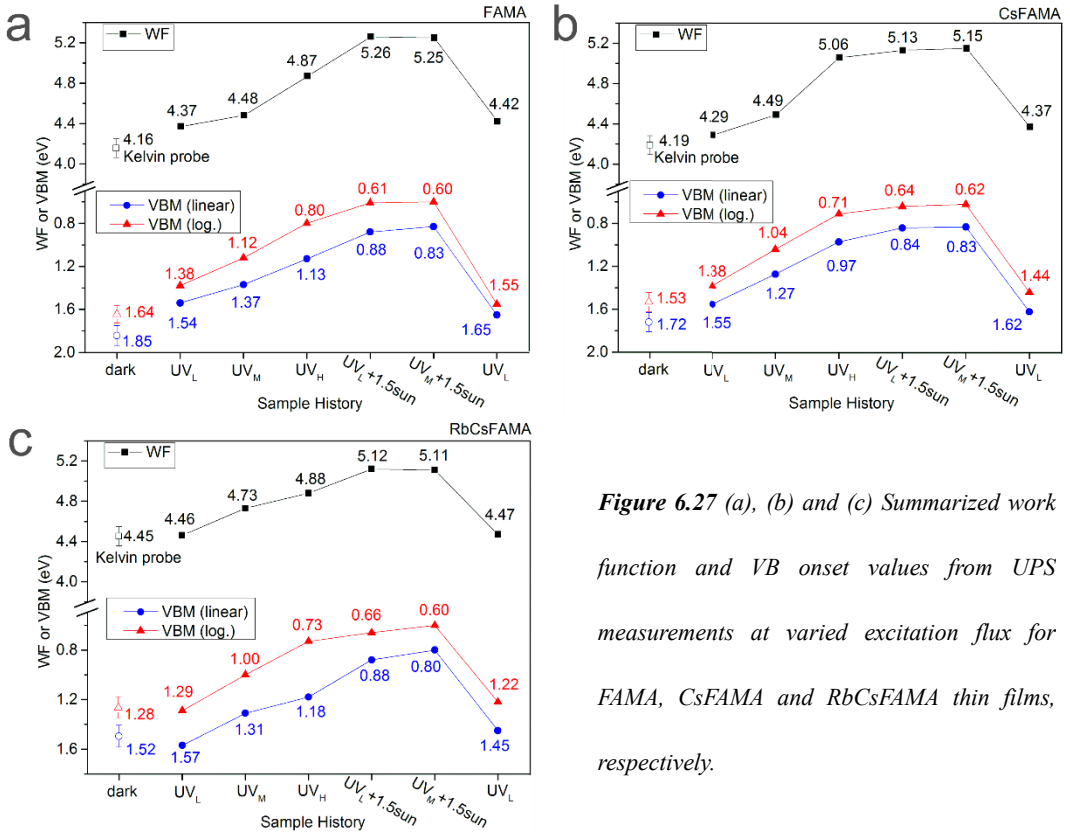

Figure 6.27 *(a), (b) and (c) Summarized work function and VB onset values from UPS measurements at varied excitation flux for FAMA, CsFAMA and RbCsFAMA thin films, respectively.*

onset was reduced from 1.55 eV to 0.83 eV and from 1.38 eV to 0.62 eV by applying linear and semi-log plots, respectively. As for RbCsFAMA thin films in **Figure 6.27** (c), analogously, the Φ increases from 4.46 eV and saturates at 5.11 eV at sufficient illumination-intensity, in parallel to the changes in VB onset values from 1.57 eV to 0.80 eV by using linear plots and from 1.29 eV to 0.60 eV by using semi-log plots. We also note

that, for mixed perovskite samples, the top valence band exhibits globally similar electronic structure, which can be understood since the cations do not contribute directly to the frontier bands.[14, 169] The above observations clearly demonstrate the significant effect of SPV on the observed energy levels by the means of UPS technique. Already at room temperature, upon illumination, ionized surface states induced surface band bending can be largely reduced as driven by the redistribution of photo-generated charge carriers. Consequently, large variations of the key parameters of the electronic structure, i.e., Φ and VB onset, of hybrid perovskites can be readily observed by UPS. Therefore, reduction of the excitation flux in UPS appears as highly recommended in order to access the perovskite intrinsic electronic structure. Furthermore, this may be one of the key reasons that makes perovskite based optoelectronic devices perform so well, as surface defects are compensated or filled under illumination, thus not impeding long-carrier lifetimes through trap-assisted recombination.[23, 137, 167].

Further evidence for the presence of SPV effect for mixed perovskites can be found from KP measurements, which were sequentially performed in dark and under illumination. Similar to the changes in surface potential (or surface Φ) for $MAPbI_3$ thin film in **Figure 6.17**, results of FAMA, CsFAMA and RbCsFAMA exhibit essentially the same surface potential dependence against illumination, as presented in **Figure 6.28** (a), (b) and (c), respectively. The difference in surface potential between dark and light amounts to 0.9 eV for FAMA and CsFAMA thin films, and a slightly smaller value of 0.6 eV for RbCsFAMA thin films, which is consistent with the observed SPV effect deduced from the energy levels shifts in UPS spectra. It is noteworthy that the shifts in surface potential are completely reversible over multiple on-off illumination cycles, which could exclude light-induced chemical reaction in the films, however, the redistribution of ions and/or ions vacancies cannot be excluded. In fact, we note that the slow decreasing of sample Φ under illumination is possibly due to an increase of tip Φ. As reported by Zhang *et al*..[172] that perovskites tend to decompose into halide species upon supra band gap illumination which

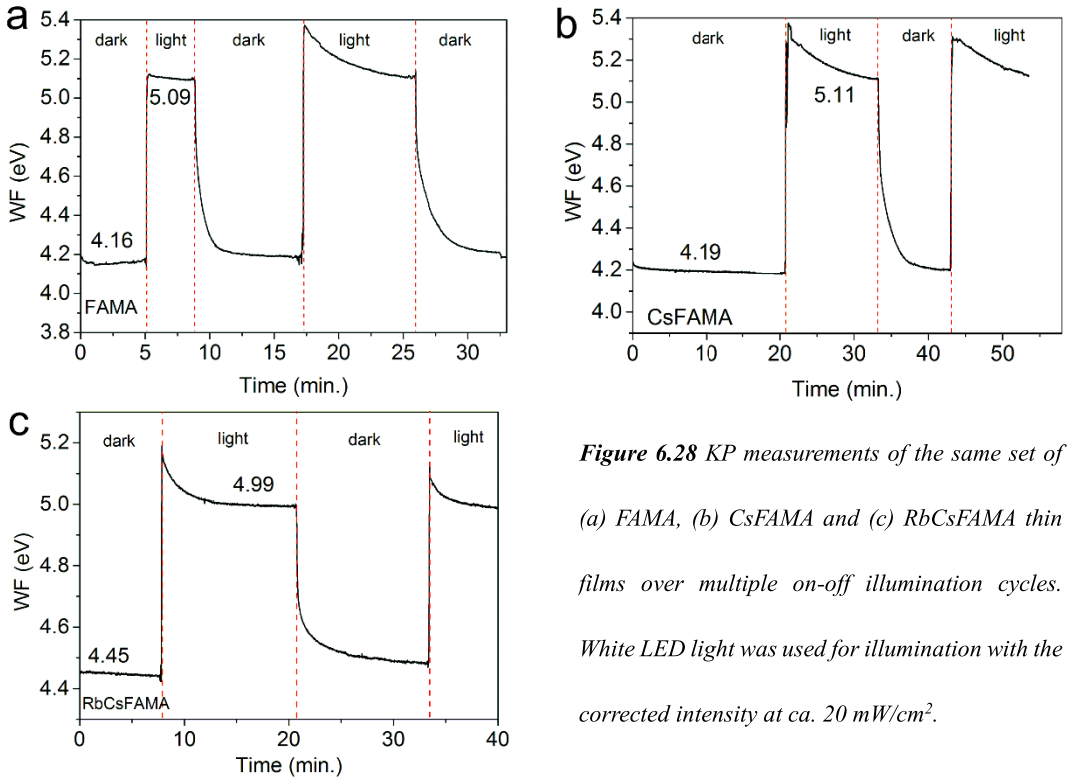

Figure 6.28 *KP measurements of the same set of (a) FAMA, (b) CsFAMA and (c) RbCsFAMA thin films over multiple on-off illumination cycles. White LED light was used for illumination with the corrected intensity at ca. 20 mW/cm².*

could contaminate the gold tip. Individually, as expected, the surface potential probed by KP in dark is slightly smaller than that of the value determined by UPS measurements even at UV_L, i.e., 4.16 ± 0.09 eV against 4.37 eV for FAMA, 4.19 ± 0.09 eV against 4.29 eV for CsFAMA and 4.45 ± 0.09 eV in contrast to 4.46 eV for RbCsFAMA. The above observation demonstrates the fact that it can be challenging to experimentally determine the intrinsic optoelectronic properties when optical excitation is inevitably employed.

6.4.4 **Summary**

In this subchapter, it was firstly shown that the widely observed n-type electronic character of the $MAPbI_3$ thin films can be attributed to the presence of surface band bending. The associate surface band bending was demonstrated by means of SPV, with its presence, a shift as large as of 0.5 eV in energy levels is observed for $MAPbI_3$ thin films solely from UPS measurements. Subsequently, fundamental different energy level alignments can be established derived from photoemission measurements. By applying additional white light illumination, further shifts in energy levels by 0.7 eV can be achieved, reaching a flat band

condition at sufficient illumination-intensity. The SPV effect in optical measurements were further investigated and confirmed by means of macroscopic KP method. Similar to the observation from photoemission results, shifts in Φ as large as 0.7 eV are obtained from the CPD measurements when switching between dark and light condition.

In addition, measurements on $MAPbI_{3-x}Cl_x$ thin films further demonstrate the presence of SPV, from which, the VB onset moves by ca. 0.7 eV towards mid-gap probed by UPS under additional white light illumination. It was further shown that the SPV effect is only reversible as a substantial amount of elemental lead are increasingly generated upon prolonged illumination in UHV condition. The resulting high density of Pb^0 can lead to strong Fermi level pinning at CBM, which quenches the SPV effect and gives rise to even stronger n-type surface. Additionally, the $MAPbI_{3-x}Cl_x$ thin films are found to partially degrade into PbI_2 in a rather short time (minutes) in UHV condition, which poses further challenges to employ perovskite-based photovoltaics in cosmic space.

In the end, the general observations of SPV on a set of mixed cations and halides perovskites were further demonstrated by combing photoemission and KP methods. We observed, essentially the same results as obtained from $MAPbI_{3-x}Cl_x$ and $MAPbI_3$ perovskites, that all samples exhibit excitation-intensity dependent shifts in energy levels, elucidating that strong SPV can readily take place within varied UV flux for mixed cations and halides perovskites. This demonstrates that caution must be taken when performing optical measurements on HaPs materials.

6.5 Energy levels alignment at halide perovskite/electron acceptors interfaces

In the previous sections, we have demonstrated that the presence of surface states, possibly originating from metallic lead species, can induce large modifications on the surface electronic structure of HaPs thin films. Particularly, the donor-type surface states can result in strong downward surface band bending, giving rise to the widely observed n-

type character of the HaPs thin films.

Discrepancies have been established in the progress of understanding the energy level alignment when forming functional interfaces between perovskites and transport layers. Noteworthy, several studies have reported different and even conflicting interface ELA scenarios even for the same material combinations. For example, Schulz *et al.*[128] reported that flat band condition holds and no band bending was observed in perovskite ($MAPbI_3$) layer when forming interfaces with C60. In contrast, another study by Wang *et al.*[153] found an upward band bending in perovskite layer accompanied by an upward shift of energy levels in C60 layer. These discrepancies might be, at least partially, ascribed to different perovskite preparation conditions,[33, 67] and thus the probed ELA, however, fundamental understanding of such correlation is still lacking. In this section, we will further demonstrate that the presence of surface states, depending on the initial density, can play a crucial role in determining the energy level alignment at HaPs/charge transport layers.

To qualitatively demonstrate and evaluate the impact of surface states on the ELA, three different perovskite sample series with strongly varying density of surface-states (DoSS) were employed. These samples are (i) pristine perovskite thin films with low-DoSS, (ii) perovskite thin films illuminated with white light, thus exhibiting high-DoSS, and (iii) single crystals displaying relatively high-DoSS. By using strong electron acceptor molecules, different ELA scenarios with variations of up to 0.6 eV BE in these perovskite substrates can be realized and understood by means of UPS and XPS.

6.5.1 **Low-DoSS perovskite/acceptor interfaces**

The electronic structure at the interface between the low-DoSS $MAPbI_{3-x}Cl_x$ perovskite substrates and the molecular acceptors are presented at first. **Figure 6.29** (a) and (b) show the evolution of the SECO and VB spectra as a function of nominal HATCN layer thickness, respectively. Initially, similar to the observations on the pristine electronic structure discussed above, the pristine perovskite film exhibits a Φ of 4.34 eV and VB onset

at 1.50 eV BE, indicating again a strong n-type electronic character on the surface. Upon molecular deposition with HATCN, the Φ increases gradually and eventually saturates at 5.49 eV at 128 Å nominal thickness for HATCN layer. Further deposition of HATCN layer up to 192 Å nominal thickness results in no change of Φ, implying a complete coverage of HATCN layer on the perovskite surface. The increase of Φ can be ascribed to the net charge transfer from perovskite substrate to molecular acceptors in order to reach electronic equilibrium across the interface, as the electron affinity of the HATCN molecules (in the range of 4.9 - 5.4 eV[84, 170]) is higher than the perovskite Φ. In such case, the acceptor LUMO level is expected to be pinned at substrate Fermi level in order to establish electrostatic equilibrium. Concomitantly, the evolution of VB spectra, upon increasing HATCN film thickness, reveals that the perovskite-related features become attenuated and shift to lower BE, as shown in **Figure 6.29** (b). From the VB spectra we can see that from 8 Å on, the HATCN HOMO peak at ca. 4.9 eV BE can be identified. We note that, a DOS with the peak position at ca. 1.8 eV is observed for HATCN thickness ranging from 2 Å up

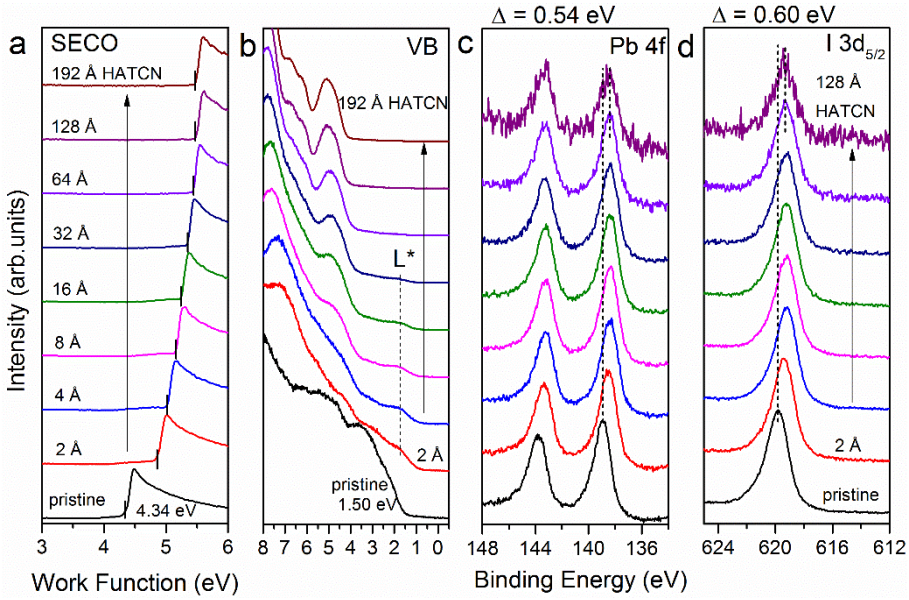

Figure 6.29 *(a) SECO, b) VB and core level spectra of c) Pb 4f and d) I $3d_{5/2}$ as a function of HATCN film thickness on pristine (low-DoSS) perovskite ($MAPbI_{3-x}Cl_x$) thin film. L^* indicates the (partially) filled LUMO of HATCN molecules. The VBM of the pristine perovskite is determined to be at 1.50 eV, indicating a strong n-type surface. Dashed lines in the core level spectra are guides to the eye and the core level shifts are indicated as "Δ". Figures are taken from [186].*

to 32 Å. As this DOS is neither present for the pristine perovskite spectrum nor for that of the thick HATCN layer, it is assigned to the interface states, likely corresponding to (partially filled) LUMO levels upon charge transfer.[4]

The observed change in Φ (ΔΦ) originates from two contributions: i) a change in perovskite surface band bending ($\Delta\Phi_{BB}$), and ii) the formation of an interface dipole ($\Delta\Phi_{ID}$) due to charge transfer, such that $\Delta\Phi = \Delta\Phi_{BB} + \Delta\Phi_{ID}$.[125-126] As we know that the $\Delta\Phi_{BB}$ can be straightforwardly determined by monitoring the energy shifts of the perovskite VB and core levels upon molecular adsorption, in this study, $\Delta\Phi_{BB}$ will be accessed directly from Pb 4f and I $3d_{5/2}$ core level energy shifts as also shown in **Figure 6.29** (c) and (d). We can observe that upon increasing HATCN layer thickness, both core levels exhibit shifts towards lower BE. Particularly, an abrupt shift of core level peak position amounts to 0.60 eV within 4 Å HATCN nominal thickness was quantified, which indicates that a flat band condition is nearly established. For larger layer thickness, the core levels remain at constant energy. Note that the band bending values discussed in this study were determined directly from the I $3d_{5/2}$ core level shifts in order to have the highest surface sensitivity.

In order to access the general trend of the ELA between low-DoSS perovskites and electron acceptors, a different acceptor molecules, F6TCNNQ, with higher EA (ca. 5.6 eV[97]) was employed. The UPS and XPS spectra of the sequential deposition of F6TCNNQ molecules are displayed in **Figure 6.30**. Similar trend upon molecule deposition was observed for F6TCNNQ molecules, as shown in **Figure 6.30** (a) for the SECO spectra, Φ increases monotonically and saturates at a nominal thickness of 16 Å with a final value of 5.36 eV. During the same time, we observe the shifts of valence band towards lower BE,

accompanied with same shifts of core levels. As displayed in **Figure 6.30** (c) and (d) for Pb 4f and I $3d_{5/2}$ core levels, respectively, a reduction of 0.71 eV is quantified which corresponds to the change of surface band bending in perovskite substrate. The slightly larger $\Delta\Phi_{BB}$ in perovskite layer upon absorption of F6TCNNQ molecules relates to the higher EA as compared to that of HATCN molecules, which is likely to induce more electron transfer across the interface. Given the initial VB onset at 1.48 eV, such shift towards lower BE leads to a flat band condition and even slightly upward band bending may persist. Apart from the shifts of the valence and core level bands, additional features with the peak position at ca. 2.8 and ca. 1.5 eV BE upon F6TCNNQ deposition were observed. These DOS are attributed to the (relaxed) HOMO and partially filled LUMO levels, which are commonly seen from the charged molecules featuring a reduced bandgap because of Coulomb interaction due to additional charges.[4, 20] In addition, such

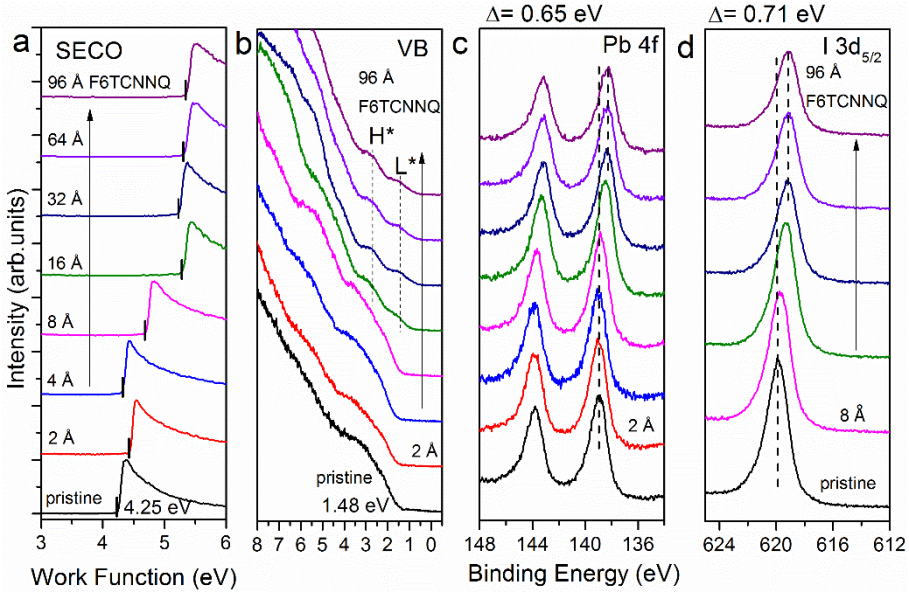

Figure 6.30 *a) SECO, b) VB and core level spectra of c) Pb 4f and d) I $3d_{5/2}$ as a function of incrementally deposited F6TCNNQ on pristine perovskite ($MAPbI_{3-x}Cl_x$) thin film. H^* and L^* indicate the relaxed HOMO and (partially) filled LUMO of F6TCNNQ molecules, respectively. The VBM of the pristine perovskite is determined to be at 1.48 eV. Figures are taken from [186].*

assignment leads to the energy gap of 1.3 eV which is consistent with the previous theoretical calculation as well as the experimental determined optical gap of F6TCNNQ anions.[20, 96]

6.5.2 High-DoSS perovskite/acceptor interfaces

a) High-DoSS of illuminated perovskite thin films

In order to investigate the dependence of the ELA on the initial DoSS on perovskite surface, similar photoemission experiments were further performed on illuminated perovskite substrates. To achieve high-DoSS, pristine perovskite films were firstly illuminated in UHV for 40 min. As we found from previous section, prolonged illumination treatment in UHV allows us to form substantial amount of high-DoSS, consisting mostly of metallic Pb (Pb^0) species, as shown in **Figure 6.31** (c) of Pb 4f core levels. Introducing of such large density of Pb^0, predominantly in the surface region (see angle-dependent XPS in **Figure 6.23**), causes strong Fermi level pinning at CBM, which results in further shift of VB onset and core levels by 0.2 eV towards high BE. Partial decomposition of perovskite upon prolonged illumination in UHV into PbI_2 species was noted in **Figure 6.25**, evident by the emergence of the absorption shoulder at ca. 500 nm. Nevertheless, the perovskite-

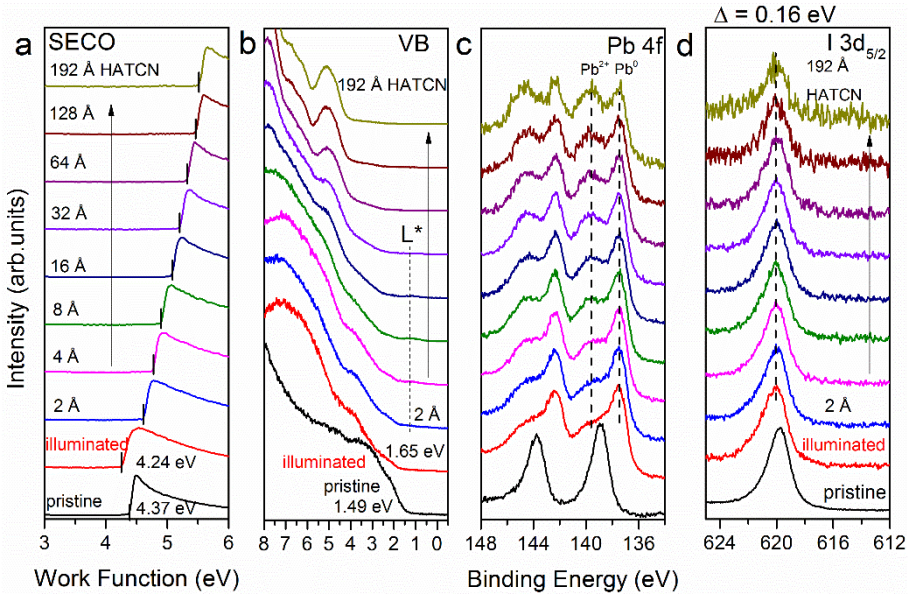

Figure 6.31 *a) SECO, b) VB and core level spectra of c) Pb 4f and d) I $3d_{5/2}$ as a function of incrementally deposited HATCN on illuminated perovskite ($MAPbI_{3-x}Cl_x$) thin film. L^* indicates the (partially) filled LUMO of HATCN molecules. The VBM of the pristine perovskite, determined at 1.49 eV, increases after illumination to 1.65 eV, showing a strong E_F pinning of the CBM. The strong low BE Pb 4f contribution is assigned to the emergence of Pb^0. Figures are taken from [186].*

related features, notably the optical absorption onset, persist.

In analogy to the changes in Φ upon HATCN and F6TCNNQ molecule adsorption, Φ increases from 4.24 eV to 5.51 eV (ΔΦ = 1.27 eV) for HATCN, and from 4.17 eV to 5.60 eV (ΔΦ = 1.43 eV) for F6TCNNQ, indicating electron transfer from the perovskite to the acceptor molecules, as presented in **Figure 6.31** (a) and **Figure 6.32** (a), respectively. In contrast to the results for low-DoSS perovskites, less change in band bending within high-DoSS perovskite substrates are found, which exhibit $\Delta\Phi_{BB}$ values of only 0.16 eV and 0.34 eV upon deposition of HATCN and F6TCNNQ, respectively. It can be clearly seen from the XPS measurements that upon molecule adsorption the Pb^0/Pb^{2+} ratio becomes strongly reduced, thus, the electron transfer occurs mainly from the metallic Pb surface states. Furthermore, the reduction of Pb^0 density indicates the fact that a control over the density of ionized donor-type surface states can be achieved by adsorption of electron acceptors, which might be useful for stabilizing interfaces in devices. We note that the larger $\Delta\Phi_{BB}$ as

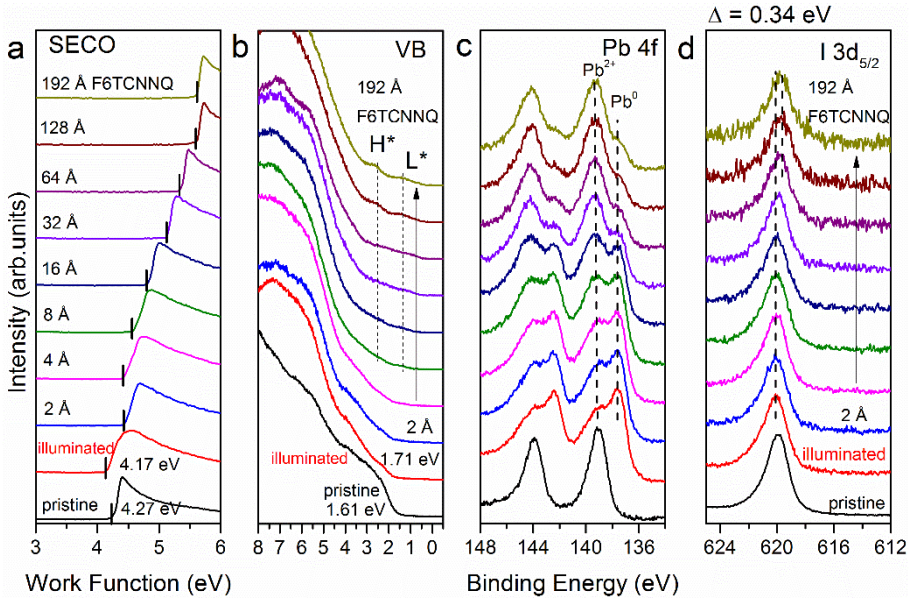

Figure 6.32 *a) SECO, b) VB and core level spectra of c) Pb 4f and d) I $3d_{5/2}$ as a function of incrementally deposited F6TCNNQ on illuminated perovskite ($MAPbI_{3-x}Cl_x$) thin film. H^* and L^* indicate the relaxed HOMO and (partially) filled LUMO of F6TCNNQ molecules, respectively. The VBM of the pristine perovskite is determined to be at 1.61 eV, which after illumination increases to 1.71 eV, again showing strong E_F pinning of the CBM. Figures are taken from [186].*

observed for F6TCNNQ molecules than that of the HATCN is attributed to the higher EA as compared to that of HATCN molecules, consistent with the larger reduction of Pb^0/Pb^{2+} ratio upon molecular adsorption.

b) High-DoSS of single crystal perovskite surfaces

In order further explore the influence of the surface DoSS, similar experiments were further conducted using single crystal perovskites ($MAPbI_3$). We observe, in contrast to the low defect density which is reported to account for the large charge diffusion length for

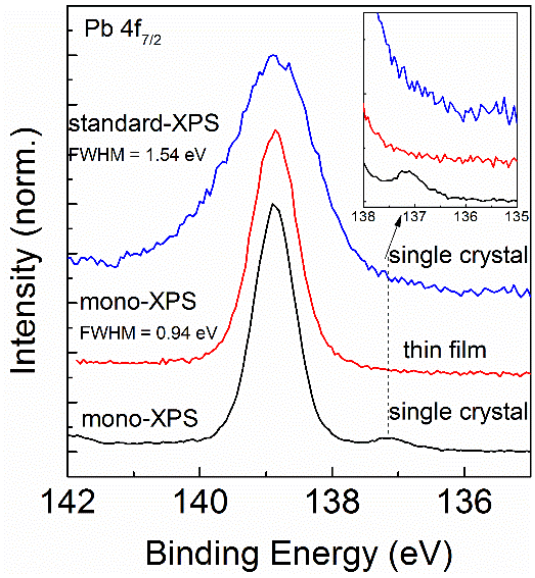

Figure 6.33 *High resolution core level spectra of $Pb4f_{7/2}$ acquired on a cleaved $MAPbI_3$ perovskite crystal and pristine thin films, together with standard XPS spectra of Pb $4f_{7/2}$ on single crystals. Inset: magnified core level spectra of Pb^0 region. Figure is taken from [186].*

single crystal perovskites,[25] that the single crystal surface exhibits relatively high-DoSS, possibly resulting from the cleaving process under inert atmosphere before introduction into the UHV system. This is clearly shown in **Figure 6.33** that although the single crystal surface does not seem to display Pb^0-reated defects under standard XPS measurements, however, high-resolution XPS spectra uncover the fact that already after cleaving the single crystal surface exhibits a relatively high density of Pb^0. Our finding agrees with the study by Yang et al.[167] that the density of surface defects is significantly higher for single crystal than for polycrystalline films.

Thickness-dependent UPS spectra of HATCN and F6TCNNQ molecules on freshly cleaved single crystal surfaces are displayed in **Figure 6.34** and **Figure 6.35**, respectively.

Upon molecular adsorption, Φ increases from 4.35 eV to 5.43 eV (ΔΦ = 1.08 eV) for HATCN, and from 4.24 eV to 4.80 eV (ΔΦ = 0.56 eV) for F6TCNNQ. We note that the small increase of Φ upon molecular absorption is due to the pronounced Volmer-Weber

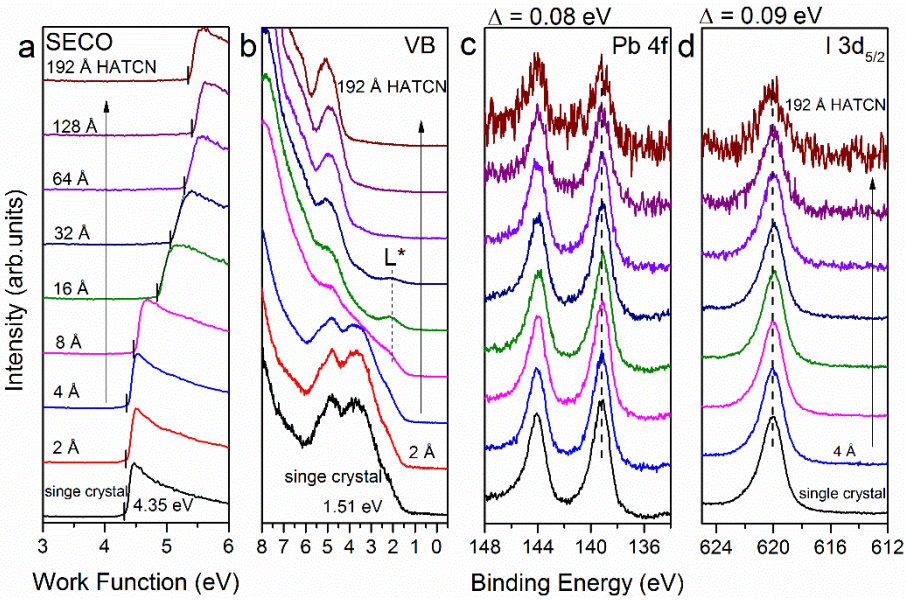

Figure 6.34 *a) SECO, b) VB and core level spectra of c) Pb 4f and d) I $3d_{5/2}$ as a function of incrementally deposited HATCN on freshly cleaved single crystal perovskite ($MAPbI_3$) surface. L^* indicates the (partially) filled LUMO of HATCN molecules. The VBM of the single crystal perovskite is at 1.51 eV. Figures are taken from [186].*

growth of these molecules on the large terraces present on single crystal surface as observed by atomic force microscopy (see Appendix 8.2.4), despite the large nominal layer thickness. This is consistent with the weak attenuation of perovskite core levels after F6TCNNQ deposition, as shown in **Figure 6.35** (c) and (d). Most importantly, the Pb 4f and I $3d_{5/2}$ core levels, similar to the results for high-DoSS perovskite films, exhibit only small shifts of ca. 0.10 eV for HATCN and ca. 0.27 eV for F6TCNNQ molecules.

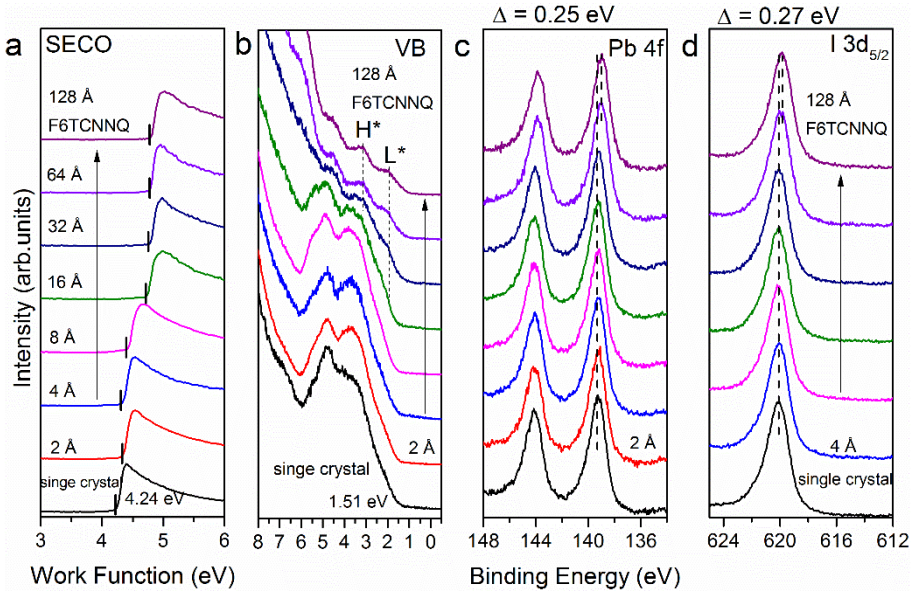

Figure 6.35 *a) SECO, b) VB and core level spectra of c) Pb 4f and d) I $3d_{5/2}$ as a function of incrementally deposited F6TCNNQ on freshly cleaved single crystal perovskite ($MAPbI_3$) surface. H^* and L^* indicate the relaxed HOMO and (partially) filled LUMO of F6TCNNQ molecules respectively. The VBM of the single crystal perovskite is at 1.51 eV. Figures are taken from [186].*

6.5.3 **Discussion and summary**

The established ELAs at perovskite/charge transport layer interfaces have shown large variations by several groups, which have not been rationalized so far. This underlines the fact that a general framework needs to be established, so that the different findings could be consistently explained and, more importantly, the understanding of the electronic properties at perovskite/charge transport layer interfaces could be enhanced. The present results clearly demonstrate that the ELAs between perovskite and functional layers are very much dependent on the perovskite surface DoSS, as illustrated in **Figure 6.36** where all determined $\Delta\Phi$ and $\Delta\Phi_{BB}$ values are summarized.

We can see from **Figure 6.36** that ΔΦ values, upon adsorption of HATCN and F6TCNNQ on both low- and high-DoSS perovskites, are overall similar (apart from the case of F6TCNNQ on the single crystal perovskite where the growth mode does not support full surface coverage, see AFM image in Appendix 8.2.4), importantly, $\Delta\Phi_{BB}$ for low-DoSS perovskite upon molecular deposition results in much higher value than those with high-DoSS perovskites. As estimated from $\Delta\Phi_{BB}$, when using low-DoSS surfaces the initially weakly E_F-pinned perovskite bands become eventually flattened in the surface region. Considering the initial downward surface band bending in the pristine perovskite samples, being induced by the donor-type Pb^0 surface states, we propose that the band flattening is a consequence of the reduction of the ionized DoSS as electrons are transferred from the surface states to the molecular acceptors. This proposition is further supported by the observed decrease in Pb^0 concentration when the acceptors are deposited onto the high-DoSS perovskite samples, as shown in Pb 4f core levels in **Figure 6.34** (c) for HATCN and **Figure 6.35** (c) for F6TCNNQ. In this case, due to the high-DoSS the CBM is very strongly

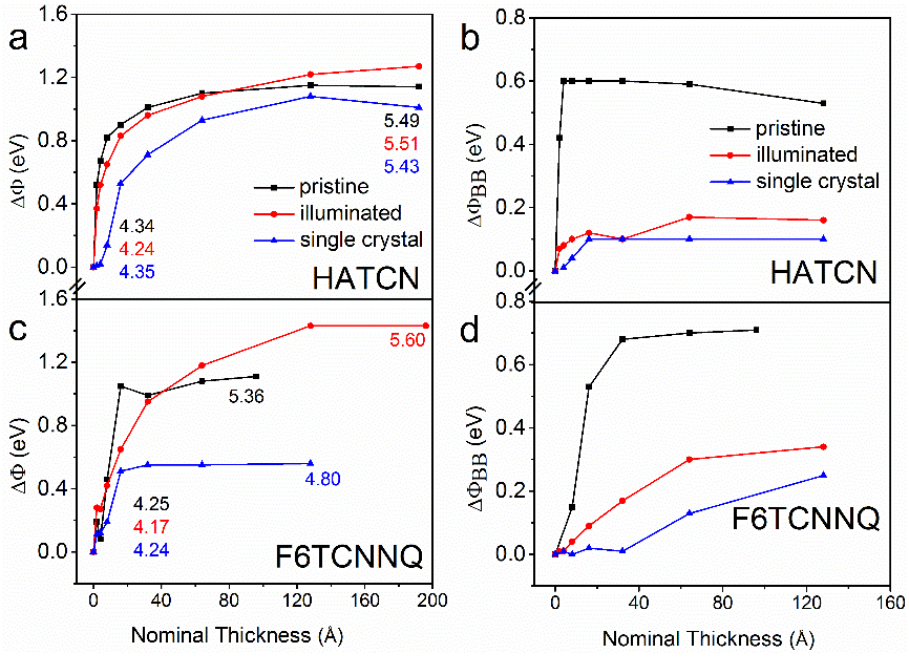

Figure 6.36 *a) and c) Evolution of work function change (ΔΦ) and b) and d) band-bending ($\Delta\Phi_{BB}$) as a function of HATCN (top) and F6TCNNQ (bottom) nominal thicknesses on pristine, single crystal and illuminated perovskites surfaces obtained from the above shown UPS and XPS results. Figures are taken from [186].*

pinned at E_F and only small $\Delta\Phi_{BB}$ values are observed. This interpretation is also consistent with the reported surface photovoltage effect, as discussed above in section 6.4, which initially occurs for pristine perovskite samples but becomes fully quenched upon prolonged white light illumination as a result of the generated high DoSS (primarily consisting of Pb^0 species).

The interfacial energy level diagrams, as a clear case of HATCN, for different perovskite surface DoSS are depicted in **Figure 6.37**. The influence of the back contact interface can be ruled out given the fact that the SPV effect readily occurs already under UV light with attenuation length of less than 20 nm, as a result, photo-generated charge carriers are expected to be only present in the surface region, giving no contribution to the buried interface. To further certify this point, XPS measurements in dark and under white light illumination were additionally performed on pristine perovskite thin film covered with 70 Å HATCN, as shown in **Figure 6.38**. Consistently, we see a shift of ca. 0.8 eV towards

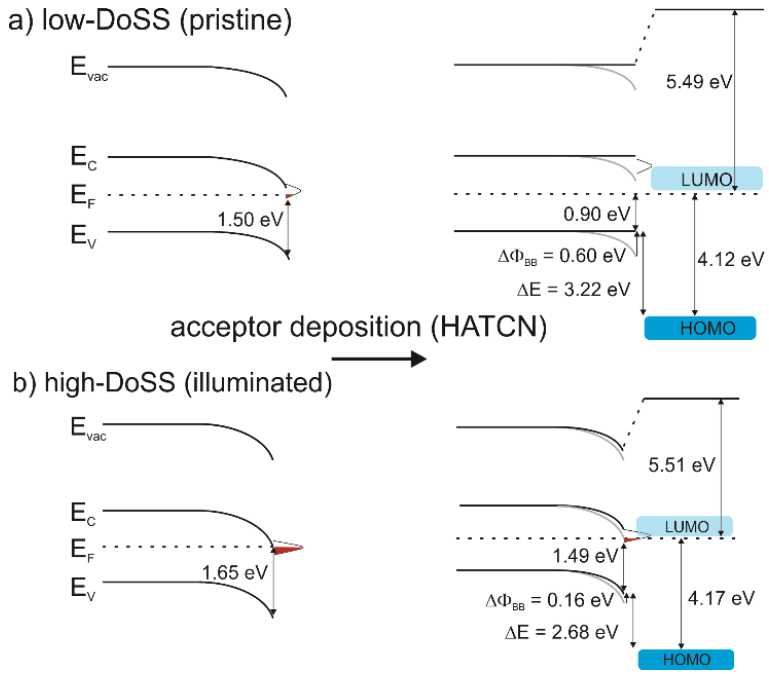

Figure 6.37 *Schematic energy level diagrams for the adsorption of HATCN acceptor on a) low and b) high-DoSS perovskite surfaces. The reduction in surface band-bending ($\Delta\Phi_{BB}$) by 0.60 eV for low-DoSS and by 0.16 eV for high-DoSS perovskite surfaces upon acceptor deposition is indicated. Red shades indicate the filled DoSS. Figures are taken from [186].*

lower BE for perovskite core levels upon HATCN deposition. Importantly, no energy shifts are observed when performing dark and light experiments, indicating that a flat band condition rather than upward band bending is reached in the perovskite film after molecular adsorption.

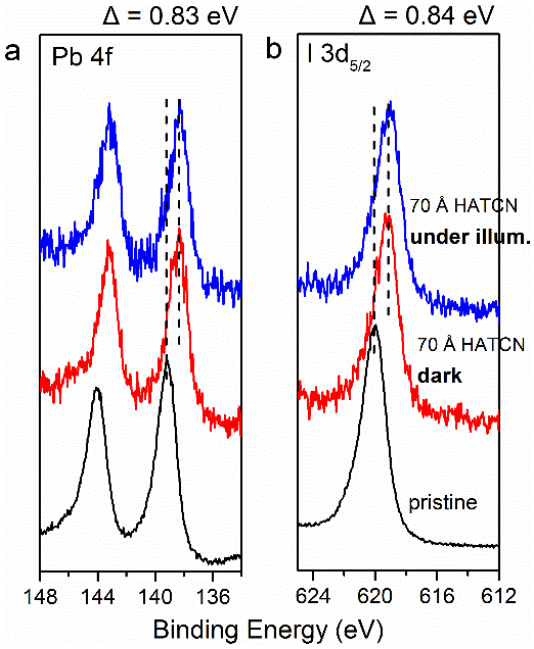

Figure 6.38 *Core level spectra of a) Pb 4f and b) I $3d_{5/2}$ of the pristine perovskite thin film and with 70 Å HATCN deposited on top. Pb 4f and I $3d_{5/2}$ core levels were acquired on 70 Å HATCN deposited perovskite surface in dark and under illumination (150 mW cm^{-2}), respectively. Figures are taken from [186].*

The depicted energy level diagrams in **Figure 6.37** for the case of HATCN clearly reveal the fact that different band bending scenarios within the perovskites are determined by the DoSS, which, depending on the present density, can result in large energy level offset variations. For instance, it can be seen from **Figure 6.37** that the energy offset between the VB onset and HOMO onset amounts to ~3.22 eV and ~2.68 eV when low- and high-DoSS perovskites are employed, respectively. This demonstrates that the interfacial energetics can be substantially modified by the perovskite surface DoSS, which in turn can pose tremendously impacts on the charge transfer process.

To summarize this section, we have investigated the impact of Pb^0-derived surface states on the interfacial ELA at perovskite/electron accepter heterojunctions. We have shown that the initial downward surface band bending for the pristine perovskite surface can be largely reduced upon adsorption of acceptor molecules. Depending on the present DoSS, different ELA scenarios are achieved and demonstrated. Large shifts by ca. 0.7 eV

towards mid-gap within pristine perovskites for low-DoSS surface are observed. In contrast, strong Fermi level pinning at CBM is induced by high-DoSS, such that strong n-type character on the surface still persists even after acceptor adsorption and concomitant electron transfer. Therefore, taking into account of the impact of DoSS, which can indeed vary considerably for different sample preparation conditions and subsequent treatments, should help explain the rather dissimilar energetics even for the nominally identical interfaces.

7 Summary and outlook

This thesis was devoted to a comprehensive understanding of the electronic structure of halide perovskites and their related interfaces. With PES as the core technique in this work, the dispersion of the frontier valence bands of single crystal perovskites was studied in great detail, providing a solid foundation for a deep insight into the optoelectronic properties of polycrystalline thin films. The surface electronic properties and the origin of the n-type behavior of different perovskite thin films were investigated by UPS and XPS measurements. The impact of surface states and their control over the energy level alignment were demonstrated. In addition, information on optical, chemical, structural, morphological properties of halide perovskite systems were obtained by combining UV-vis, X-ray diffraction, LEED and AFM measurements.

Single crystal perovskites were firstly employed in order to investigate the electronic band dispersions. We have demonstrated, by combining LEED and ARPES measurements, that the perovskite single crystals ($MAPbBr_3$ and $MAPbI_3$) exhibit strongly dispersive valence bands along the *X*-*M* and *X*-*R* directions at 300 K, with a bandwidth of 1.3 eV and 1.0 eV along the *X*-*R* direction for $MAPbBr_3$ and $MAPbI_3$, respectively, further supported by DFT calculation. LEED studies reveal that the (001) facet of cubic phase for both crystals was exposed upon cleaving. In contrast to the expectation of finding only the tetragonal phase at RT, the results obtained for the $MAPbI_3$ surface, however, demonstrate the coexistence of cubic and tetragonal phases already at RT. Only the former, which dominates the LEED pattern, is also observed in ARPES. The experimentally determined hole effective masses, which amount to ~0.25 m_0 for $MAPbBr_3$ and ~0.18 m_0 for $MAPbI_3$ crystals, are comparably low as that of their inorganic counterparts, e.g. Si[113] and/or GaAs.[7] We argued that the discrepancy between small effective mass and rather low

experimentally determined hole mobility suggests that the transport properties are not a result of bare carriers but, because of efficient Coulomb screening and soft lattices, resembling large polaron bands with potentially heavy masses.[9, 39, 109, 132, 181] While polaron formation certainly impacts charge transport, we do not observe polaronic effects in the band structure studies, owing to the fact that photoemission typically occurs on the fs time-scale, while large-polaron formation is expected to take place within ~10^2 fs.[132]

With a detailed knowledge on the electronic band structure, the issue of reliably determining valence band onset of perovskite thin films was further addressed. From the experimental single crystal band structure, the electronic spectra of polycrystalline thin films were reconstructed. We reveal that the comparably small contribution from the global VBM at *R* to area- and angle-averaged spectra compromises a straightforward valence band onset determination of HaPs. Similar to earlier suggestions,[34] using a logarithmic intensity scale to determine the VB onset is thus preferable, but all experimental parameters, such as instrumental limitations and sample gap-states, must still be carefully considered.

The above results uncovered the electronic band structure of single crystal perovskites and provided solid grounds towards a comprehensive understanding of the electronic properties of perovskite thin films. The surface electronic structure and its peculiarities of perovskite thin films were the focus of the third part. By characterizing the prototypical $MAPbI_3$ thin films using UPS, surface band bending was found to account for the n-type behavior of perovskite films often observed from photoemission measurements. This is demonstrated by the occurrence of SPV, from which a shift by ca. 0.5 eV in energy levels solely from UPS measurements is obtained. Supported by KP measurements in dark and under illumination, all samples exhibit excitation-intensity dependent energy levels, leading to shifts by up to 0.7 eV under additional illumination from UPS measurements. XPS measurements on perovskite films conclude that the presence of donor-type surface states, possible consisting of metallic Pb, is the origin of downward band bending on perovskite surface. Furthermore, degradation into PbI_2 and elemental Pb due to prolonged white light illumination in UHV condition is found to take place in perovskite material. The

resulting metallic Pb can in turn lead to strong Fermi level pinning at CBM, which quenches the SPV effect. The results suggest that SPV must be certainly taken into account when characterizing hybrid perovskite samples where optical excitation is inevitably employed.

Finally, the presence of surface states was found to not only modify the electronic energy levels on perovskite surface, but also control over the energy level alignment when forming interfaces with transport layers. By employing electron acceptor molecules, the impact of Pb^0-derived surface states on the interfacial ELA at perovskite/electron accepter heterojunctions was investigated. We have shown that the initial downward surface band bending for the pristine perovskite surface can be largely reduced upon adsorption of acceptor molecules. Depending on the present DoSS, different ELA scenarios are achieved and demonstrated. Large shifts by ca. 0.7 eV in energy levels towards mid-gap within pristine perovskite (low-DoSS) surface are observed. In contrast, strong Fermi level pinning at CBM is induced by high-DoSS, such that strong n-type character on the surface still persists even after acceptor adsorption and concomitant electron transfer. Therefore, taking into account of the impact of DoSS, which can indeed vary considerably for different sample preparation conditions and subsequent treatments, should help explain the rather dissimilar energetics even for the nominally identical interfaces.

The above results in this thesis help contribute to a better understanding of the electronic properties of perovskite systems, however, many fundamental questions still remain. The key one is the impact of structural dynamic on the electronic structure, optical and electrical properties. It would therefore be very important to perform investigations on the halide perovskites at different time- and length-scales.

8 Appendix

8.1 Excitation source parameters

Table A1. Main satellite contributions (intensity and photon energy) of the helium discharge lamp.

Satellite	Relative intensity (%)	Photon energy (eV)
He I_β	2-5	23.09
He I_γ	0.5-0.8	23.74
He II_β	< 10	48.37
He II_γ	/	51.02

Table A2. Main satellite contributions (relative intensity and relative energy with respect to **K**$\alpha_{1,2}$) of the X-ray excitation sources. Mg **K**$\alpha_{1,2}$ = 1253.6 eV, Al **K**$\alpha_{1,2}$ = 1486.6 eV. Parameters are taken from [91].

	Relative energy shift (eV)		**Relative intensity (%)**	
K line	**Mg**	**Al**	**Mg**	**Al**
α_3	8.5	9.7	9.1	7.3
α_4	10.1	11.7	5.1	3.1

8.2 Additional experimental data

8.2.1 **Density functional theory**

DFT calculations were performed using the VASP plane-wave code,[81] using the

HSE exchange-correlations functional[55-56] including spin-orbit coupling, and 'normal' PAW potentials (treating the *5d* electrons of Pb explicitly) with a plane-wave kinetic energy cutoff of 400 eV. To allow for interpretation of the experimental data despite the remaining deficiencies of our theoretical approach, we performed an *a posteriori* correction by "stretching" the eigenvalue spectrum according to the values reported in our previous study.[34] Cubic unit-cells of $MAPbI_3$ and $MAPbBr_3$ with previously calculated lattice constants[32] and a 4x4x4 Γ-centered *k*-point grid were used for self-consistently calculating the charge-density. Subsequent band-structure calculations were performed non-self-consistently using an equally–spaced *k*-grid of 50 points between the high-symmetry points of the Brillouin zone.

8.2.2 **Determining the valence band onset of halide perovskites**

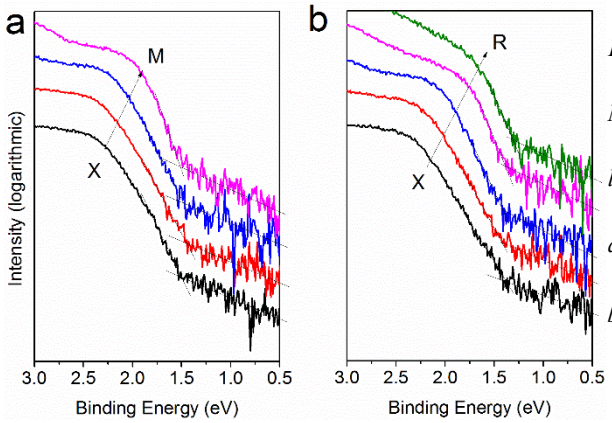

Figure 8.1 *Energy distribution curves (EDCs) of $MAPbI_3$ single crystal from* ***Figure 6.11*** *in semi-log plots for selected k-values along the (a) X-M and (b) X-R directions. Figures are taken from [185].*

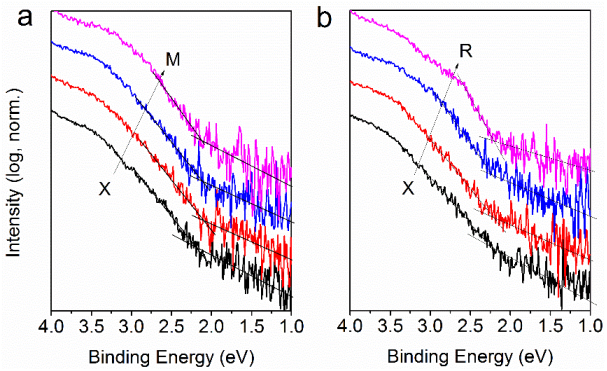

Figure 8.2 *Energy distribution curves (EDCs) of $MAPbBr_3$ single crystal from* ***Figure 6.5*** *in semi-log plots for selected k-values along the (a) X-M and (b) X-R directions. Figures are taken from [185].*

8.2.3 **Surface electronic properties of halide perovskite thin films**

Figure 8.3 shows UPS spectra of the $MAPbI_{3-x}Cl_x$ thin films measured at multiple on-off illumination cycles. The work function and VB onset values, as summarized **Figure 6.20** (b), become fixed after first illumination cycle, indicating a strong Fermi level pinning at CBM.

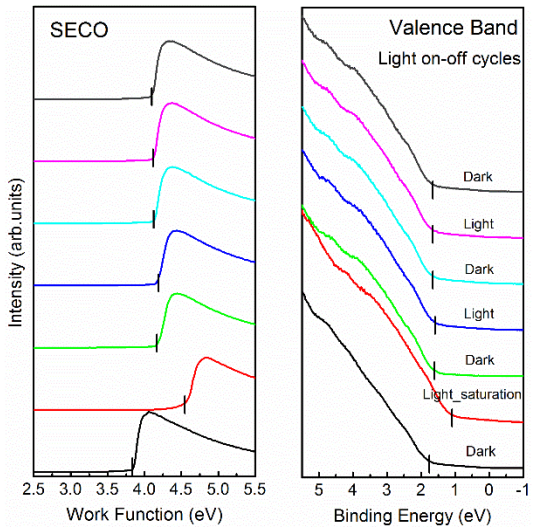

Figure 8.3 *The series of UPS measurements of the perovskite film illuminated at an intensity of 67 mW cm^{-2} over multiple on-off cycles. Figures are taken from [184].*

Figure 8.4 shows UPS spectra of the perovskite film, which was measured over multiple

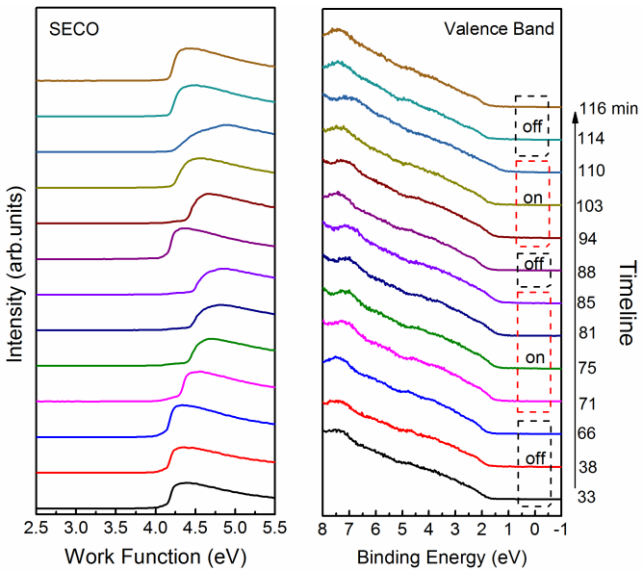

Figure 8.4 *The series of UPS measurements of the perovskite film illuminated at an intensity of 154 mW/cm² over multiple on-off illumination cycles. Figures are taken from [184].*

illumination cycles with constant power intensity at 154 mW/cm^2. The work function and VB onset values are summarized in **Figure 6.21**.

The UPS spectra as a function of excitation-intensity are shown in **Figure 8.5** for FAMA thin film, **Figure 8.6** for CsFAMA thin film and **Figure 8.7** for RbCsFAMA thin film. We note that, for mixed perovskite samples, the top valence band structure exhibits globally very similar electronic structure, which can be understood since the cations do not contribute directly to the frontier bands.[14, 169]

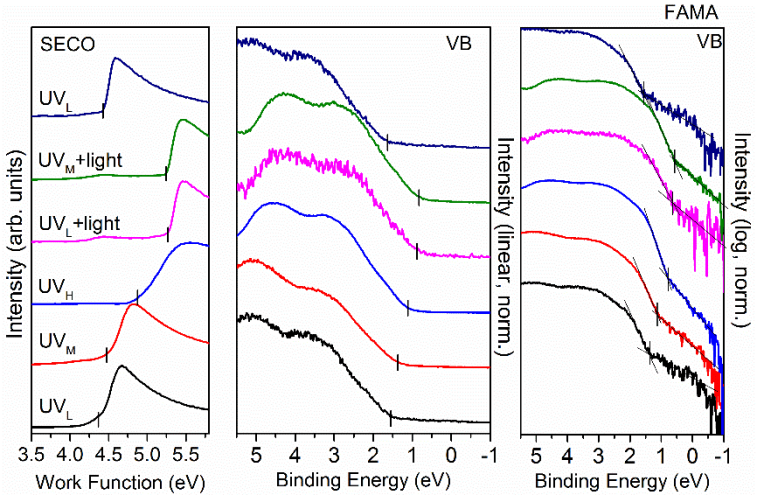

Figure 8.5 *UPS spectra of FAMA thin films measured with varied incident UV flux and additional white light illumination (150 mW/cm²). VB in linear and logarithmic intensity scale are presented in middle and right panels, respectively.*

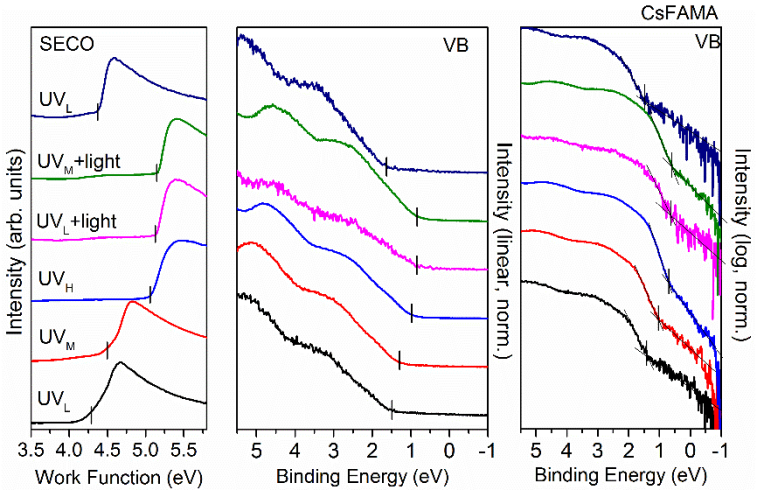

Figure 8.6 *UPS spectra of CsFAMA thin films measured with varied incident UV flux and additional white light illumination (150 mW/cm^2). VB in linear and logarithmic intensity scale are presented in middle and right panels, respectively.*

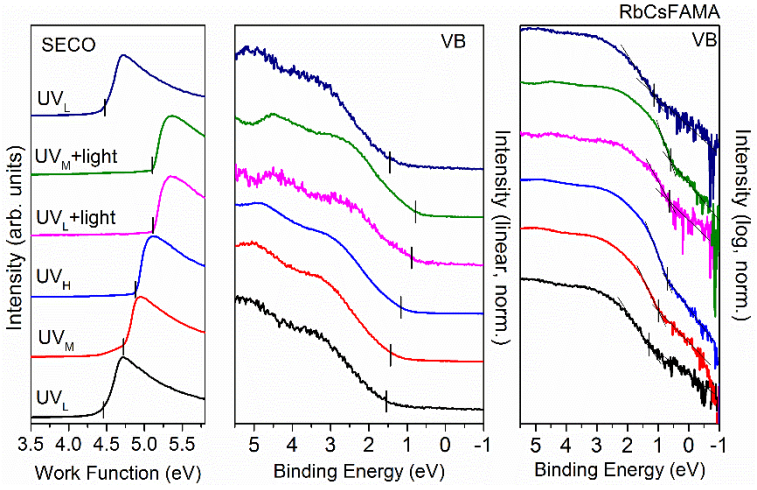

Figure 8.7 *UPS spectra of RbCsFAMA thin films measured with varied incident UV flux and additional white light illumination (150 mW/cm^2). VB in linear and logarithmic intensity scale are presented in middle and right panels, respectively.*

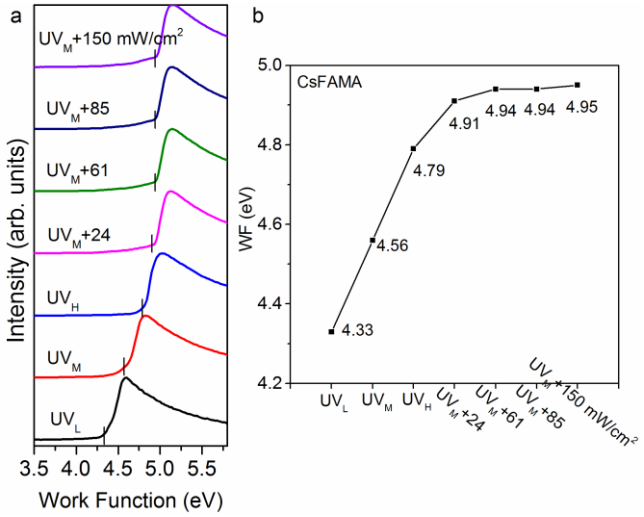

Figure 8.8 *(a) SECO spectra of a CsFAMA perovskite thin film as a function of excitation intensity. (b) summarized work function values at varied illumination intensity from (a).*

8.2.4 **Energy levels alignment at halide perovskite/electron acceptors interfaces**

Absorption spectra of the pristine and illuminated perovskite films are shown in **Figure 8.9**. We note that perovskite features to a large extent retain the same. Although it is seen that the intensity of the perovskite absorption onset decreases after illumination treatment, it remains virtually observable.

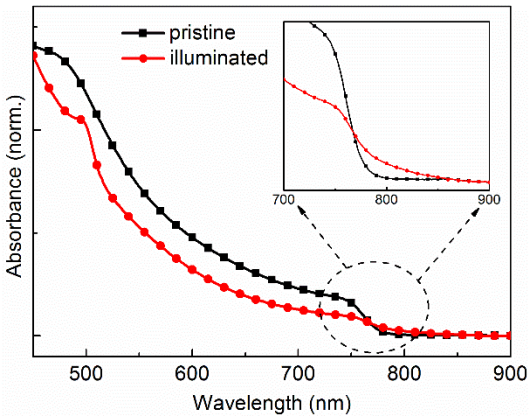

Figure 8.9 *UV-vis absorption spectra of a pristine (■) and illuminated (●) perovskite films. Inset: magnified absorbance region at absorption onset. Figure is taken from [186].*

The surface morphology of the pristine, illuminated and single crystal perovskites before molecular deposition are shown in **Figure 8.10** (a), (b) and (c), respectively. Adsorption of HATCN and F6TCNNQ molecules on the surfaces are shown

correspondingly in the middle [**Figure 8.10** (d), (e) and (f), respectively] and on the bottom [**Figure 8.10** (g), (h) and (i), respectively]. It can be seen that F6TCNNQ deposition on pristine perovskite surface exhibits large islands aggregates. Extremely pronounced island growth mode can be found on single crystal surface, as a consequence, it results in low surface coverage of F6TCNNQ molecules. However, deposition of HATCN does not result in clear distribution of the molecules, which might indicate a preferred lay-by-layer growth mode on different perovskite surfaces. It is also noted that the topographic features of illuminated perovskite surface have been largely modified by illumination treatment in UHV condition, which results in small crystallites.

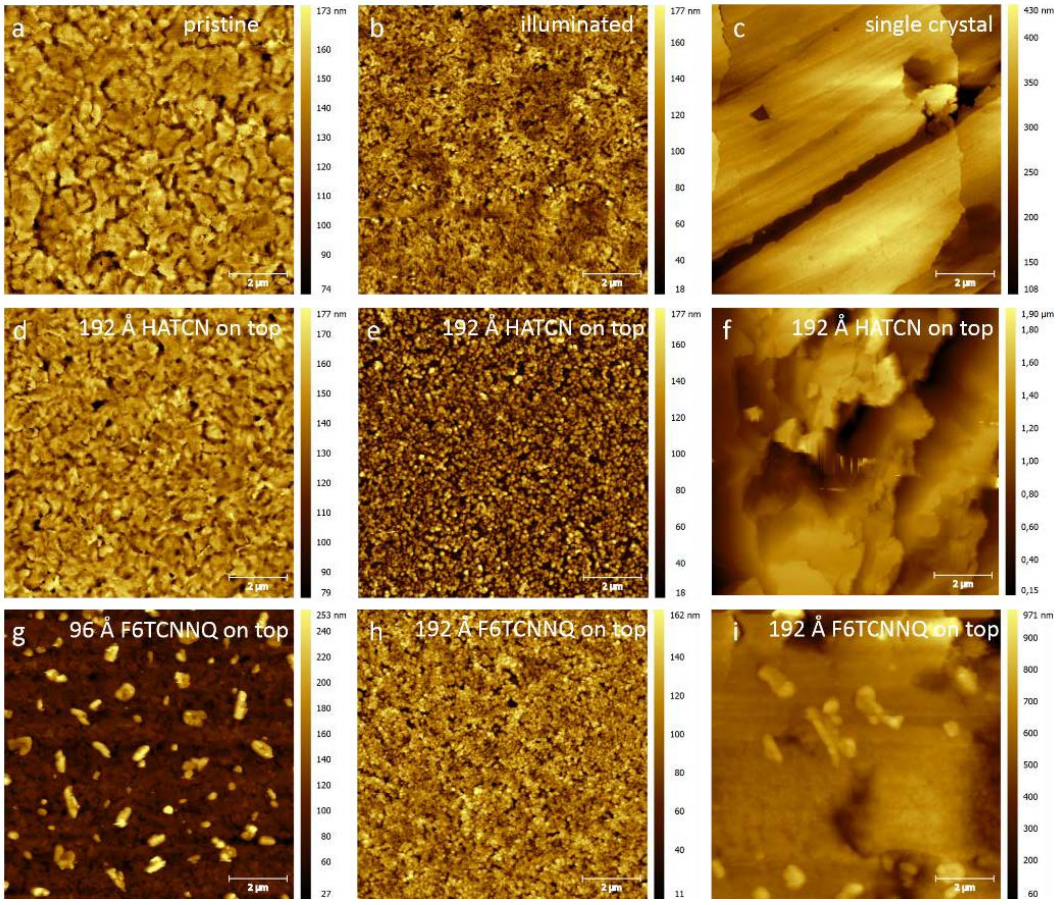

Figure 8.10 *AFM morphology of a) the pristine, b) illuminated and c) single crystal perovskite surfaces before and after absorption of d), e) and f) 192 Å HATCN, and g) 96 Å, h) 192 Å and i) 192 Å F6TCNNQ molecules on top of the corresponding samples. Figures are taken from [186].*

These results are consistent with the photoemission measurements, which, due to the high surface sensitivity (~1-2 nm) of the technique, reveal that the HATCN film fully covers the substrates as the perovskite valence features are strongly quenched upon adsorption. In contrast, strong photoemission features from the perovskites remain visible for F6TCNNQ even for the nominally thickest films.

Bibliography

[1] http://www.specs.de/cms/upload/PDFs/UV/SPECS_Brochure_UV-Source-Series.pdf.
[2] Abdelmageed, G., et al. Mechanisms for light induced degradation in MAPbI3 perovskite thin films and solar cells. *Applied Physics Letters* **2016,** *109*, 233905.
[3] Alonso, M., et al. Surface photovoltage effects in photoemission from metal-gap(110) interfaces: Importance for band bending evaluation. *Physical Review Letters* **1990,** *64*, 1947.
[4] Amsalem, P., et al. Role of charge transfer, dipole-dipole interactions, and electrostatics in fermi-level pinning at a molecular heterojunction on a metal surface. *Physical Review B* **2013,** *87*, 035440.
[5] Andrade, J. D. *X-ray photoelectron spectroscopy (xps): Surface and interfacial aspects of biomedical polymers*, Springer: 1985.
[6] Bi, D., et al. Polymer-templated nucleation and crystal growth of perovskite films for solar cells with efficiency greater than 21%. *Nature Energy* **2016,** *1*, 16142.
[7] Blakemore, J. S. Semiconducting and other major properties of gallium arsenide. *Journal of Applied Physics* **1982,** *53*, R123.
[8] Bocquet, F. C., et al. Final-state diffraction effects in angle-resolved photoemission at an organic-metal interface. *Physical Review B* **2011,** *84*.
[9] Bonn, M., et al. Role of dielectric drag in polaron mobility in lead halide perovskites. *ACS Energy Letters* **2017,** *2*, 2555.
[10] Braun, J. The theory of angle-resolved ultraviolet photoemission and its applications to ordered materials. *Reports on Progress in Physics* **1996,** *59*, 1267.
[11] Braun, S., et al. Energy-level alignment at organic/metal and organic/organic interfaces. *Advanced Materials* **2009,** *21*, 1450.
[12] Brenner, T. M., et al. Hybrid organic—inorganic perovskites: Low-cost semiconductors with intriguing charge-transport properties. *Nature Reviews Materials* **2016,** *1*, 15007.
[13] Brenner, T. M., et al. Are mobilities in hybrid organic-inorganic halide perovskites actually "high"? *The Journal of Physical Chemistry Letters* **2015,** *6*, 4754.
[14] Brivio, F., et al. Relativistic quasiparticle self-consistent electronic structure of hybrid halide perovskite photovoltaic absorbers. *Physical Review B* **2014,** *89*.
[15] Brucker, C. F. Electron spectroscopy: Theory, techniques and applications. *Surface and Interface Analysis* **1982,** *4*, i.
[16] Burschka, J., et al. Sequential deposition as a route to high-performance perovskite-sensitized solar cells. *Nature* **2013,** *499*, 316.
[17] Bussolotti, F., et al. Hole-phonon coupling effect on the band dispersion of organic molecular semiconductors. *Nature Communications* **2017,** *8*, 173.

[18] Cappella, B.; Dietler, G. Force-distance curves by atomic force microscopy. *Surface Science Reports* **1999,** *34*, 1.
[19] Chen, Q., et al. Planar heterojunction perovskite solar cells via vapor-assisted solution process. *Journal of the American Chemical Society* **2014,** *136*, 622.
[20] Christodoulou, C., et al. Tuning the electronic structure of graphene by molecular dopants: Impact of the substrate. *ACS Applied Materials & Interfaces* **2015,** *7*, 19134.
[21] Conings, B., et al. Perovskite-based hybrid solar cells exceeding 10% efficiency with high reproducibility using a thin film sandwich approach. *Advanced Materials* **2014,** *26*, 2041.
[22] De Wolf, S., et al. Organometallic halide perovskites: Sharp optical absorption edge and its relation to photovoltaic performance. *The Journal of Physical Chemistry Letters* **2014,** *5*, 1035.
[23] deQuilettes, D. W., et al. Photo-induced halide redistribution in organic-inorganic perovskite films. *Nature Communications* **2016,** *7*, 11683.
[24] Docampo, P., et al. Efficient organometal trihalide perovskite planar-heterojunction solar cells on flexible polymer substrates. *Nature Communications* **2013,** *4*, 2761.
[25] Dong, Q., et al. Electron-hole diffusion lengths > 175 μm in solution-grown CH3NH3PbI3 single crystals. *Science* **2015,** *347*, 967.
[26] Dou, L., et al. Atomically thin two-dimensional organic-inorganic hybrid perovskites. *Science* **2015,** *349*, 1518.
[27] Dou, L., et al. Solution-processed hybrid perovskite photodetectors with high detectivity. *Nature Communications* **2014,** *5*, 5404.
[28] Douglas A. Skoog, F. J. H., Stanley R. Crouch. *Principles of instrumental analysis*, Cengage Learning: 2017.
[29] Du, M.-H. Density functional calculations of native defects in ch3nh3pbi3: Effects of spin–orbit coupling and self-interaction error. *The Journal of Physical Chemistry Letters* **2015,** *6*, 1461.
[30] Du, M. H. Efficient carrier transport in halide perovskites: Theoretical perspectives. *Journal of Materials Chemistry A* **2014,** *2*, 9091.
[31] Duan, H. S., et al. The identification and characterization of defect states in hybrid organic-inorganic perovskite photovoltaics. *Physical Chemistry Chemical Physics* **2015,** *17*, 112.
[32] Egger, D. A.; Kronik, L. Role of dispersive interactions in determining structural properties of organic–inorganic halide perovskites: Insights from first-principles calculations. *The Journal of Physical Chemistry Letters* **2014,** *5*, 2728.
[33] Emara, J., et al. Impact of film stoichiometry on the ionization energy and electronic structure of CH3NH3PbI3 perovskites. *Advanced Materials* **2016,** *28*, 553.
[34] Endres, J., et al. Valence and conduction band densities of states of metal halide perovskites: A combined experimental–theoretical study. *The Journal of Physical Chemistry Letters* **2016,** *7*, 2722.
[35] Eperon, G. E., et al. Morphological control for high performance, solution-processed planar heterojunction perovskite solar cells. *Advanced Functional Materials* **2014,** *24*, 151.

[36] Even, J., et al. Importance of spin–orbit coupling in hybrid organic/inorganic perovskites for photovoltaic applications. *The Journal of Physical Chemistry Letters* **2013,** *4*, 2999.
[37] Even, J., et al. Solid-state physics perspective on hybrid perovskite semiconductors. *The Journal of Physical Chemistry C* **2015,** *119*, 10161.
[38] Fröhlich, H.; Sewell, G. L. Electric conduction in semiconductors. *Proceedings of the Physical Society* **1959,** *74*, 643.
[39] Frost, J. M. Calculating polaron mobility in halide perovskites. *Physical Review B* **2017,** *96*, 195202
[40] Frost, J. M., et al. Atomistic origins of high-performance in hybrid halide perovskite solar cells. *Nano Letters* **2014,** *14*, 2584.
[41] Galkowski, K., et al. Determination of the exciton binding energy and effective masses for methylammonium and formamidinium lead tri-halide perovskite semiconductors. *Energy & Environmental Science* **2016,** *9*, 962.
[42] Gao, W., et al. Quasiparticle band gap of organic-inorganic hybrid perovskites: Crystal structure, spin-orbit coupling, and self-energy effects. *Physical Review B* **2016,** *93*, 085202.
[43] Gelius, U. Binding energies and chemical shifts in esca. *Physica Scripta* **1974,** *9*, 133.
[44] Gelius, U., et al. A high resolution esca instrument with x-ray monochromator for gases and solids. *Journal of Electron Spectroscopy and Related Phenomena* **1973,** *2*, 405.
[45] Giovanelli, L., et al. Interpretation of valence band photoemission spectra at organic-metal interfaces. *Physical Review B* **2013,** *87*.
[46] Goldschmidt, V. M. Die gesetze der krystallochemie. *Naturwissenschaften* **1926,** *14*, 477.
[47] Green, M. A., et al. Optical properties of photovoltaic organic–inorganic lead halide perovskites. *The Journal of Physical Chemistry Letters* **2015,** *6*, 4774.
[48] Guittet, M. J., et al. Bonding and xps chemical shifts in zrsio4 versus sio2 and zro2:Charge transfer and electrostatic effects. *Physical Review B* **2001,** *63*, 125117.
[49] He, Y.; Galli, G. Perovskites for solar thermoelectric applications: A first principle study of CH3NH3aI3 (a = Pb and Sn). *Chemistry of Materials* **2014,** *26*, 5394.
[50] Hecht, M. H. Role of photocurrent in low-temperature photoemission studies of schottky-barrier formation. *Physical Review B* **1990,** *41*, 7918.
[51] Hedin, L.; Lundqvist, S. *Effects of electron-electron and electron-phonon interactions on the one-electron states of solids*, Academic Press: 1970.
[52] Heinhold, R., et al. Influence of polarity and hydroxyl termination on the band bending at zno surfaces. *Physical Review B* **2013,** *88*.
[53] Heo, J. H., et al. Efficient inorganic-organic hybrid heterojunction solar cells containing perovskite compound and polymeric hole conductors. *Nature Photonics* **2013,** *7*, 486.
[54] Herz, L. M. Charge-carrier mobilities in metal halide perovskites: Fundamental mechanisms and limits. *ACS Energy Letters* **2017,** *2*, 1539.
[55] Heyd, J., et al. Hybrid functionals based on a screened coulomb potential. *The Journal of Chemical Physics* **2003,** *118*, 8207.

[56] Heyd, J., et al. Hybrid functionals based on a screened coulomb potential. *The Journal of Chemical Physics* **2006,** *124*, 219906.
[57] Hill, I. G., et al. Molecular level alignment at organic semiconductor-metal interfaces. *Applied Physics Letters* **1998,** *73*, 662.
[58] Hofmann, P. *Solid state physics: An introduction*, Wiley-VCH Verlag GmbH & Co.: 2015.
[59] https://www.nrel.gov/pv/assets/pdfs/cell_efficiency_explanatory_notes.pdf.
[60] Hüfner, S. *Photoelectron spectroscopy: Principles and applications*, Springer: 2003.
[61] Hwang, J., et al. Energetics of metal–organic interfaces: New experiments and assessment of the field. *Materials Science and Engineering: R: Reports* **2009,** *64*, 1.
[62] Ibach, H.; Lüth, H. *Solid-state physics: An introduction to principles of materials science*, Springer-Verlag Berlin Heidelberg: 2009.
[63] Im, J.-H., et al. 6.5% efficient perovskite quantum-dot-sensitized solar cell. *Nanoscale* **2011,** *3*, 4088.
[64] Ishii, H., et al. Energy level alignment and interfacial electronic structures at organic/metal and organic/organic interfaces. *Advanced Materials* **1999,** *11*, 605.
[65] John F. Moulder, W. F. S., Peter E. Sobol, Kenneth D. Bomben. *Handbook of x-ray photoelectron spectroscopy : A reference book of standard spectra for identification and interpretation of xps data*, Perkin-Elmer Corporation 1992.
[66] Johnson, E. O. Large-signal surface photovoltage studies with germanium. *Physical Review* **1958,** *111*, 153.
[67] Juarez-Perez, E. J., et al. Photoinduced giant dielectric constant in lead halide perovskite solar cells. *The Journal of Physical Chemistry Letters* **2014,** *5*, 2390.
[68] Kahn, A., et al. Electronic structure and electrical properties of interfaces between metals and π-conjugated molecular films. *Journal of Polymer Science Part B: Polymer Physics* **2003,** *41*, 2529.
[69] Karakus, M., et al. Phonon-electron scattering limits free charge mobility in methylammonium lead iodide perovskites. *The Journal of Physical Chemistry Letters* **2015,** *6*, 4991.
[70] Kelvin, L. *Philosophical Magazine* **1898,** *46*.
[71] Kim, H.-S., et al. Lead iodide perovskite sensitized all-solid-state submicron thin film mesoscopic solar cell with efficiency exceeding 9%. *Scientific Reports* **2012,** *2*, 591.
[72] Kim, J., et al. The role of intrinsic defects in methylammonium lead iodide perovskite. *The Journal of Physical Chemistry Letters* **2014,** *5*, 1312.
[73] Kim, T. W., et al. Self-organized superlattice and phase coexistence inside thin film organometal halide perovskite. *Advanced Materials* **2018,** *30*, 1705230.
[74] Kittel, C., Introduction to solid state physics John Wiley & Sons: 2005.
[75] Koch, N. Organic electronic devices and their functional interfaces. *Chemphyschem* **2007,** *8*, 1438.
[76] Koch, N., et al. *The molecule-metal interface*, Wiley-VCH: 2013.
[77] Koch, N., et al. Evidence for temperature-dependent electron band dispersion in pentacene. *Physical Review Letters* **2006,** *96*, 156803.

[78] Kojima, A., et al. Organometal halide perovskites as visible-light sensitizers for photovoltaic cells. *Journal of the American Chemical Society* **2009,** *131*, 6050.
[79] Komesu, T., et al. Surface electronic structure of hybrid organo lead bromide perovskite single crystals. *The Journal of Physical Chemistry C* **2016,** *120*, 21710.
[80] Kraut, E. A., et al. Precise determination of the valence-band edge in x-ray photoemission spectra: Application to measurement of semiconductor interface potentials. *Physical Review Letters* **1980,** *44*, 1620.
[81] Kresse, G.; Furthmüller, J. Efficient iterative schemes for ab initio total-energy calculations using a plane-wave basis set. *Physical Review B* **1996,** *54*, 11169.
[82] Kronik, L.; Shapira, Y. Surface photovoltage phenomena: Theory, experiment, and applications. *Surface Science Reports* **1999,** *37*, 1.
[83] Lee, M. M., et al. Efficient hybrid solar cells based on meso-superstructured organometal halide perovskites. *Science* **2012,** *338*, 643.
[84] Lee, S., et al. Determination of the interface energy level alignment of a doped organic hetero-junction using capacitance–voltage measurements. *Organic Electronics* **2012,** *13*, 2346.
[85] Ley, M. C. *Photoemission in solids i: General principles*, Springer: 1978.
[86] Li, C., et al. Halide-substituted electronic properties of organometal halide perovskite films: Direct and inverse photoemission studies. *ACS Applied Materials & Interfaces* **2016,** *8*, 11526.
[87] Li, X., et al. A vacuum flash–assisted solution process for high-efficiency large-area perovskite solar cells. *Science* **2016,** *353*, 58.
[88] Liang, P.-W., et al. Additive enhanced crystallization of solution-processed perovskite for highly efficient planar-heterojunction solar cells. *Advanced Materials* **2014,** *26*, 3748.
[89] Liu, M., et al. Efficient planar heterojunction perovskite solar cells by vapour deposition. *Nature* **2013,** *501*, 395.
[90] Liu, Y., et al. Two-inch-sized perovskite CH3NH3PbX3 (X = Cl, Br, I) crystals: Growth and characterization. *Advanced Materials* **2015,** *27*, 5176.
[91] M O Krause; Ferreira, J. G. K x-ray emission spectra of mg and al. *Journal of Physics B: Atomic and Molecular Physics* **1975,** *8*, 2007.
[92] Machida, S.-i., et al. Highest-occupied-molecular-orbital band dispersion of rubrene single crystals as observed by angle-resolved ultraviolet photoelectron spectroscopy. *Physical Review Letters* **2010,** *104*, 156401.
[93] Machida, S., et al. Highest-occupied-molecular-orbital band dispersion of rubrene single crystals as observed by angle-resolved ultraviolet photoelectron spectroscopy. *Physical Review Letters* **2010,** *104*, 156401.
[94] Mark R Deakin; Buttry, D. A. Electrochemical applications of the quartz crystal microbalance. *Analytical Chemistry* **1989,** *61*, 1147A.
[95] McMeekin, D. P., et al. A mixed-cation lead mixed-halide perovskite absorber for tandem solar cells. *Science* **2016,** *351*, 151.
[96] Méndez, H., et al. Doping of organic semiconductors: Impact of dopant strength and electronic coupling. *Angewandte Chemie International Edition* **2013,** *52*, 7751.

[97] Mendez, H., et al. Charge-transfer crystallites as molecular electrical dopants. *Nature Communications* **2015,** *6*, 8560.
[98] Menéndez-Proupin, E., et al. Self-consistent relativistic band structure of the CH3NH3PbI3 perovskite. *Physical Review B* **2014,** *90*, 045207.
[99] Meyer, J., et al. Transition metal oxides for organic electronics: Energetics, device physics and applications. *Advanced Materials* **2012,** *24*, 5408.
[100] Michel A. VanHove, W. H. W., Chi-Ming Chan. *Low-energy electron diffraction: Experiment, theory and surface structure determination*, Springer-Verlag Berlin Heidelberg: 1986.
[101] Miller, E. M., et al. Substrate-controlled band positions in CH3NH3PbI3 perovskite films. *Physical Chemistry Chemical Physics* **2014,** *16*, 22122.
[102] Misra, R. K., et al. Temperature- and component-dependent degradation of perovskite photovoltaic materials under concentrated sunlight. *The Journal of Physical Chemistry Letters* **2015,** *6*, 326.
[103] Miyata, A., et al. Direct measurement of the exciton binding energy and effective masses for charge carriers in organic–inorganic tri-halide perovskites. *Nature Physics* **2015,** *11*, 582.
[104] Mom, R. V., et al. Leed analysis of a nickel cylindrical single crystal. *Surface Science* **2013,** *613*, 15.
[105] Mönch, W. *Semiconductor surfaces and interfaces*, Springer: 1993.
[106] Mosconi, E., et al. Light-induced annihilation of frenkel defects in organo-lead halide perovskites. *Energy & Environmental Science* **2016,** *9*, 3180.
[107] Moser, S. An experimentalist's guide to the matrix element in angle resolved photoemission. *Journal of Electron Spectroscopy and Related Phenomena* **2017,** *214*, 29.
[108] Motta, C., et al. Revealing the role of organic cations in hybrid halide perovskite CH3NH3PbI3. *Nature Communications* **2015,** *6*, 7026.
[109] Neukirch, A. J., et al. Polaron stabilization by cooperative lattice distortion and cation rotations in hybrid perovskite materials. *Nano Letters* **2016,** *16*, 3809.
[110] Niesner, D., et al. Giant rashba splitting in CH3NH3PbBr3 organic-inorganic perovskite. *Physical Review Letters* **2016,** *117*, 126401.
[111] Oehzelt, M., et al. Organic semiconductor density of states controls the energy level alignment at electrode interfaces. *Nature Communications* **2014,** *5*, 4174.
[112] Ostroverkhova, O. Organic optoelectronic materials: Mechanisms and applications. *Chemical Reviews* **2016,** *116*, 13279.
[113] Ottaviani, G., et al. Hole drift velocity in silicon. *Physical Review B* **1975,** *12*, 3318.
[114] Park, J. S., et al. Electronic structure and optical properties of alpha-CH3NH3PbBr3 perovskite single crystal. *The Journal of Physical Chemistry Letters* **2015,** *6*, 4304.
[115] Park, N.-G. Perovskite solar cells: An emerging photovoltaic technology. *Materials Today* **2015,** *18*, 65.
[116] Pellet, N., et al. Mixed-organic-cation perovskite photovoltaics for enhanced solar-light harvesting. *Angewandte Chemie International Edition* **2014,** *53*, 3151.
[117] Poglitsch, A.; Weber, D. Dynamic disorder in

methylammoniumtrihalogenoplumbates (ii) observed by millimeter-wave spectroscopy. *The Journal of Chemical Physics* **1987,** *87*, 6373.
[118] Rajkanan, K., et al. Absorption coefficient of silicon for solar cell calculations. *Solid-State Electronics* **1979,** *22*, 793.
[119] Ralaiarisoa, M., et al. Effect of water, oxygen, and air exposure on CH3NH3PbI3–xClx perovskite surface electronic properties. *Advanced Electronic Materials* **2018**, 1800307.
[120] Reinert, F., et al. Direct measurements of thel-gap surface states on the (111) face of noble metals by photoelectron spectroscopy. *Physical Review B* **2001,** *63*.
[121] Rief, M., et al. Single molecule force spectroscopy on polysaccharides by atomic force microscopy. *Science* **1997,** *275*, 1295.
[122] Sadoughi, G., et al. Observation and mediation of the presence of metallic lead in organic–inorganic perovskite films. *ACS Applied Materials & Interfaces* **2015,** *7*, 13440.
[123] Salim, T., et al. Perovskite-based solar cells: Impact of morphology and device architecture on device performance. *Journal of Materials Chemistry A* **2015,** *3*, 8943.
[124] Savenije, T. J., et al. Thermally activated exciton dissociation and recombination control the carrier dynamics in organometal halide perovskite. *The Journal of Physical Chemistry Letters* **2014,** *5*, 2189.
[125] Schlesinger, R., et al. Controlling the work function of zno and the energy-level alignment at the interface to organic semiconductors with a molecular electron acceptor. *Physical Review B* **2013,** *87*.
[126] Schultz, T., et al. Tuning the work function of gan with organic molecular acceptors. *Physical Review B* **2016,** *93*.
[127] Schulz, P., et al. Interface energetics in organo-metal halide perovskite-based photovoltaic cells. *Energy & Environmental Science* **2014,** *7*, 1377.
[128] Schulz, P., et al. Electronic level alignment in inverted organometal perovskite solar cells. *Advanced Materials Interfaces* **2015,** *2*, 1400532.
[129] Seah, M. P.; Dench, W. A. Quantitative electron spectroscopy of surfaces: A standard data base for electron inelastic mean free paths in solids *Surface and Interface Analysis* **1979,** *1*, 2.
[130] Sendner, M., et al. Optical phonons in methylammonium lead halide perovskites and implications for charge transport. *Materials Horizons* **2016,** *3*, 613.
[131] Shi, D., et al. Low trap-state density and long carrier diffusion in organolead trihalide perovskite single crystals. *Science* **2015,** *347*, 519.
[132] Shi, T., et al. Unipolar self-doping behavior in perovskite CH3NH3PbBr3. *Applied Physics Letters* **2015,** *106*, 103902.
[133] Smith, N. V., et al. Photoemission spectra and band structures of d-band metals. Viii. Normal emission from cu(111). *Physical Review B* **1980,** *21*, 4331.
[134] Snoke, D. W. *Solid state physics: Essential concepts*, Addison-Wesley: 2009.
[135] Stolterfoht, M., et al. Approaching the fill factor shockley–queisser limit in stable, dopant-free triple cation perovskite solar cells. *Energy & Environmental Science* **2017,** *10*, 1530.

[136] Stolterfoht, M., et al. Visualization and suppression of interfacial recombination for high-efficiency large-area pin perovskite solar cells. *Nature Energy* **2018,** *3*, 847.
[137] Stranks, S. D., et al. Recombination kinetics in organic-inorganic perovskites: Excitons, free charge, and subgap states. *Physical Review Applied* **2014,** *2*, 034007.
[138] Stranks, S. D., et al. Electron-hole diffusion lengths exceeding 1 micrometer in an organometal trihalide perovskite absorber. *Science* **2013,** *342*, 341.
[139] Strocov, V. N. Intrinsic accuracy in 3-dimensional photoemission band mapping. *Journal of Electron Spectroscopy and Related Phenomena* **2003,** *130*, 65.
[140] Sueyoshi, T., et al. Low-density band-gap states in pentacene thin films probed with ultrahigh-sensitivity ultraviolet photoelectron spectroscopy. *Applied Physics Letters* **2009,** *95*, 183303.
[141] Suga, S.; Sekiyama, A. *Photoelectron spectroscopy: Bulk and surface electronic structures*, Springer: 2014.
[142] Tan, Z. K., et al. Bright light-emitting diodes based on organometal halide perovskite. *Nature Nanotechnology* **2014,** *9*, 687.
[143] Tong, M. A. V. H. a. S. Y. *Surface crystallography by leed*, Springer-Verlag Berlin Heidelberg: 1979.
[144] Tsai, H., et al. High-efficiency two-dimensional ruddlesden-popper perovskite solar cells. *Nature* **2016,** *536*, 312.
[145] Ueno, N.; Kera, S. Electron spectroscopy of functional organic thin films: Deep insights into valence electronic structure in relation to charge transport property. *Progress in Surface Science* **2008,** *83*, 490.
[146] Umebayashi, T., et al. Electronic structures of lead iodide based low-dimensional crystals. *Physical Review B* **2003,** *67*.
[147] Valtiner, M., et al. Hydrogen adsorption on polar ZnO(0001)-Zn: Extending equilibrium surface phase diagrams to kinetically stabilized structures. *Physical Review B* **2010,** *82*.
[148] Van Hove, L. The occurrence of singularities in the elastic frequency distribution of a crystal. *Physical Review* **1953,** *89*, 1189.
[149] Véron, A. C., et al. One-dimensional organic–inorganic hybrid perovskite incorporating near-infrared-absorbing cyanine cations. *The Journal of Physical Chemistry Letters* **2018,** *9*, 2438.
[150] W Bardyszewski, L. H. A new approach to the theory of photoemission from solids. *Physica Scripta* **1985,** *32*, 439.
[151] Wagner, C. D., et al. Empirical atomic sensitivity factors for quantitative analysis by electron spectroscopy for chemical analysis. *Surface and Interface Analysis* **1981,** *3*, 211.
[152] Wang, C., et al. Valence band dispersion measurements of perovskite single crystals using angle-resolved photoemission spectroscopy. *Physical Chemistry Chemical Physics* **2017,** *19*, 5361.
[153] Wang, C., et al. Electronic structure evolution of fullerene on CH3NH3PbI3. *Applied Physics Letters* **2015,** *106*, 111603.
[154] Wang, Q., et al. Qualifying composition dependent p and n self-doping in

CH3NH3PbI3. *Applied Physics Letters* **2014,** *105*, 163508.
[155] Weller, M. T., et al. Complete structure and cation orientation in the perovskite photovoltaic methylammonium lead iodide between 100 and 352 k. *Chem Commun (Camb)* **2015,** *51*, 4180.
[156] Wells, A. F. *Structural inorganic chemistry*, Oxford University Press: 2012.
[157] Whitfield, P. S., et al. Structures, phase transitions and tricritical behavior of the hybrid perovskite methyl ammonium lead iodide. *Scientific Reports* **2016,** *6*, 35685.
[158] Winkler, S., et al. The impact of local work function variations on fermi level pinning of organic semiconductors. *Journal of Physical Chemistry C* **2013,** *117*, 22285.
[159] Wolff, C. M., et al. Reduced interface-mediated recombination for high open-circuit voltages in CH3NH3PbI3 solar cells. *Advanced Materials* **2017**, 1700159.
[160] Wu, Y., et al. Retarding the crystallization of PbI2 for highly reproducible planar-structured perovskite solar cells via sequential deposition. *Energy & Environmental Science* **2014,** *7*, 2934.
[161] Xin, Q., et al. Accessing surface brillouin zone and band structure of picene single crystals. *Physical Review Letters* **2012,** *108*.
[162] Y. H. Chang, et al. First-principles study of the structural and the electronic properties of the lead-halide-based inorganic-organic perovskites (CH3NH3)PbX3 and CsPbX3 (X = Cl, Br, I). *Journal of the Korean Physical Society* **2004,** *44*.
[163] Yaffe, O., et al. Local polar fluctuations in lead halide perovskite crystals. *Physical Review Letters* **2017,** *118*, 136001.
[164] Yang, J.-P., et al. Band dispersion and hole effective mass of methylammonium lead iodide perovskite. *Solar RRL* **2018**, 1800132.
[165] Yang, J.-P., et al. Fermi-level pinning appears upon weak electrode-organic contact without gap states: A universal phenomenon. *Organic Electronics* **2017,** *48*, 172.
[166] Yang, W. S., et al. High-performance photovoltaic perovskite layers fabricated through intramolecular exchange. *Science* **2015,** *348*, 1234.
[167] Yang, Y., et al. Top and bottom surfaces limit carrier lifetime in lead iodide perovskite films. *Nature Energy* **2017,** *2*, 16207.
[168] Yantara, N., et al. Inorganic halide perovskites for efficient light-emitting diodes. *The Journal of Physical Chemistry Letters* **2015,** *6*, 4360.
[169] Yin, W.-J., et al. Unusual defect physics in CH3NH3PbI3 perovskite solar cell absorber. *Applied Physics Letters* **2014,** *104*, 063903.
[170] Yoshida, H.; Yoshizaki, K. Electron affinities of organic materials used for organic light-emitting diodes: A low-energy inverse photoemission study. *Organic Electronics* **2015,** *20*, 24.
[171] Yu, Z. G. Rashba effect and carrier mobility in hybrid organic-inorganic perovskites. *The Journal of Physical Chemistry Letters* **2016,** *7*, 3078.
[172] Zhang, F., et al. Complexities of contact potential difference measurements on metal halide perovskite surfaces. *The Journal of Physical Chemistry Letters* **2019**, 890.
[173] Zhang, P., et al. A precise method for visualizing dispersive features in image plots. *Review of Scientific Instruments* **2011,** *82*, 043712.

[174] Zhang, T., et al. Profiling the organic cation-dependent degradation of organolead halide perovskite solar cells. *Journal of Materials Chemistry A* **2017,** *5*, 1103.
[175] Zhang, W. *Photoemission spectroscopy on high temperature superconductor*, Springer: 2013.
[176] Zhang, W., et al. Enhanced optoelectronic quality of perovskite thin films with hypophosphorous acid for planar heterojunction solar cells. *Nature Communications* **2015,** *6*, 10030.
[177] Zheng, F., et al. Rashba spin-orbit coupling enhanced carrier lifetime in CH3NH3PbI3. *Nano Letters* **2015,** *15*, 7794.
[178] Zhou, H., et al. Interface engineering of highly efficient perovskite solar cells. *Science* **2014,** *345*, 542.
[179] Zhou, Y., et al. Room-temperature crystallization of hybrid-perovskite thin films via solvent–solvent extraction for high-performance solar cells. *Journal of Materials Chemistry A* **2015,** *3*, 8178.
[180] Zhu, H., et al. Lead halide perovskite nanowire lasers with low lasing thresholds and high quality factors. *Nature materials* **2015,** *14*, 636.
[181] Zhu, H., et al. Screening in crystalline liquids protects energetic carriers in hybrid perovskites. *Science* **2016,** *353*, 1409.
[182] Zhu, H., et al. Organic cations might not be essential to the remarkable properties of band edge carriers in lead halide perovskites. *Advanced Materials* **2016,** *29*, 1603072.
[183] Zhu, X. Y.; Podzorov, V. Charge carriers in hybrid organic-inorganic lead halide perovskites might be protected as large polarons. *The Journal of Physical Chemistry Letters* **2015,** *6*, 4758.
[184] Zu, F.-S., et al. Impact of white light illumination on the electronic and chemical structures of mixed halide and single crystal perovskites. *Advanced Optical Materials* **2017,** *5*, 1700139.
[185] Zu, F., et al. Constructing the electronic structure of CH3NH3PbI3 and CH3NH3PbBr3 perovskite thin films from single-crystal band structure measurements. *The Journal of Physical Chemistry Letters* **2019,** *10*, 601.
[186] Zu, F., et al. Surface state density determines the energy level alignment at hybrid perovskite/electron acceptors interfaces. *ACS Applied Materials & Interfaces* **2017,** *9*, 41546.
[187] Zuo, C.; Ding, L. An 80.11% ff record achieved for perovskite solar cells by using the nh4cl additive. *Nanoscale* **2014,** *6*, 9935.

Publications

1. **F. S. Zu**, C. M. Wolff, M. Ralaiarisoa, P. Amsalem, D. Neher, N. Koch. Unraveling the electronic properties of lead halide perovskites with surface photovoltage in photoemission studies. ACS Appl. Mater. Interfaces **2019**, 11, 21578.

2. **F. S. Zu**, P. Amsalem, D. A. Egger, R. Wang, C. M. Wolff, H. Fang, M. A. Loi, D. Neher, L. Kronik, S. Duhm, N. Koch. Constructing the electronic structure of $CH_3NH_3PbI_3$ and $CH_3NH_3PbBr_3$ perovskite thin films from single-crystal band structure measurements. *J. Phys. Chem. Lett.* **2019**, 10, 601.

3. **F. S. Zu**, P. Amsalem, M. Ralaiarisoa, T. Schultz, R. Schlesinger, N. Koch. Surface state density determines the energy level alignment at hybrid Perovskite/electron acceptors interfaces. *ACS Appl. Mater. Interfaces* **2017**, 9, 41546.

4. **F. S. Zu**, P. Amsalem, I. Salzmann, R.-B. Wang, M. Ralaiarisoa, S. Kowarik, S. Duhm, N. Koch. Impact of white light illumination on the electronic and chemical structures of mixed halide and single crystal perovskites. *Adv. Optical Mater.* **2017,** 5, 1700139.

5. P. Caprioglio, **F. S. Zu**, C. Michael, M. Wolff, J. A. M. Prieto, M. Stolterfoht, P. Becker, N. Koch, T. Unold, B. Rech, S. Albrecht, D. Neher. High open circuit voltages in pin-type perovskite solar cells through strontium addition. *Sustainable Energy Fuels*, **2019**, 3, 550.

6. C.M. Wolff, **F. S. Zu**, A. Paulke, L.P. Toro, N. Koch, D. Neher. Reduced interface-mediated recombination for high open-circuit voltages in $CH_3NH_3PbI_3$ solar cells. *Adv. Mater.* **2017**, 29, 1700159.

7. G. Sun, **F. S. Zu**, N. Koch, J. Rappich, K. Hinrichs. In Situ infrared spectroscopic monitoring and characterization of the growth of polydopamine (PDA) films. *Phys. Status Solidi B*, **2019**, 256, 1800308.

8. S. Zhang, M. Stolterfoht, A. Armin, Q. Lin, **F. S. Zu**, J. Sobus, H. Jin, N. Koch, P.

Meredith, P. L. Burn. D. Neher. Interface engineering of solution-processed hybrid organohalide perovskite solar cells. *ACS Appl. Mater. Interfaces* **2018**, 10, 21681.

Acknowledgements

This dissertation was complemented with the help of many people, and I would like to thank them now.

At first, I want to thank my supervisor Prof. Norbert Koch, who gave me the chance to come to Berlin as an exchange student during my master study, and the opportunity to pursue my PhD study in his group at Humboldt-Universität zu Berlin. He guided me through my research from many aspects, and provided me so many opportunities to attend several international conferences.

I would like to thank all group members from SMS for helping me over the past few years. In particular, a big thank you to Dr. Patrick Amsalem for numerous discussions and supports. A special thank you to Dr. Johannes Frisch for helping me settle down when I first arrived in Berlin.

I want to thank Prof. Steffen Duhm for hosting me in his group many times and letting me conduct ARPES experiments at Soochow University. I would like to thank Christian Wolff, Dr. David Egger, Pietro Caprioglio, Prof. Leeor Kronik and Prof. Dieter Neher for great collaborations.

Lastly, I would like to thank my family and my wife Shanshan for their strong support.

Selbstständigkeitserklärung

Hiermit erkläre ich, die Dissertation selbstständig und nur unter Verwendung der angegebenen Hilfen und Hilfsmittel angefertigt zu haben. Ich habe mich nicht anderwärts um einen Doktorgrad in dem Promotionsfach beworben und besitze keinen entsprechenden Doktorgrad. Die Promotionsordnung der Mathematisch-Naturwissenschaftlichen Fakultät, veröffentlicht im Amtlichen Mitteilungsblatt der Humboldt-Universität zu Berlin Nr. 42 am 11. Juli 2018, habe ich zur Kenntnis genommen.

Fengshuo Zu

Berlin, 11.03.2019